



The University of
Nottingham

UNITED KINGDOM • CHINA • MALAYSIA

**Development of Advanced Polymer Nanocomposites for
Thermal Management Applications**

Hongnan Zhang

Thesis submitted to the University of Nottingham for the degree of

Doctor of Philosophy

Supervisors:

Dr. Fang Xu, Dr. Liliana De Lillo, Prof. Lee Empringham, Prof. Xianghui Hou,

Dr. Barun Ghosh

Faculty of Engineering

August 2024

Abstract

The miniaturisation and high-level integration of advanced electronic devices, such as 3D chip stacks, bring about increased functionality, efficiency and power density. However, this has also intensified the challenge of heat dissipation. Unfortunately, the existing thermally conductive composites fall short of meeting the growing demands of the electronics industry. Hence, development of high thermal conductivity composites becomes the highly demanded to address the heat dissipation issues of electrical and electronic devices.

This research, based on the review of the current research on thermally conductive composite insulating materials, endeavours to prepare high-performance thermally conductive epoxy resin-based composites. Different strategies, including freeze casting and vacuum-assisted filtration methods, have been employed to prepare a range of novel thermally conductive composites via the alignment of micro/nano-structured filler units.

Firstly, 3D vertically aligned silicon carbide (SiC) whiskers aerogels were constructed by freeze casting method, followed by thermal sintering to consolidate the aerogels. The resulting 3D network structure establishes thermal transfer pathways within polymer composites, leading to a much-improved thermal conductivity ($1.55 \text{ W m}^{-1} \text{ K}^{-1}$) and a low coefficient of thermal expansion (through-plane: 48 ppm K^{-1} , in-plane: 35 ppm K^{-1}) even at a low filler loading of 10.2 vol%.

The vacuum-assisted filtration method was used to construct horizontally aligned hybrid fillers consisting of hexagonal boron nitride platelets (h-BN) and SiC whiskers within epoxy resin. The results reveal that Epoxy/BN/SiC bi-layered composite achieves the highest in-plane thermal conductivity at room temperature, measuring of

2.16 W m⁻¹ K⁻¹, compared to composite with single filler and randomly mixed hybrid fillers (1.55 W m⁻¹ K⁻¹) at 15.5 vol% total loading. This study also indicates a synergistic effect on dielectric properties and thermal conductivity in the epoxy/BN/SiC bi-layered composite. Epoxy/BN/SiC bi-layered composite demonstrates enhanced dielectric constant (9.03) with low dielectric loss of 0.015 (1000 Hz) at room temperature, surpassing the composite with randomly mixed hybrid fillers, which exhibits a dielectric loss of 0.029. This innovative method holds promise for developing high-performance dielectric materials featured with improved thermal conductivity and low dielectric loss.

Building on the success achieved in improving in-plane thermal conductivity, the vacuum-assisted filtration method was also used to enhance the through-plane thermal conductivity. The h-BN and Graphene oxide (GO) were effectively vertically oriented within the epoxy resin composites. Consequently, the BN-GO-epoxy composite boosts an impressive through-plane thermal conductivity of 5.51 W m⁻¹ K⁻¹ at a loading of 42 vol%. In addition, these composites exhibit a revolutionarily low coefficient of thermal expansion (5 ppm K⁻¹) that can match well with materials used in Si semiconductor chips. This approach is very promising for advancing materials with super thermal and mechanical characteristics.

This work offers fresh perspectives on the design and formulation of high-performance thermal management materials. The developed composites showcase significant potential for applications in the next generation of power electronics.

Publications

1. Chenxi Hu, **Hongnan Zhang**, Nigel Neate, Michael Fay, Xianghui Hou, David Grant, Fang Xu. Highly Aligned Ni-Decorated GO–CNT Nanostructures in Epoxy with Enhanced Thermal and Electrical Properties. *Polymers* 2022, 14(13), 2583.
2. **Hongnan Zhang**, Ruqaiyah Khan and Fang Xu. Constructing Hybrid BN and SiC Filler Silicone Polymer Composites with Enhanced Thermal Conductivity (Abstract). 2023 6th International Conference on Polymer Science and Nanotechnology, Barcelona, Spain.
3. **Hongnan Zhang**, Barun Ghosh, Xianghui Hou, Michael Fay, Christopher Parmenter, Fang Xu. Construction of 3D SiC Whiskers Networks for Polymer Composites with Improved Thermal Conductivity. (In preparation)
4. **Hongnan Zhang**, Barun Ghosh, Paolo Giangrande, Xiaofei Hu, Ming Li, David M Grant, Xianghui Hou, Fang Xu. Development of thermally conductive dielectric bi-layered nanocomposite. (In preparation)
5. **Hongnan Zhang**, Adeeba Shaheen, Xianghui Hou, Fang Xu. Enhanced through-plane thermal conductivity of boron nitride and graphene oxide epoxy composites by vacuum filtration. (In preparation)

Acknowledgements

I am profoundly grateful to my supervisor, Dr. Fang Xu, whose unwavering guidance, encouragement, and insightful advice have been invaluable throughout my PhD journey. I consider myself exceptionally fortunate to have had her as my supervisor. Beyond her academic support, Dr. Xu has shown genuine care for my well-being, embodying not just the role of a supervisor but also that of a trusted friend. Her presence has brought immense joy and stability to my PhD experience, particularly amidst the challenges of being far away from home and family. I owe much of my happiness and success in this journey to her nurturing guidance and steadfast support.

I extend my heartfelt gratitude to my co-supervisors Prof. Xianghui Hou, Dr. Barun Ghosh, Dr. Liliana De Lillo, and Prof. Lee Empringham for their sustained help and invaluable insights throughout my research journey. Despite not being affiliated with the University of Nottingham anymore, Dr. Xianghui Hou, and Dr. Barun Ghosh have remained steadfast in their commitment to my progress, offering invaluable guidance and encouragement. Their contributions have been instrumental in shaping this thesis, and I am deeply appreciative for their continued support without which this accomplishment would not have been possible.

I would like to give thanks to the technicians in Advanced Materials Research Group, especially to Mr. Theo Ching, Dr. Hannah Constantin, Mr. John Kirk and Mr. Richard Homer for their constant help and training. Thanks to Mr. Martin Roe, Mr. Christopher Parmenter, Dr. Nigel Neate and Dr. Michael Fay from the Nanoscale and Microscale Research Centre (NMRC) for their help on SEM, TEM and FIB-SEM. Thanks to Dr. Grace Guan for LFA training. I would like to acknowledge group members Dr. Yu Yu,

Dr. Lei Lei, Dr. Chenxi Hu, Dr. Mengjuan Wu, Dr. Peifeng Li, Dr. Daniel Koti and many others for their friendship and support.

I am deeply thankful to my friends Mengjuan Wu and Lingyu Qin for their kindly help during the challenging times of the Covid-19 pandemic. Their companionship and encouragement were invaluable, and I remain eternally grateful for their role in my life.

To my beloved parents, I owe an immeasurable debt of gratitude for their ongoing support and boundless love. Despite the difficulties imposed by the pandemic, which prevented us from meeting for nearly four years, their constant love and encouragement provided me with the strength and determination to persevere through my PhD journey. Their constant backing has been my guiding light, and I am forever thankful for their presence in my life.

I also wish to give thanks to the China Scholarship Council and the University of Nottingham for the scholarship support.

Finally, I would like to thank all my friends, colleagues and families who have provided valuable support during this journey. I apologize for not being able to mention everyone by name, but please know that I sincerely appreciate all the help and support you have provided me. Your contributions have made a significant difference, and I am truly grateful for every one of you.

Table of Contents

Abstract	i
Publications	iii
Acknowledgements	iv
Table of Contents	vi
List of Figures and Tables.....	xi
List of Abbreviations.....	xxii
 Chapter 1 Introduction	 1
1.1 Background	1
1.2 Motivation and Innovation.....	5
1.2.1 Motivation.....	5
1.2.2 Innovation	6
1.3 Aims and Objectives	7
1.4 Outline of Chapters	9
 Chapter 2 Literature review	 10
2.1 Background on thermal management materials.....	10
2.2 Mechanism of heat transfer in polymer composites and key influencing factors 10	
2.2.1 Mechanism of heat transfer in polymer composites	10
2.2.2 Key influencing factors	15

2.3	Solutions and limitations of improving thermal conductivity of polymer composites.....	18
2.3.1	Functionalization of filler surface	19
2.3.2	Hybrid particles	20
2.3.3	Oriented fillers	21
2.4	Distribution control of thermally conductive fillers in polymer composites	22
2.4.1	Polymer composites with randomly distributed fillers	22
2.4.2	Polymer composites with 2D aligned fillers	25
2.4.3	Polymer composites with 3D network fillers.....	31
2.5	Effect of fillers on CTE of polymer composites	38
2.6	Dielectric properties of polymer composites	41
2.6.1	Dielectric constant and dielectric loss.....	41
2.6.2	Mechanism of dielectric properties	42
2.6.3	The research on thermally conductive dielectric composites	43
2.7	Application of thermally conductive composites.....	46
2.7.1	Electronic packaging.....	46
2.7.2	Light-emitting Diode (LED) devices	48
2.7.3	Solar cells	49
2.8	Summary	51
	Chapter 3 Methodologies	54

3.1	Raw materials and chemicals	54
3.2	Preparation of 3D SiCW network aerogels (3D SiCW) and 3D SiCW-epoxy composites	54
3.2.1	Preparation of 3D SiCW network aerogels (3D SiCW).....	54
3.2.2	Preparation of 3D networks SiCW-epoxy Composites (3D SiCW-epoxy)	55
3.3	Fabrication of BN/SiC bi-layered epoxy resin composites.....	57
3.4	Constructing vertically aligned Boron Nitride-Graphene Oxide (BN-GO) epoxy composites by vacuum-assisted filtration method.....	59
3.5	Microstructural Characterisation Methods.....	60
3.5.1	Scanning Electron Microscopy (SEM)	60
3.5.2	Focused Ion Beam Scanning Electron Microscopy (FIB-SEM).....	62
3.5.3	Transmission Electron Microscope (TEM).....	63
3.5.4	Energy Dispersive Spectroscopy (EDS)	65
3.5.5	X-ray Diffraction (XRD).....	65
3.5.6	Density measurement	67
3.6	Evaluation of mechanical properties	68
3.7	Evaluation of Thermal Performance	69
3.7.1	Thermal diffusivity test.....	69
3.7.2	Differential Scanning Calorimetry (DSC) and Modulated DSC (MDSC)	70

3.7.3	Thermal conductivity	71
3.7.4	The coefficient of thermal expansion (CTE)	72
3.7.5	Thermogravimetric Analysis (TGA).....	72
3.8	Electrical resistance measurement	73
3.9	Evaluation of dielectric properties	73
3.9.1	Dielectric constant measurement	73
3.9.2	Breakdown strength	74
Chapter 4 3D SiC Whiskers Networks for Polymer Composites with Improved Thermal Conductivity		
		75
4.1	Fabrication and characterisation of 3D SiCW network aerogels	75
4.2	Structural characterisation of 3D network SiCW-epoxy composites	90
4.3	Thermal and electrical properties of 3D SiCW-epoxy composites.....	92
4.4	Discussion	102
4.4.1	The effect of SiCW aerogel structure on thermal conductivity of composites.....	102
4.4.2	The effect of SiCW aerogel structure on CTE.....	107
4.5	Summary	111
Chapter 5 Development of thermally conductive dielectric bi-layered nanocomposite		
		112
5.1	Characterisation of BN/SiC bi-layered film.....	112
5.2	Characterisation of Epoxy/BN/SiC bi-layered composite	113

5.3	Thermal properties of Epoxy/BN/SiC bi-layered composite.....	116	
5.4	Dielectric properties of Epoxy/BN/SiC bi-layered composite.....	122	
5.5	Electrical properties of Epoxy/BN/SiC bi-layered composite	126	
5.6	Discussion	127	
5.7	Summary	134	
Chapter 6 Enhanced through-plane thermal conductivity of BN and GO epoxy composites by vacuum-assisted filtration			135
6.1	Characterisation of BN-GO slices.....	135	
6.2	Characterisation of BN-GO composites.....	141	
6.3	Thermal properties of BN-GO composites	144	
6.4	Thermal conductivity of BN-GO5-70 composites.....	147	
6.5	Discussion	148	
6.6	Summary	153	
Chapter 7 Conclusion and future work			155
7.1	Conclusion	155	
7.2	Future work.....	158	
References.....			161

List of Figures and Tables

Figure 1.1 (a) 2D packages involve mounting two or more chips on the same level of the package base, (b) 2.5D introduces an intermediary layer between the chip and the base of the package, and (c) 3D packages vertically stack the chips. [4]	2
Figure 1.2 Schematic image of glass fibre reinforced substrate [15].....	3
Figure 2.1 The distribution state of fillers in the polymer matrix.....	14
Figure 2.2 Percolation-like behaviour with the loading fraction increased during which the pathway between two connected fillers increases [55].	15
Figure 2.3 Surface treatment of AlN particles [90].....	23
Figure 2.4 Schematic of preparing PVDF/BN/CNT composites with three different sizes of BN [91].	24
Figure 2.5 The methods for alignment of fillers in polymer [94].	25
Figure 2.6 Cross-section micrograph of the composites prepared (a) by doctor blading (b) by casting only [71].	27
Figure 2.7 Schematic of the composite preparation by vacuum filtration force [99].	28
Figure 2.8 The SEM images of the (a-b) cross-section (c) surface morphology of NF-BNNS-PVA paper. Red arrows in (b) indicate the bridges between platelets. [87] ..	28
Figure 2.9 Fabrication procedure of the AlN-Fe ₃ O ₄ hybrid filler [101].	29
Figure 2.10 Schematic of the process for preparing BNNS/PVA films [105].....	30
Figure 2.11 Schematic of 3D BNNS network preparation using sol-gel technique, and influence of BNNS loading on the thermal conductivity [110].	32
Figure 2.12 Illustration of the freeze casting process. [114].....	34

Figure 2.13 The relationship between the aqueous suspension states and the processing steps. [116]	34
Figure 2.14 Schematic of freeze-casting principle. [117]	35
Figure 2.15 An illustration of the fabrication of 3D BNNS network [118].....	36
Figure 2.16 Schematic route for the preparation of 3D BN/Epoxy composites by salt templating method [119].	36
Figure 2.17 Illustration of preparation procedures of the Graphene network and the polymer nano composite [120].	37
Figure 2.18 (a) Working principle of TIMs; (b) The electronics package with two TIMs. [158]	47
Figure 2.19 A solar cell module made by different layers [167].	50
Figure 2.20 Illustration of operation of TIM in solar cell [169].	51
Figure 3.1 Schematic of the fabrication of 3D SiCW-epoxy. The experimental process consists of four steps: (I) preparation of an aqueous slurry containing SiC and PVA; (II) freezing the slurry in liquid nitrogen; (III) freeze-drying and sintering the aerogels; (IV)polymer infiltration.	56
Figure 3.2 Schematic for fabricating BN/SiC bi-layered epoxy resin composite by sequential vacuum-assisted filtration.	58
Figure 3.3 Schematic of preparing vertically aligned BN-GO composites by vacuum-assisted filtration.	60
Figure 3.4 SEM probe model and operating principle.[171]	61

Figure 3.5 (a) Schematic image of FIB-SEM system [172]; (b) the images of picking one fibre by a needle; (c) the images of putting the fibre on the holder.	63
Figure 3.6 Schematic diagram of TEM system [173].	64
Figure 3.7 Principle of X-ray diffraction.[176].	66
Figure 3.8 Archimedes Principle.	68
Figure 3.9 Schematic of the measurement of the thermal diffusivity. [177]	70
Figure 4.1 Photographs of (a) the mould; (b) 3D SiCW aerogels; (c) Photograph of the 3D SiCW aerogel standing on ear of wheat without bending the ears, demonstrating its light weight; (d) Compression stress-strain curves of 3D SiCW aerogel; inset of (d) shows the process of compression test and the 3D SiCW aerogel after compression.	77
Figure 4.2 Photograph of showing the weight of (a) heavy object, (b) SiCW aerogel, (c) favourable strength of 3D SiCW aerogels.	77
Figure 4.3 SEM images of (a) a cluster of SiC whiskers, (b) an individual SiC whisker; the inset of (b) is the illustration of the effect of SiC whisker orientation on the XRD pattern; (c) (d) SEM images of SiCW aerogel layer at different magnifications; inset of (d) is the schematic illustration of SiCW aerogel layer, (e) XRD pattern of SiC whiskers, Homo-freeze-SiC aerogel and 3D SiCW-2.5 aerogel sintering at 1000 °C, 1100 °C and 1200 °C; (f) XRD pattern of 3D SiCW aerogels with different loading sintering at 1000 °C.	79
Figure 4.4 SEM images of the cross-section of 3D SiCW aerogels with various solid loadings (a) SiCW-2.5; (b) SiCW-3.6; (c) SiCW-4.6; (d) SiCW-5.7; (e) SiCW-6.7; (f) SiCW-8.2; (g) SiCW-10.2.	82

Figure 4.5 (a) Digital photograph of SiCW aerogel fabricated by homogeneous freeze casting method; SEM images of (b) (c) SiCW aerogel with 2.5 vol% loadings fabricated by homogeneous freeze casting method followed by sintering at 1000 °C for 3 hours; (d) SiCW aerogel with 10.2 vol% loadings fabricated by homogeneous freeze casting method followed by sintering at 1000 °C for 6 hours.	83
Figure 4.6 The photos of SiCW-PVA aerogels with different PVA contents.	85
Figure 4.7 Cross-sectional SEM images of SiCW aerogels with different PVA contents: (a) 0.5 wt%, (b) 0.9 wt%, (c) 1.4 wt%, (d) 2.7 wt%, (e) 3.6 wt%, (f) 4.4 wt%, (g) 8.5 wt%; (h) Digital photo of SiCW-PVA-4.4 aerogel before and after sintering; (i-l) Cross-sectional SEM images of SiCW aerogels before sintering with 4.4 wt% PVA content in slurry at different magnifications.	87
Figure 4.8 SEM image of SiC whisker junctions in 3D SiCW aerogel.	88
Figure 4.9 (a) SEM images for EDS scanning of SiC aerogel after sintering at 1200 °C; (b) Elemental mapping of Si; (c) Elemental mapping of O. (d) FIB-SEM images of picking out a SiC fibre by the needle; (e) SEM images of SiC fibre after polishing by focus ion beam; (f) high magnification TEM image of transfer interface, the insets of (f) show the SAED pattern of inner core and outer layer of SiC fibre; (g) TEM images of SiC fibre sintered at 1100 °C for 6 hours after polishing by FIB-SEM; (h) TEM images of local surface for EDS scanning of fibre shown in (g); (i) Elemental mapping of O; (j) Elemental mapping of Si. TEM images of SiC fibre sintered at (k) 900 °C for 6 hours, (l) 1000 °C for 6 hours, (m)1000 °C for 3 hours, (n) 1200 °C for 6 hours.....	89

Figure 4.10 (a) SEM images of the fracture morphology in 3D SiCW-3.6-epoxy composites; EDS elemental mapping of (b) Si (c) O; (d) high-resolution SEM images of (a); (e) high-resolution SEM images of the SiC fibre marked A in (d); (f) high-resolution SEM images of the SiC fibre marked B in (d).....	91
Figure 4.11 (a) (b) SEM images of the cross-section of R-SiCW-epoxy composites at different magnification.....	92
Figure 4.12 (a) Through-plane and in-plane thermal conductivity of 3D SiCW-epoxy composites with aerogels sintered at 1000 °C for 6 hours as a function of filler tested at room temperature; (b) Schematic of the heat dissipation through the 3D SiCW-epoxy resin; (c) Through-plane thermal conductivity of SiCW composites fabricated by different method; Homo-freeze-SiCW-epoxy was prepared by homogeneous freeze-casting method and followed by sintering at 1000 °C for 6 hours; 3D SiCW-epoxy was prepared by unidirectional freeze-casting method and followed by sintering at 1000°C for 6 hours; R-SiCW-epoxy was prepared by mixing SiCW and epoxy directly; (d) The through-plane thermal conductivity of 3D SiCW-epoxy-10.2 vol% with SiC aerogels sintered at different temperature; (e) logarithmic values of the through-plane thermal conductivity of 3D SiCW-epoxy composites with aerogels sintered at 1000 °C for 6 hours as a function of the SiCW volume fraction; (f) logarithmic values of the through-plane thermal conductivity of R-SiCW-epoxy composites as a function of the SiCW volume fraction.....	96
Figure 4.13 (a) Thermal conductivity of 3D SiCW-epoxy-10.2 vol% composites with 3D SiCW-10.2 aerogels sintered at 1000 °C for different hours; (b) Through-plane	

thermal conductivity of SiCW-3.6-epoxy composites with aerogels prepared by different concentrations of PVA.	97
Figure 4.14 (a) CTE values (b) T_g values of 3D SiCW-epoxy composites as a function of SiCW loadings.....	98
Figure 4.15 Volume resistivity of 3D SiCW-epoxy composites with different SiCW loadings.	99
Figure 4.16 (a) Experimental setup for thermal infrared imaging; Infrared thermal images of (b) (c) epoxy, (d) R-SiCW-epoxy, (e) 3D SiCW-epoxy composites; (f) Surface temperature variation with heating time; (g) Optical images of epoxy, R-SiCW-epoxy and SiCW-epoxy composites placed on a hot plate; (h) Infrared thermal images of samples corresponding to (g) at the beginning of heating; (i) Infrared thermal images of samples corresponding to (g) after heating 30 seconds.....	101
Figure 4.17 Thermal conductivity enhancement efficiency (η) of the composites with different SiC whiskers volume loading.....	106
Figure 5.1 (a) Illustration of layer-by-layer structure, (b) Optical images of layered structures (BN/SiC bi-layer), (c) Epoxy/BN/SiC bi-layered composite after epoxy infiltration, SEM image of (d) SiC surface of BN/SiC bi-layer and (e) h-BN surface of BN/SiC bi-layer.	113
Figure 5.2 SEM images of (a) the cross-section of Epoxy/BN/SiC layered composite; (b) the surface of Epoxy/SiC layer; (c) the surface of Epoxy/BN layer; (d) the surface of Epoxy/BN/SiC random composite.	114
Figure 5.3 (a) XRD patterns of pure BN platelets powder, SiC whisker, EBNSiC_2L-SiC surface, EBNSiC_2L-BN surface and EBNSiC_R; (b) T_c analysis of BN platelets, EBNSiC_2L-BN surface and EBNSiC_R calculated from intensity values	

of XRD peak data; inset of (b) illustrates the impact of BN orientation on the XRD pattern.....	116
Figure 5.4 TGA curve of Epoxy/BN/SiC layered composite from room temperature to 700 °C.	119
Figure 5.5 In-plane and through-plane thermal conductivity of pure epoxy resin, EBN, ESiC, EBNSiC_R and EBNSiC_2L composites.	119
Figure 5.6 (a) The coefficient of thermal expansion of pure epoxy resin, EBN, ESiC and EBNSiC_2L composites; (b) Dimensional change as a function of operating temperature of the pure epoxy, EBN, ESiC and EBNSiC_2L.....	121
Figure 5.7 (a) Dielectric constant and dielectric loss dependence on frequency for pure epoxy and composites at room temperature; Dielectric constant and dielectric loss dependence on frequency at different temperature for (b) Epoxy, (c) EBN, (d) ESiC, (e) EBNSiC_R, (f) EBNSiC_2L.....	124
Figure 5.8 Dielectric constant dependence on frequency for pure epoxy and composites at room temperature.	124
Figure 5.9 (a) Weibull distribution of breakdown strength of pure epoxy resin and composites; SEM images of (b) epoxy; (c) EBNSiC_R composites; (d) EBNSiC_2L composites after breakdown.....	126
Figure 5.10 Electrical resistivities of epoxy and composites.....	127
Figure 6.1 SEM images of h-BN powder with size of (a) 0.5 μm , (b) 70 nm; (c) XRD pattern of h-BN powder and GO.....	136
Figure 6.2 XRD pattern of aligned BN-GO slices. Inset shows the illustration of the effect of BN orientation on the XRD pattern.	138

Figure 6.3 (a) (b) (c) SEM images of the surface of aligned BN-GO3 slice with different magnification; (d) (e) (f) Elemental mapping collect from (c).	139
Figure 6.4 SEM images of the cross-section of (a) (b) BN-GO5; (c)(d) BN-GO7..	139
Figure 6.5 Compressive stress-strain curves of (a) pure BN and BN-GO slices; (b) pure BN. (c) Photo of BN slice during compression test; (d) Photo of BN slices after compression test; (e) Photo of BN-GO5 during compression test; (f) Photo of BN-GO5 after compression test.	140
Figure 6.6 SEM images of (a) the top surface of BN-GO5 composites, (b) (c) (d) the fracture surface cross-section of BN-GO5 composites.	142
Figure 6.7 TGA curves of the BN-GO1, BN-GO3 and BN-GO5 composites.....	144
Figure 6.8 (a) Thermal conductivity of aligned BN-GO-epoxy composites with different GO weight percentage in BN-GO slices; (b) Thermal conductivity of pure epoxy resin, BN-epoxy and BN-GO5-epoxy.	145
Figure 6.9 (a) Dimension change of pure epoxy resin, BN composites and BN-GO composites with the temperature change; (b) CTE values of pure epoxy resin, BN composites and BN-GO composites.	147
Figure 6.10 The thermal conductivities of epoxy resin, BN-epoxy, BN-GO5-epoxy and BN-GO5-70 composites.	148
Figure 6.11 The phonon dispersion spectra of (a) h-BN [235], (b) Graphene [237].	151

Table 2.1 Thermal conductivities of polymers commonly used as matrix [8, 10, 44, 45].	12
Table 2.2 Thermal conductivities of commonly used thermally conductive fillers [10, 50-54].	13
Table 2.3 CTE values of the most commonly used polymer [123].	38
Table 2.4 CTE values of materials in electronic packaging. [13]	39
Table 3.1 The weight (W_{SiC} , W_{PVA}) and volume (V_{H_2O}) used to prepare SiCW aerogels with different SiC loadings; $R_{SiC/PVA}$ is weight ratio of SiC and PVA; SiC wt% and PVA wt% are the weight percentage of SiC and PVA in slurry.	55
Table 3.2 The details of materials used in the experiment. W_{BN} is the weight of BN; W_{SiC} is the weight of SiC; V_{IPA} is the volume of IPA.	58
Table 3.3 The details of materials used in the experiment. W_{BN} is the weight of 0.5 μm BN; W_{GO} is the weight of GO; W_{BN70} is the weight of 70 nm BN nanoparticles.	60
Table 4.1 The solid volume loading, density and porosity of 3D SiCW aerogels with different solid loading.	76
Table 4.2 The Texture coefficient (Tc) of SiC whiskers (SiCWs), Homo-freeze-SiCW aerogel and 3D SiCW aerogels.	80
Table 4.3 The weight (W_{SiC} , W_{PVA}) and volume (V_{H_2O}) used to prepare SiCW aerogels with different PVA contents; SiC/PVA is the weight ratio of SiC and PVA, SiCwt% is the weight percentage of SiC in the suspension; PVAwt% is the weight percentage of PVA in the suspension.	85
Table 4.4 The density and porosity of SiCW aerogels with different PVA contents.	86

Table 4.5 Comparison of thermal conductivity and CTE of our 3D SiCW-epoxy composite with epoxy-based composites filled with other fillers in the published literature.	107
Table 4.6 The properties of SiC and epoxy. [194, 195, 202, 203].	110
Table 5.1 Thermal conductivity (K) data for three samples of the same materials, including the average value, standard deviation (S). Standard error (SE), t-value and p-value of the two groups data (in-plane and through-plane thermal conductivity) calculated by statistical methods.	120
Table 5.2 Comparison of thermal conductivity, dielectric constant, dielectric loss and breakdown strength of our EBNSiC_2L composite with various polymer in the open literature.	133
Table 6.1 The intensity of peak (002), (100) and (102); the relative intensity of (100) and (002) peaks; text coefficient of peak (002) and (100) for pure h-BN powder and aligned BN-GO slices.	137
Table 6.2 The weight loss of samples at 700 °C, the original samples weight, weight of epoxy and GO in samples, weight of BN, weight of GO, the weight of epoxy in samples.	143
Table 6.3 The density of samples (ρ), volume of epoxy in samples (V_{epoxy}), volume of whole samples (V_{sample}), volume of BN in samples (V_{BN}), volume loading of BN in samples ($V_{\text{BN}\%}$), volume of BN and GO in samples ($V_{\text{BN+GO}}$), volume loading of BN and GO in samples ($V_{\text{BN+GO}\%}$).	143
Table 6.4 The density (ρ), specific heat capacity (C_p) through-plane thermal diffusivities (λ), the calculated thermal conductivities (K) of epoxy resin, BN-epoxy, BN-GO-epoxy composites.	145

Table 6.5 The density (ρ), specific heat capacity (C_p) through-plane thermal diffusivities (λ), the calculated thermal conductivities (K) of epoxy resin, BN-epoxy, BN-GO5-epoxy and BN-GO5-70 composites. 148

Table 6.6 Comparison of thermal conductivity (K) and CTE of our vertically aligned BN-GO-epoxy composite with other BN polymer composites. 153

List of Abbreviations

1D	One-dimensional
2D	Two-dimensional
3D	Three-dimensional
AC	Alternating current
AlN	Aluminium Nitride
Al ₂ O ₃	Aluminium oxide
BeO	Beryllium oxide
BN	Boron Nitride
BNNS	Boron nitride nano sheet
BNNT	Boron nitride nano tube
CTE	Coefficient of thermal expansion
CNTs	Carbon Nanotubes
CNFs	cellulose nanofibers
DSC	Differential Scanning Calorimetry
EV	Electric vehicles
EEE	Electrical and Electronic Equipment
EDS	Energy Dispersive Spectroscopy
EIS	Electrochemical Impedance Spectroscopy
FEG-SEM	Field emission gun scanning electron microscope
FIB-SEM	Focused Ion Beam Scanning Electron Microscopy
Fe ₃ O ₄	Ferroferric oxide
GO	Graphene Oxide
GNP	Graphite nano-platelets
GNs	Graphene nanosheets
h-BN	hexagonal BN

IPA	Isopropyl alcohol
LED	Light-emitting Diode
MgO	Magnesium oxide
MF	Melamine-formaldehyde
MDSC	Modulated Differential Scanning Calorimetry
PCBs	Printed circuit boards
PVA	Polyvinyl acetate
PVDF	Poly(vinylidene fluoride)
PP	Polypropylene
PS	Polystyrene
PC	Polycarbonate
PEEK	Polyetheretherketone
PPS	Polyphenylene sulfide
PVC	Polyvinyl chloride
PVDF	Polyvinylidene difluoride
PTFE	Polytetrafluoroethylene
PEVA	Poly(ethylene vinyl acetate)
PI	Polyimide, Thermoplastic
PDMS	Poly(dimethylsiloxane)
R	Electrical resistance
rGO	Reduced Graphene Oxide
SAED	Selected Area Electron Diffraction
SEM	Scanning Electron Microscope
SiC	Silicon Carbide
SiCW	Silicon Carbide whisker
SiO ₂	Silica dioxide

SWCNT	Single wall CNTs
T _g	Glass transition temperature
TEM	Transmission electron microscope
TGA	Thermogravimetric Analysis
TIM	Thermal interface materials
T _c	Texture coefficient
XRD	X-Ray Diffraction

Chapter 1 Introduction

1.1 Background

In the UK, greenhouse gas emissions are to be cut to zero by 2050, as outlined in a new government plan aimed at combating climate change [1]. Consequently, there is a pressing need to advance the timeline for phasing out petrol and diesel vehicles to meet this target by 2035. This shift presents both challenges and opportunities, particularly for electric vehicles (EV) within the automotive industry. Within EVs, advanced electronic devices play a crucial role, necessitating miniaturisation, multifunctionality, reduced weight and increased power density [2].

The miniaturization of electronic components hinges on the development of advanced electronic packaging technologies. The manufacturing process of electronic products can be likened to construct a building, with the integrated circuit chip serving as a floor. Just as buildings aim to maximise construction density, electronic products must assemble multiple layers of chips with distinct functions to enhance packaging efficiency, optimise internal space utilisation, and reduce overall size [3]. Figure 1.1 illustrates the progression from two-dimensional (2D) to three-dimensional (3D) packaging structure [4]. While 3D packaging enhances the functionality of electronic products and significantly boosts power density, it also induces substantial heat dissipation challenges [5]. Failure to dissipate accumulated heat from components in a timely manner poses a serious risk to the stability and safety of the electronic products. Studies show that more than half of the electronic devices failure stem from heat-related issues [2]. Consequently, efficient heat dissipation has emerged as a critical necessity in power electronics, crucial for extending product lifespan and enhancing performance [2, 6, 7].

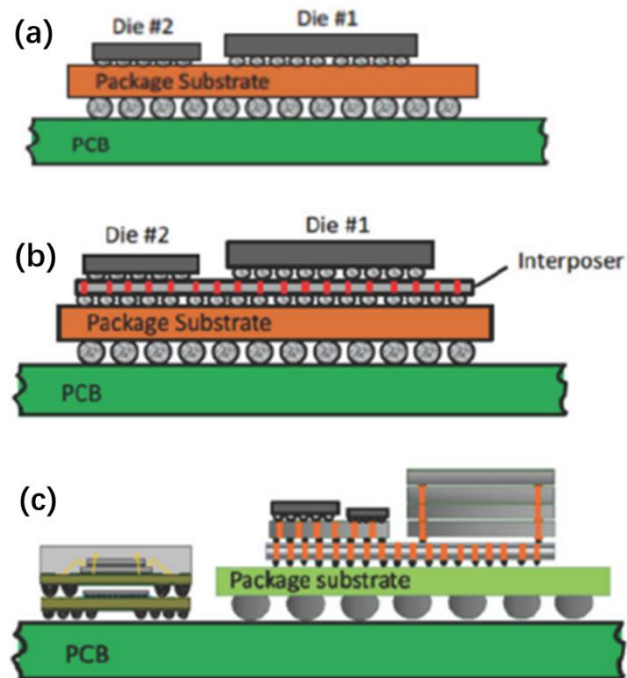


Figure 1.1 (a) 2D packages involve mounting two or more chips on the same level of the package base, (b) 2.5D introduces an intermediary layer between the chip and the base of the package, and (c) 3D packages vertically stack the chips. [4]

As shown in Figure 1.1, substrates play an essential function in packaging. The role of substrate materials is to support, fixed electronic components and their surface or internal formation of the circuit pattern can be connected to the circuit, as well as insulation, thermal transfer, isolation and protection of components. In the package, the heat was generated from the semiconductor and then transferred to the substrate. To meet the requirements of insulating and heat conduction, polymer materials are usually utilized in the substrate because of their good processability, electrical insulation, lightweight, and low cost [8, 9]. The most commonly used polymer substrate material is glass fibres reinforced epoxy. For example, FR4 is a well-known commercial material for printed circuit boards (PCBs). The polymer composite is combined with a glass fibre cloth to form a dielectric layer, which is coated with copper

on both sides to form a polymer composite substrate with a sandwich structure, as shown in Figure 1.2.

However, current polymer materials usually possess relatively low thermal conductivity (e.g. below $0.5 \text{ W m}^{-1} \text{ K}^{-1}$) [10-12]. The internal temperature of electronic products will continue to rise because of ineffective heat dissipation until some components are burned, resulting in thermal failure. Moreover, thermal stresses and warpage will occur in the high temperature working environment due to the varied coefficient of thermal expansions (CTEs) of each electronic components [13]. Therefore, thermally conductive materials with high thermal conductivity, excellent electrical insulation and a matching CTE with silicon are considered the optimal selection to solve the heat dissipation issue [14].

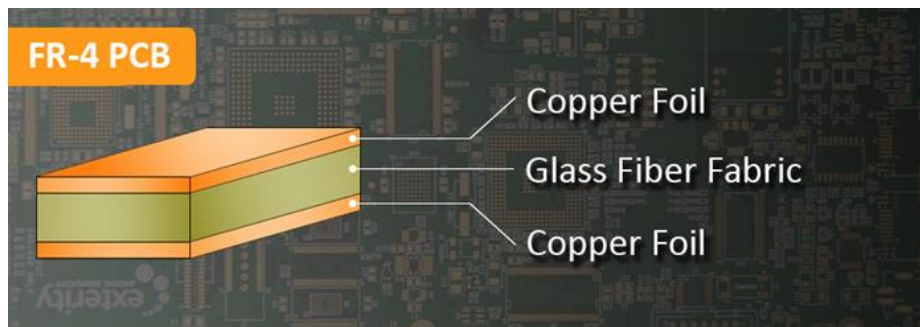


Figure 1.2 Schematic image of glass fibre reinforced substrate [15].

Polymer composites which include polymer matrix and thermally conductive fillers (e.g. Boron Nitride, Aluminium Nitride) have been proposed to improve the thermal conductivity [16-18]. In general, the fillers are introduced into the polymer by the method of solution mixing, which disperses the fillers randomly. However, the improvement of thermal conductivity for polymer composites is limited due to the lack of effective thermal transfer pathways. Many methods with a large amount of filler loading have been proposed to address this issue, but such high loading (50 wt%) resulted in the degradation of mechanical properties, heavy weight and high cost,

which limits the application of polymer composites [19, 20]. Thus, there is an urgent need to design thermally conductive composites with a less addition of loading to meet the requirements of advanced electronic devices. To achieve high efficiency of heat transfer in composites, continuous pathways of fillers need to be constructed to guarantee that most of the heat is transferred through the filler networks [21-23]. The methods for constructing continuous thermal transfer pathways of fillers include ice-templating (freeze-casting) [24, 25], vacuum-assisted filtration [26, 27], hot pressing [28, 29] and mechanical stretching [30, 31]. However, most methods are only successful in enhancing the in-plane thermal conductivity, so the utilization of fillers to improve both in-plane and through-plane thermal conductivities still demands further investigation.

Another severe issue in the electronic package is the mismatch of CTE of each constitutive element [32]. As the temperature changes, the package materials expand at different rates, leading to mechanical thermal stress and strain. The CTE of the silicon chip is only 3 ppm K⁻¹ [33]. However, the CTE of some substrate of polymer composites is much higher (20-60 ppm K⁻¹), especially in the Z direction [34]. For example, the CTE of current PCB materials-FR4 in the X-Y direction is about 12-16 ppm K⁻¹, but 80-90 ppm K⁻¹ in the Z direction [35]. Thus, it is necessary to develop novel polymer composites with desirable three-dimensional coefficients of thermal expansion. Previous study has shown that the epoxy composite with aligned filler layers significantly reduces CTE along the alignment direction at a low filler loading [36]. Therefore, constructing filler networks in polymer is an effective strategy for increasing the thermal conductivity while decreasing the CTE of the polymer composites.

1.2 Motivation and Innovation

1.2.1 Motivation

High thermal conductivity electrically insulating composites have important applications in many fields. As the electronics industry progresses rapidly, device integration is advancing towards higher densities, leading to a significant increase in power density per unit volume, thus generating a large amount of heat. If the accumulated heat is not efficiently dissipated promptly, localized hotspots will severely influence the efficiency, stability, and lifespan of electronic devices. High thermal conductivity composites therefore play a crucial role in modern electronics industry. These composites not only serve to support and fasten electronic components, but also to effectively dissipate heat. However, currently used composites have relatively low thermal conductivity, resulting in unsatisfactory heat dissipation that cannot meet the needs of modern electronic industry development. Electronic devices are rapidly changing various aspects of our lives, therefore, developing composites with high thermal conductivity is critically important.

Although polymer composites have been proposed to enhance thermal conductivity, the application of these composites is limited by the low thermal conductivity of polymers and the significant degradation of mechanical and processing properties following the addition of high filler content. Traditional methods for creating thermally conductive composites struggle to form effective thermal conduction pathways within the composites. Therefore, there is an urgent need to create oriented and orderly thermal conduction networks inside the system to achieve composites with high thermal conductivity. The deep understanding of the relationship between the structure and properties of thermal conductivity composites also needs to be established, to provide

a solid theoretical foundation for the industrialization of high-performance thermal conductivity composites.

1.2.2 Innovation

1. By employing efficient vacuum-assisted filtration and ice templating methods, an effective and well-ordered thermally conductive network is constructed within the polymer matrix. The heat in the composites mainly diffuses and transfers through the network formed by the thermal conductive fillers. Simply increasing the filler content does not guarantee the formation of an effective and well-ordered thermal conductive network. More importantly, it is imperative to manage the orientation of the thermal conductive networks to align them with the direction of heat flow. Achieving true connectivity of thermal conductive particles and forming controllable, stable, and structurally ordered thermal pathways through filtration and ice templating methods are the main innovative aspects of this study. The unique novelty from this work is to achieve stable silicon carbide (SiC) whisker 3D networks by sintering and forming vertically aligned fillers by vacuum-assisted filtration.
2. Micro-sized SiC whiskers are selected as raw materials. In previous studies, SiC nanofibers were commonly used for preparing aerogels using the ice templating method. SiC whiskers are more economical compared to SiC nanofibers.
3. The suitable sintering temperature and atmosphere conditions for SiC whiskers have been studied in detail for the first time in this thesis. Furthermore, the impact of sintering temperature on the thermal conductivity of the composite was investigated. The sintering was a new microstructure control method to reduce the interfacial thermal resistance between fillers.

4. This thesis studies the role of synergistic effect on dielectric properties and thermal properties by layering hybrid fillers of hexagonal boron nitride platelets (h-BN) and SiC whiskers into epoxy resin.
5. The vacuum-assisted filtration method is commonly used to create horizontal pathways for filler thermal conduction. This thesis innovatively applies the vacuum-assisted filtration method to construct vertical thermal conduction pathways, and simultaneously utilizes Graphene oxide (GO) as both a thermal filler and a bonding agent to enhance mechanical performance.

1.3 Aims and Objectives

Despite numerous studies have been summarized on thermally conductive composites in the literature review, several issues remain to be further investigated. For instance, the construction of 3D thermal conductive networks using SiC whiskers and the effect of sintering temperature on the thermal conductivity of composites; the synergistic effect of multilayer structured composites on thermal conductivity and dielectric properties; and finding more efficient methods to achieve vertical alignment of fillers to enhance through-plane thermal conductivity.

The aims of this research were to produce epoxy resin based polymer composites with fillers including SiC whiskers, h-BN platelets, and GO, which exhibit improved thermal conductivity and low CTE, and to investigate the relationship between the microstructure and thermal properties of these composites.

To achieve these aims, the specific objectives of the research were as follows:

1. To build the 3D network structure of SiC whiskers by freeze casting method. SiC whiskers will be mixed with polyvinyl acetate (PVA) as an adhesive in aqueous slurry followed by freeze casting to prepare SiC aerogels. The ratio of

SiC to PVA in the slurry will be adjusted to find a range that can maintain the structure of SiC aerogels. The sintering temperature and time as important factor will also be investigated. The target is to explore the conditions for preparing the optimal microstructure.

2. To align BN platelets and SiC whiskers by using the vacuum-assisted filtration method.

BN platelets and SiC whiskers will be aligned in the horizontal direction by using vacuum-assisted filtration method. Single layer BN, single layer SiC and BN/SiC bilayer will all be prepared for further investigation.

3. To achieve vertically aligned BN platelets using vacuum-assisted filtration method.

Firstly, BN will be aligned in the horizontal direction to get a 2 cm high sample. Then the sample will be cut into slices and rotate it 90 degrees. GO will also be added to explore the effect on sample preparation.

4. To impregnate epoxy resin into the aligned fillers.

The liquid epoxy resin will be impregnated into the fillers prepared before. In this process, temperature and vacuum time will be adjusted to obtain uniform composites without bubbles.

5. To characterise the morphology of the fillers and composites produced.

The characterisation methods, including X-Ray Diffraction (XRD), Scanning Electron Microscope (SEM) and Transmission electron microscope (TEM) will be used to study the microstructure and morphology of the samples.

6. To determine the thermal properties of the composites produced.

The thermal conductivity will be investigated with the laser flash method. The CTE will be determined via thermomechanical analysis.

7. To investigate the relationship between the microstructure and thermal properties. To explain the heat transfer mechanism with in-depth understanding the effect of the filler type, loading and alignment on thermal conductivity.

1.4 Outline of Chapters

This thesis has been organised into seven chapters. Chapter 1 gives a brief introduction to the background, objectives and structure of the thesis. Chapter 2 presents the literature review about thermally conductive polymer composites as well as their applications in different fields. Chapter 3 describes the experimental methods and details information on the characterisation technologies. Chapter 4 describes the construction of 3D SiC whisker networks in epoxy resin polymer to improve the thermal conductivity of composites by the freeze-casting method. Chapter 5 presents the role of synergistic effect on dielectric properties and thermal conductivity of the bi-layered h-BN and SiC epoxy composites. Chapter 6 discusses the enhancement of through-plane thermal conductivity and the reduction of the CTE of epoxy resin polymer achieved by vertically aligning BN and GO using vacuum-assisted filtration. Finally, the conclusions of this thesis and some future research suggestions are summarized in Chapter 7.

Chapter 2 Literature review

2.1 Background on thermal management materials

Thermal management addresses issues related to heat removal, thermal strain, and distortion. It holds a significant position in the packaging of power semiconductors and other electronic devices. In electronic devices, a large fraction of power loss transforms into heat. For instance, during the 1980s, the heat flux density of integrated circuits stood at approximately 10 W cm^{-2} , escalating to $20\sim 30 \text{ W cm}^{-2}$ in the 1990s. By 2008, this figure had reached nearly 100 W cm^{-2} . At present, the heat flux density at the chip level has surpassed 1 kW cm^{-2} , with the density at hot spots potentially hitting 30 kW cm^{-2} [37-39]. To guarantee the prompt dissipation of the substantial heat produced by electronic components, materials for thermal management have emerged as a crucial factor in the design and assembly of microelectronic product systems. The electronic chip packages are consisting of several different materials. Semiconductors and ceramics exhibit CTEs between 2 ppm K^{-1} and 7 ppm K^{-1} , whereas the CTEs for copper, aluminium, and glass fibre-reinforced polymer PCBs are significantly greater (17 to 80 ppm K^{-1}) [13, 40]. Thermal stresses and warpage in each component mainly result from the variation in CTEs. Therefore, polymer composites need to be developed to possess both low CTE and high thermal conductivity.

2.2 Mechanism of heat transfer in polymer composites and key influencing factors

2.2.1 Mechanism of heat transfer in polymer composites

The process of heat transfer involves the flow of heat through solids, liquids, or gases or between two closely interacting media. Heat transfer occurs through three

fundamental mechanisms: thermal radiation, thermal convection, and thermal conduction [41]. Among these, within the interior of solids, heat transfer primarily occurs through thermal conduction. This thesis is dedicated to exploring the internal heat transfer capacity of polymer matrix composites, therefore only the heat conduction part is discussed.

The heat conduction mechanism in solids can be classified into electron conduction and phonon conduction. Free electrons are the thermal carriers in metals and a limited number of conductive polymers (such as polyacetylene, polypyrrole and polyaniline) [42]. These electrons, characterised by their small volume and high mobility, can freely move without being constrained by the lattice positions in crystalline substances, efficiently transferring heat through mutual collisions. Therefore, bulk materials that conduct heat through free electrons typically exhibit high thermal conductivity. However, the presence of free electrons also imparts excellent electrical conductivity to the materials, which may limit their application when electrical insulation is required.

In most polymer and ceramic materials, heat conduction is primarily achieved by lattice vibration and molecular chain vibration, and the carrier of heat energy is mainly phonon. Compared with some polymer materials, the lattice structure of ceramic is more ordered, which means phonons are able to travel in the direction of the lattice, and have larger average free paths, so the bulk ceramics show higher thermal conductivity.

In polymer materials, polymer chains are intertwined, which is not conducive to the high-speed motion of phonons. There are serious scattering and propagation direction changes of phonon at the interface of the polymer chain, and the average free path of

phonon is significantly reduced across the polymer chains, which determines that polymers exhibit low thermal conductivity [43]. Most insulating polymers display thermal conductivities between 0.1-0.5 W m⁻¹ K⁻¹, as shown in Table 2.1 [8, 10, 44, 45].

Table 2.1 Thermal conductivities of polymers commonly used as matrix [8, 10, 44, 45].

Materials	Thermal Conductivity (W m⁻¹ K⁻¹)
Epoxy resin	0.19
Polycarbonate (PC)	0.20
Polypropylene (PP)	0.11
Polystyrene (PS)	0.14
Polyimide, Thermoplastic (PI)	0.11
Polyetheretherketone (PEEK)	0.25
Polyvinyl chloride (PVC)	0.19
Polyvinylidene difluoride (PVDF)	0.19
Polyphenylene sulfide (PPS)	0.30
Polytetrafluoroethylene (PTFE)	0.27
Poly(ethylene vinyl acetate) (PEVA)	0.34
Poly(dimethylsiloxane) (PDMS)	0.25

The internal disordered arrangement of molecular chains and the presence of a significant amount of non-crystalline regions in polymers lead to extensive phonon scattering, restricting the use of polymers due to their low thermal conductivity [46]. To overcome this limitation, certain polymer processing techniques can be employed during polymer synthesis or processing to enhance the orientation of a portion of polymer chains or introduce new microstructural units. This can partially improve the

intrinsic thermal conductivity of polymers. Numerous researchers have explored the study of intrinsic polymers, employing techniques such as orientation methods to induce locally ordered structures along specific directions of internal molecular chains, and incorporating liquid crystal rigid elements into the matrix to enhance the thermal conductivity of polymers [47-49]. However, intrinsic polymer research is predominantly focused on the microscopic scale, presenting challenges in characterisation, limited improvements in thermal conductivity, and complexities in processing, hindering large-scale production. Therefore, the current mainstream approach remains adding thermally conductive fillers into the polymer matrix to prepare composites.

Table 2.2 Thermal conductivities of commonly used thermally conductive fillers [10, 50-54].

Materials	Thermal Conductivity ($\text{W m}^{-1} \text{K}^{-1}$)
Diamond	2000
Graphite	100~400 (on plane)
Graphene	2000~6000
Carbon nanotubes	2000~6000
Boron Nitride (BN)	250~300
Aluminium nitride (AlN)	200~319
Aluminium oxide (Al_2O_3)	20~29
BeO	270
Silicon carbide (SiC)	120

In thermally conductive composites, the improvement of thermal conduction is mainly from the contribution of heat conduction fillers, which is related to the type of fillers, distribution of fillers, the content of fillers and the thermal resistance of interface. The

thermal conductivities of fillers which are commonly utilized are listed in Table 2.2. At lower filler loadings, they remain isolated within the polymer matrix (Figure 2.1). Thus, in the matrix, there is no sufficient connection between the isolated fillers to form thermal conduction pathways, which limits the improvement of the thermal conductivity of composites. As filler loading is further increased to the percolation threshold, fillers begin to contact each other to form macroscopic heat conduction networks, which can provide a channel for the high-speed transmission of phonons (Figure 2.1). As depicted in Figure 2.2, the thermal conductivity of the composite shows a significantly increase after the percolation threshold point [55]. Furthermore, efficient heat transfer is achieved when the heat transfer direction is aligned with the heat conduction network. In conclusion, enhancing the thermal conductivity relies on establishing highly oriented thermal conduction networks in the polymer matrix.

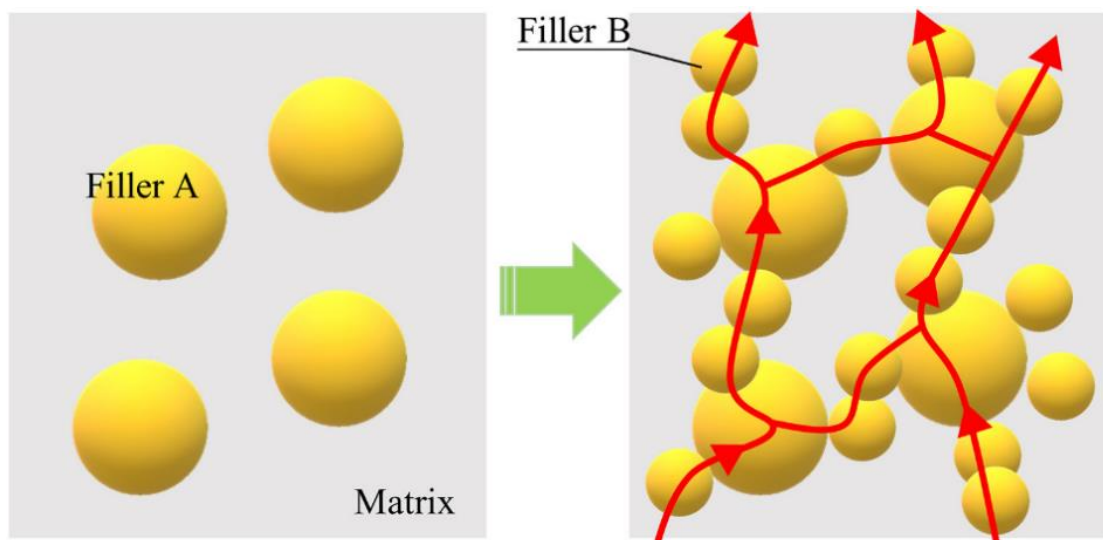


Figure 2.1 The distribution state of fillers in the polymer matrix.

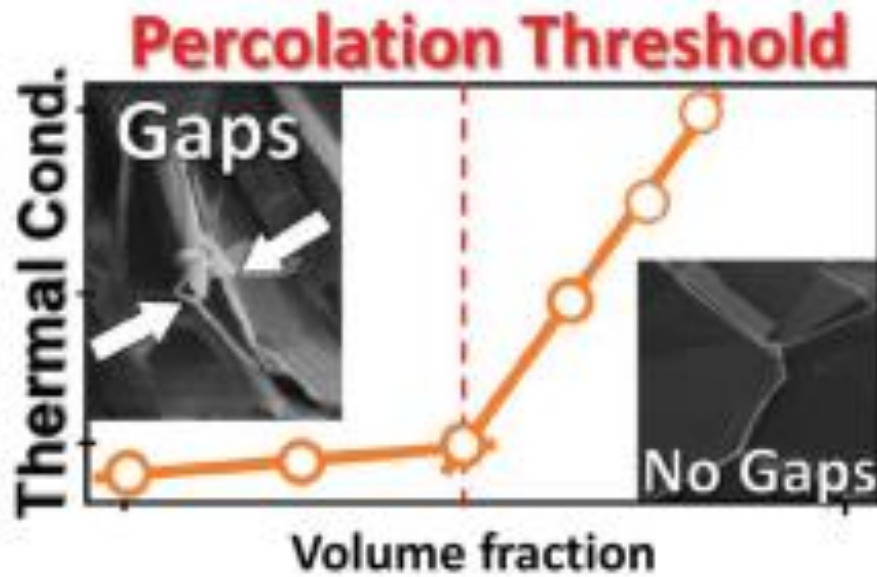


Figure 2.2 Percolation-like behaviour with the loading fraction increased during which the pathway between two connected fillers increases [55].

2.2.2 Key influencing factors

(1) Intrinsic properties of thermally conductive fillers.

The properties of the fillers (including the intrinsic thermal conductivity of the fillers, shape, size, etc.) influence the thermal conductive properties of polymer matrix composites. For the same materials, the crystal structures and defects of fillers are the important factors that influence intrinsic thermal conductivity of fillers [56]. In actual substances featuring defective lattice structures, the average distance phonons travel and heat transfer efficiency are constrained as well due to the impact of phonon scattering phenomena resulting from defects, boundaries, etc [57]. Different fillers have different intrinsic thermal conductivities, such as the theoretical intrinsic thermal conductivity of AlN is $319 \text{ W m}^{-1} \text{ K}^{-1}$ [58], SiC is $120 \text{ W m}^{-1} \text{ K}^{-1}$ [59], and diamond intrinsic thermal conductivity is $2000 \text{ W m}^{-1} \text{ K}^{-1}$ [50], as shown in Table 2.2. In addition, the size of the fillers also affects the thermal conductivity of the composites. When the volume fraction of BN fillers remains constant, composites the silicone

rubber composite incorporating larger-sized (20 μm) particle fillers exhibits greater thermal conductivity compared to one utilizing fillers of smaller (0.3 and 6.0 μm) particle sizes, because composites with larger fillers have less filler/polymer interface leading to lower interface thermal resistance [60]. However, this situation does not occur for all composites, as there are controversial studies on the effect of particle size. Zhou et al. investigated silicone rubber with various particle size of Al_2O_3 fillers and discovered that the thermal conductivity of composites with 5 μm Al_2O_3 fillers was slightly higher compared to those with Al_2O_3 fillers of 25 μm and 0.5 μm at 64 vol% loading [61]. As filler loading increases, the thermal conductivity of composite improves due to the compact packing structure of the particles, with finer 5 μm particles achieving higher packing density and better thermal conductivity than 25 μm particles. However, when the particle size of the filler is at the nanoscale, the nanoparticles may exhibit unique physical and chemical properties that differ significantly from their bulk counterparts due to their small size and high surface area to volume ratio. Nanomaterials are materials that have at least one dimension in the nanometre scale, typically ranging from 1 to 100 nanometres. Consequently, the thermal conductivity of polymer composites prepared with nanoscale fillers may not necessarily be lower than that of composites prepared with micrometre-scale fillers [8, 62].

The geometry of fillers profoundly influences the thermal conductivity of polymer composites. Distinct dimensions of fillers (zero-dimensional spherical, 1D linear or rod-like, 2D sheet-like, and 3D honeycomb-like) determine factors such as filler dispersion, contact area, and contact modes during filler interlacing [22]. These factors result in variations in the number and quality of constructed heat transfer pathways, subsequently impacting the extent of their contribution to thermal conductivity in

composites. Compared with zero-dimensional materials, 1D materials and 2D materials with ultra-high aspect ratios can form a large contact area between the fillers, which provides a wider path for the transfer of phonons and reduces the interface thermal resistance. Under the same preparation conditions, for instance, the contact area of 1D fillers may be smaller than that of 2D fillers, leading to differences in the thermal conductivity of the prepared polymer-based composites. Su et al. [63] investigated the thermal conductivity of epoxy resin-based composites filled with BN nanosheets and BN nanotubes. The study revealed that the thermal conductivity of the BN nanosheet/epoxy resin composites is higher than that of the BN nanotube/epoxy resin composites.

(2) Distribution of fillers

The creation of pathways for phonon thermal flow hinges on the interaction among filler particles and the formation of the network structure. When the amount of filler is comparatively minimal, a small quantity of fillers is randomly dispersed within the matrix, forming an "island-sea" structure where they exist in isolation with minimal contact between them, and as a result, thermal conductivity has very small increase. With the continuous increase in filler content or adjustments in the preparation process, the filler particles gradually come into contact with each other, eventually forming a continuous phase that traverses the entire composites [64]. Creating a thermal conduction pathway enhances thermal conductivity by enabling heat transfer via electrons or phonons along the path of least thermal resistance, according to thermal conduction path theory.

According to the thermal conduction path theory, establishing a connected thermal conduction network within the polymer matrix can form high-efficiency thermal

conduction paths, facilitating effective heat transfer [65]. For fillers randomly dispersed in the polymer, the thermal conduction networks need to be established through the sufficient stacking of a considerable quantity of filler materials. In other words, the random dispersion of fillers hinders the interconnected required for the formation of thermal conduction paths, leading to less enhancement of thermal conductivity in polymer-based composites. It has been reported that it is necessary to add over 50 wt% of BN (8 μm) fillers to the epoxy-terminated dimethylsiloxane to achieve a tenfold increase in thermal conductivity [8, 66]. In contrast to the random dispersion of fillers, a small amount of fillers can enhance the thermal conductivity of composites by forming a connected thermal conduction network within the polymer, providing thermal transfer paths for heat transfer.

2.3 Solutions and limitations of improving thermal conductivity of polymer composites

Currently, the fillers used to prepare thermally conductive insulating polymer nanocomposites are carbon (carbon nanotubes [67], graphene [68]), metals (silver [69], copper [70]), ceramic. Ceramic fillers include nitrides, such as BN [71] and AlN [72], etc.; oxides, such as magnesium oxide (MgO) [73] and beryllium oxide (BeO) [74]; carbides, such as SiC [59].

Metals have excellent thermal and electrical conductivity. However, these fillers themselves have very high electrical conductivity leading to the increase of electrical conductivity of composites. Therefore, metallic fillers are suitable only for applications where electrical insulation and the threshold for voltage breakdown are not essential considerations.

In carbon-based thermally conductive polymer materials, fillers mainly include carbon fibre, graphite, carbon nanotubes, diamond and graphene. Carbon fillers can remarkably enhance the material's ability to conduct heat with a small amount of addition, which is lighter than metal fillers and inorganic fillers. Unfortunately, carbon-based filler itself also has a high electrical conductivity, which limits its application in the field of insulation. Within the domain of composites that are both thermally conductive and electrically insulating, such conductive additives are often coated with either an organic or inorganic insulating layer. This coating aims to restricting the filler's conductivity, yet it preserves the composites' high ability to transfer heat. For example, Noma et al. used a sol-gel method to coat the surface of graphite particles with a layer of silica dioxide (SiO_2) [75]. When the filler volume fraction was 22.9%, the thermal conductivity of the polymer composites reached $3.3 \text{ W m}^{-1} \text{ K}^{-1}$. At the same time, it has a good insulation performance. When a voltage of 500 V is applied, the volume resistivity of the composites is $>1.0 \times 10^{14} \Omega \text{ cm}$.

The traditional method of mixing is very limited to improving the thermal conductivity of composites. In order to achieve high thermal conductivity with a relatively low filling amount, a lot of research has been carried out in recent years.

2.3.1 Functionalization of filler surface

The synergy between the fillers and the polymer matrix significantly impacts the composite's thermal conductivity. By modifying the filler's surface, the interaction between the filler and the matrix can be improved, leading to better filler dispersion within the matrix. This optimization of the phonon transport path minimizes the thermal resistance at the interface, thereby elevating the composite's thermal

conductivity [76, 77]. There are two methods for the functionalization of the filler surface: covalent functionalization and non-covalent functionalization [78].

(1) covalent functionalization

Covalent functionalization is to graft some chemical groups on the surface of the filler through a covalent bond by a chemical reaction, thereby enhancing the interface interaction between the filler and the matrix. Common methods include strong acid oxidation, solvent assisted ball milling and coupling agent treatment [79].

(2) non-covalent functionalization

Non-covalent functionalization uses electrostatic interactions between fillers and modifiers, π - π interactions, Van der Waals forces, and hydrogen bonds to achieve filler surface functionalization [80, 81]. Compared with covalent functionalization, non-covalent functionalization has the advantages of not damaging the filler structure and is easy to operate.

Teng et al. non-covalently functionalized graphene nanosheets (GNs) through polyglycidyl methacrylate modified with pyrene molecules, promoted the dispersion of GNs in the polymer matrix [80]. The improved interface interaction significantly improves the thermal conductivity of GNs/epoxy composites.

2.3.2 Hybrid particles

Enhancing the thermal conductivity of the composites with just one type of filler is limited. Hybrid fillers of various types, morphologies, and sizes into a composite facilitates synergistic interactions among the fillers, leading to a higher thermal conductivity [64, 82, 83]. Xu et al. used AlN whiskers and AlN particles as fillers in

PVDF-based composite [84], and achieved a thermal conductivity up to $11.0 \text{ W m}^{-1} \text{ K}^{-1}$ at 60 vol% filler loading. .

2.3.3 Oriented fillers

However, currently, there are also some limitations of current polymer composites. First, the process of surface functionalization is too complicated, and the improvement of thermal conductivity is limited. Second, a large amount of fillers is still needed to achieve higher thermal conductivity, which results high cost. Third, the studies are more focused on improving thermal conductivity rather than how to reduce CTE. Thus, it is essential to find an efficient way to improve the thermal conductivity of composites.

The key to preparing high thermal conductivity composites is to form thermally conductive pathways in polymer matrix. For composites prepared by simply mixing, the fillers are randomly distributed, which is not conducive to achieving high thermal conductivity. Materials with a 1D structure and a high aspect ratio, like carbon nanotubes and carbon fibres, along with 2D materials, such as graphene and hexagonal BNNS, exhibit thermal conductivity along their length direction that significantly surpasses their radial thermal conductivity. When aligned, these materials can fully leverage their super thermal conductivity in the longitudinal direction. Currently, numerous techniques have been explored to align the fillers, including the doctor blade method [71, 85], application of electric and magnetic fields [86], filtering [87], hot pressing [88], and electrospinning [89], etc. These will be introduced in detail in the next section of this thesis.

2.4 Distribution control of thermally conductive fillers in polymer composites

Introducing thermal conductive fillers into the polymer is a common approach to preparing high thermal conductivity composites. Effectively controlling the distribution of fillers within the polymer matrix is a key method for establishing thermal conduction pathways. The commonly used nano fillers including BN nanosheet (BNNS), BN nanotube (BNNT) and SiC fibre have anisotropic heat transfer properties. These fillers can be oriented in the process of preparing composites, which significantly enhances the thermal conductivity of composites in the orientation direction of fillers. Therefore, according to the orientation of thermally conductive fillers in the polymer, thermal conductive composites can be classified into three distinct groups: (1) polymer composites with randomly distributed fillers; (2) polymer composites with 2D aligned fillers; (3) polymer composites with 3D structural network of fillers.

2.4.1 Polymer composites with randomly distributed fillers

Solution simply mixing is the prevalent technique for dispersing fillers randomly within polymer composites. The composites are obtained by mixing the thermally conductive fillers with the liquid polymer or the solid polymer dispersed in the solvent evenly and then placing it in the mould for curing. In the past decade, scientists have conducted many studies on the randomly distributed filler in polymer composites. Surface functionalization of fillers was usually employed to enhance the thermal conductivity of such materials. The AlN filled with epoxy resin composite has been proposed by Tanaka et al., as shown in Figure 2.3 [90]. They made different surface modifications to AlN, including surface grafting of silane, epoxy, mercapto and other

functional groups. The results show that the maximum thermal conductivity of the composite is $6 \text{ W m}^{-1} \text{ K}^{-1}$ when the AlN content is 65 vol%.

Hybrid fillers are additionally employed to enhance thermal conductivity of randomly distributed fillers polymer composites. Qi et al. prepared PVDF composite using three different sizes BN particles mixed with carbon nanotubes (CNTs). As shown in Figure 2.4, the final dispersion states of CNTs in PVDF composites were affected by the shape of BN particles [91]. The results exhibit that the largest thermal conductivity is $2.18 \text{ W m}^{-1} \text{ K}^{-1}$, which demonstrates that the middle size of BN particles ($8.70 \mu\text{m}$) is the most proper filler to construct high efficiency heat conductive pathways with CNTs in PVDF/BN/CNT composite.

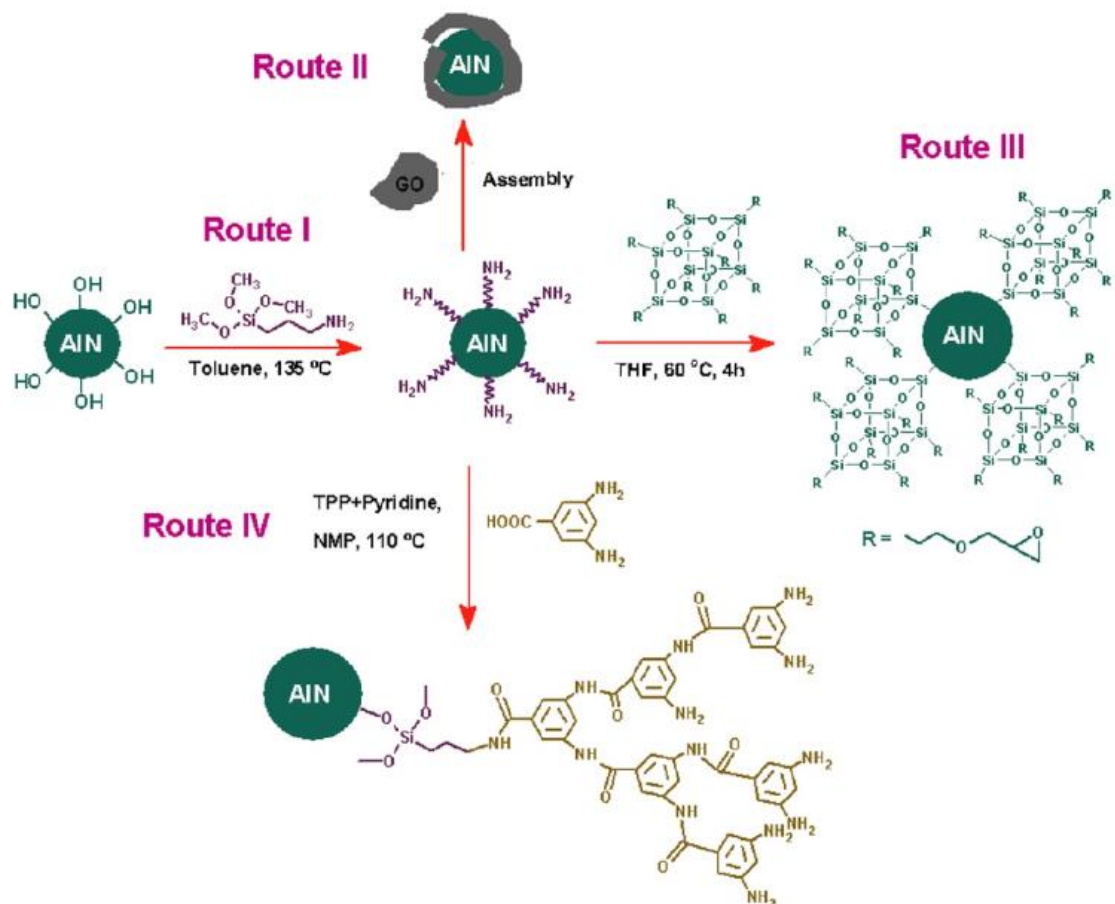


Figure 2.3 Surface treatment of AlN particles [90]

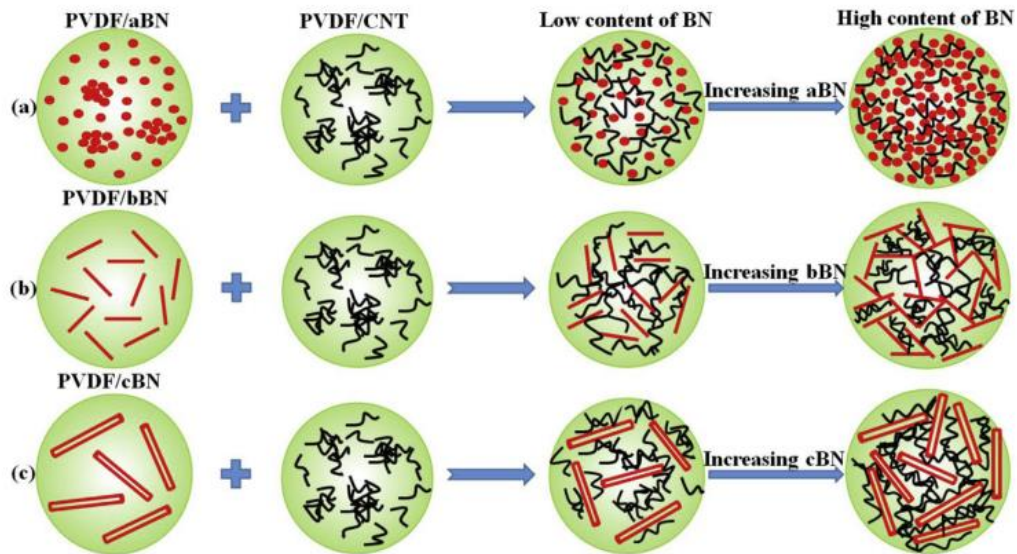


Figure 2.4 Schematic of preparing PVDF/BN/CNT composites with three different sizes of BN [91].

Although inorganic fillers have high thermal conductivity, random distribution fillers polymer composites are limited in practical application. Recently, oriented fillers polymer composite has attracted more and more attention due to the following shortcomings of randomly distributed fillers polymer composite. Firstly, the essential factor to improve thermal conductivity is to construct heat transfer pathways. In polymer composites, polymer, as a poor conductor of heat, mainly provides mechanical and electrical insulation support, while heat flow is mainly conducted through thermal conductive fillers. The random dispersion of fillers results in a large amount of fillers/polymer interfaces, leading to elevated thermal resistance. Severe phonon scattering occurs at the interfaces, which affects the heat conduction in composites. Secondly, only increasing the content of thermally conductive fillers can improve thermal conductivity, but it will lead to the degradation of mechanical properties and seriously affect its processability. Thus, it is still a challenge to improve the thermal conductivity without damaging the mechanical properties. Thirdly, high filler content will undoubtedly increase the cost of composites.

2.4.2 Polymer composites with 2D aligned fillers

Many thermally conductive fillers have anisotropic heat conducting properties. They can be oriented during specific processing and form oriented heat conducting pathways in the composite, which makes the materials have better heat conducting properties in the orientation direction [59]. In many applications, thermally conductive composites are required to have a high thermal conductivity in a specified direction. Therefore, in the research of thermally conductive composites, achieving high thermal conductivity in a specified direction has attracted much attention. As shown in Figure 2.5, many methods have been put forward to oriented fillers, including injection moulding [92], doctor blading [71, 85], stretching [93], vacuum-assisted orientation [87], electromagnetic field orientation [86], hot pressing [88], ice template method [59], electrospinning [89] etc.

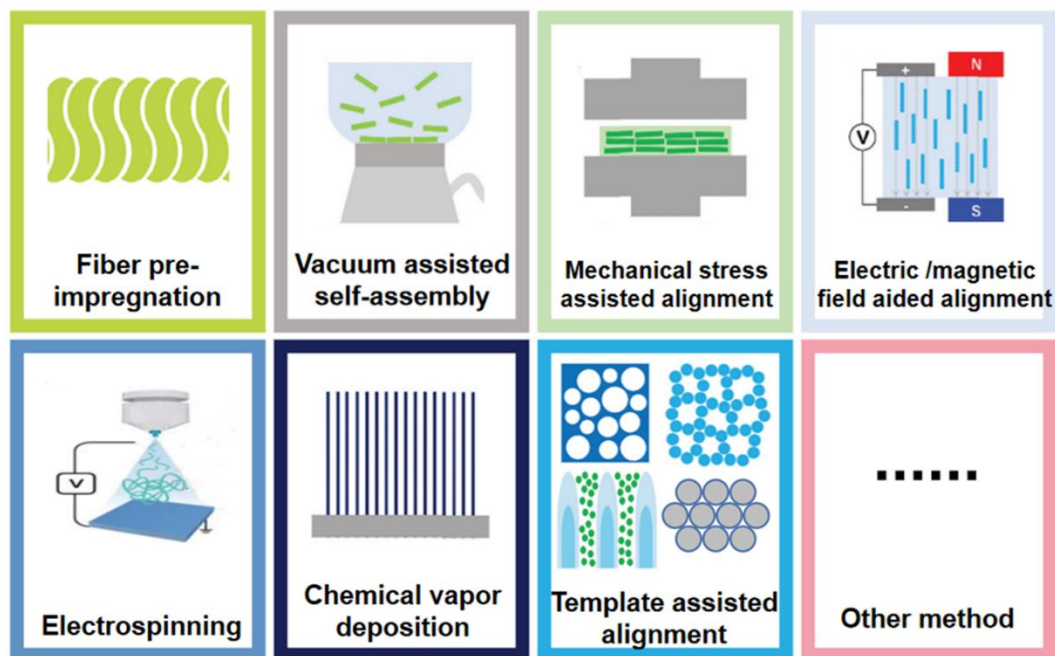


Figure 2.5 The methods for alignment of fillers in polymer [94].

Injection moulding is a typical method of orienting anisotropic fillers. When a mixture of polymers and fillers is injected through a mould, the applied shear stress causes the fillers to be oriented in the injection direction [95]. The Al_2O_3 fibres whose average diameter is 10 μm form a good orientation in a high-density polyethylene matrix [92]. Compared with the random dispersion of Al_2O_3 fibres, the thermal conductivity of composite in the injection direction improves by 17.5%. By using the injection moulding method, various types of moulds can be designed according to the requirement of practical application. Users can orient the fibrous filler according to the shape of the mould. Injection moulding is suitable for the low injection flow rate. The orientation of fillers in composites gradually disappears at a high injection flow rate owing to the influence of the interaction between the fillers [96].

In contrast, **doctor blading (or tape casting)** is a simple technique for horizontally orienting fillers. Doctor blading does not require special moulding equipment, and the preparation process is simple and continuous, so it is suitable for large-scale production. Cast moulding is divided into two steps, first the blend of fillers and polymer is deposited onto a substrate, allowing it to spread naturally under gravitational forces. The mild shear stress produced in this process can orient the fillers. Second the blade moves at a speed up to several meters per minute to control the thickness of the films. At the boundary of the blade, the movement of the blade will cause the fluid to flow and generate strong shear stress. The shear force causes the anisotropic fillers to form an orientation along the direction of the fluid flow [97].

Xu et al. prepared BN/polyvinyl alcohol (PVA) film by doctor blading [71]. The SEM image in Figure 2.6 shows that the shear stress brought by the blade caused BN to form a good horizontal orientation in the PVA matrix, while the composite interface prepared without the doctor blading process showed a randomly scattered BN

distribution. The in-plane thermal conductivity of composites is 5.4, 7.6, and 8.8 W m⁻¹ K⁻¹ respectively, when the BN content is 10, 20, and 30 vol%. At the same BN content, the in-plane thermal conductivity of composites prepared by the doctor blading is increased by more than 13.5% than that of the composites prepared by the simply mixing. In addition, the blade can uniformly control the thickness of the film, so that the composite film has a transmittance within a certain range of BN content.

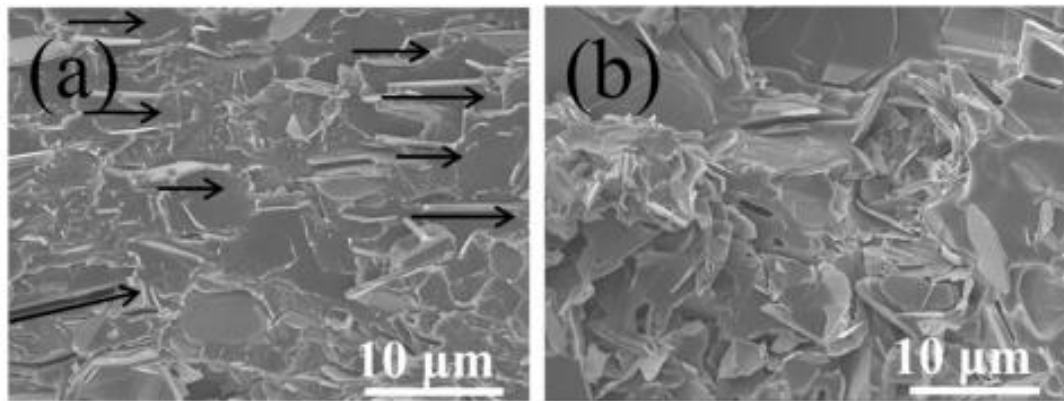


Figure 2.6 Cross-section micrograph of the composites prepared (a) by doctor blading (b) by casting only [71].

Vacuum-assisted orientation is the method of forming anisotropic thermally conductive fillers into a horizontal orientation which is similar to doctor blading. The difference is that doctor blading is based on shear stress, while vacuum-assisted orientation is based on fluid forces [98]. Figure 2.7 shows the flow chart of vacuum-assisted filtration assembled process for BNNS/cellulose nanofibers (CNFs) film [99]. The fillers and solvent are mixed and placed in a vacuum-assisted filtration system. Then because of the vacuum force at the bottom, the solvent will flow downward and penetrate through the holes of the sand core, thereby generating liquid flow force. The fillers will move to the bottom under the action of liquid flow force. In order to maintain the stability of its structure, the fillers will tend to be arranged horizontally

to form a densely layered structure. The higher vacuum degree leads to a higher degree of orientation in the in-plane direction.

Zeng and others used BNNS as the basic assembly unit and PVA as the polymer matrix to prepare thin-film materials with similar microstructure to natural shells based on vacuum-assisted filtration technology [87]. SEM images (Figure 2.8) show that the cross-section of the composite presents a perfect layered structure, in which BNNS are closely stacked with each other. The contact interface provides a large heat transfer area. BNNS forms an oriented heat conduction path which improves the in-plane thermal conductivity of the composite to $6.9 \text{ W m}^{-1} \text{ K}^{-1}$. The essence of vacuum-assisted orientation is to establish a framework in which the fillers contact with each other, and then use a polymer to fill the gap between the fillers, which is suitable for the preparation of ultra-high filler content composites.

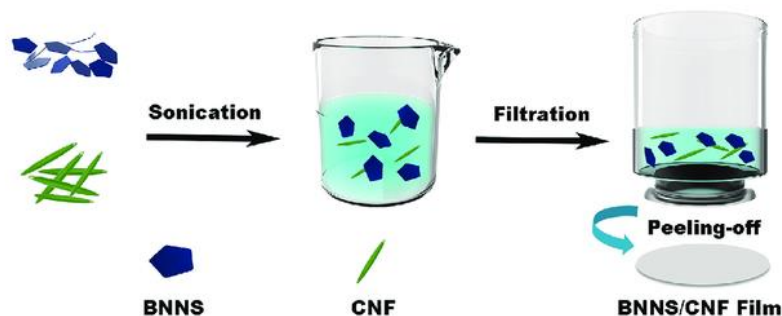


Figure 2.7 Schematic of the composite preparation by vacuum filtration force [99].

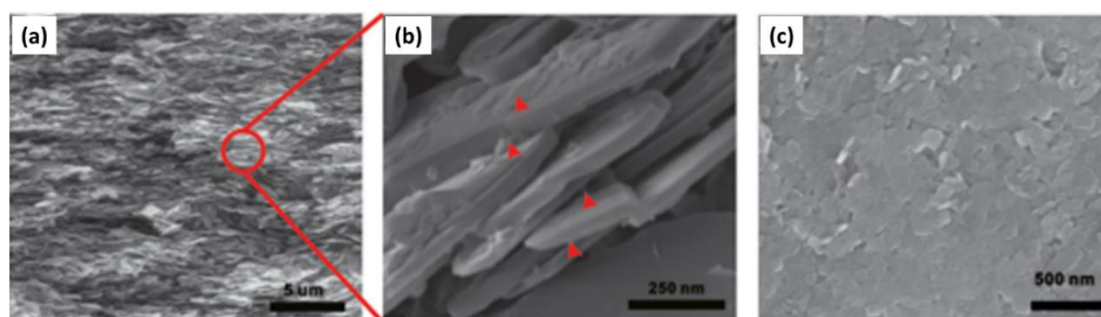


Figure 2.8 The SEM images of the (a-b) cross-section (c) surface morphology of NF-BNNS-PVA paper. Red arrows in (b) indicate the bridges between platelets. [87]

Electromagnetic field orientation also serves as an efficient approach to realize the orientation of fillers in specific directions [100]. Most ceramic fillers themselves are not intrinsically magnetic materials. Therefore, it is necessary to perform surface modification treatment on the ceramic fillers in advance, making ceramic fillers oriented in a magnetic field, such as loading magnetic particles on the surface. Kim et al. loaded magnetic (ferroferric oxide) Fe_3O_4 particles on the surface of AlN and used a magnetic field to form an orientation inside the epoxy matrix (Figure 2.9) [101]. When AlN content is 20 vol%, the through-plane thermal conductivity of epoxy composites with randomly distributed AlN is $0.915 \text{ W m}^{-1} \text{ K}^{-1}$, and thermal conductivity rises to $1.754 \text{ W m}^{-1} \text{ K}^{-1}$ after magnetic field orientation. The principle of electric field orientation is similar to that of magnetic field orientation, which causes fillers to be indirectly affected by external forces [102]. Anisotropic fillers such as nanosheets and nanowires are polarized when an electric field is applied. Electric field-induced torque acts on the fillers to form a linear array. The main disadvantage of electromagnetic field orientation is that it needs a long time to orient the fillers. In a viscous polymer matrix, it often takes several hours to achieve the orientation of the filler, which limits its practical application.

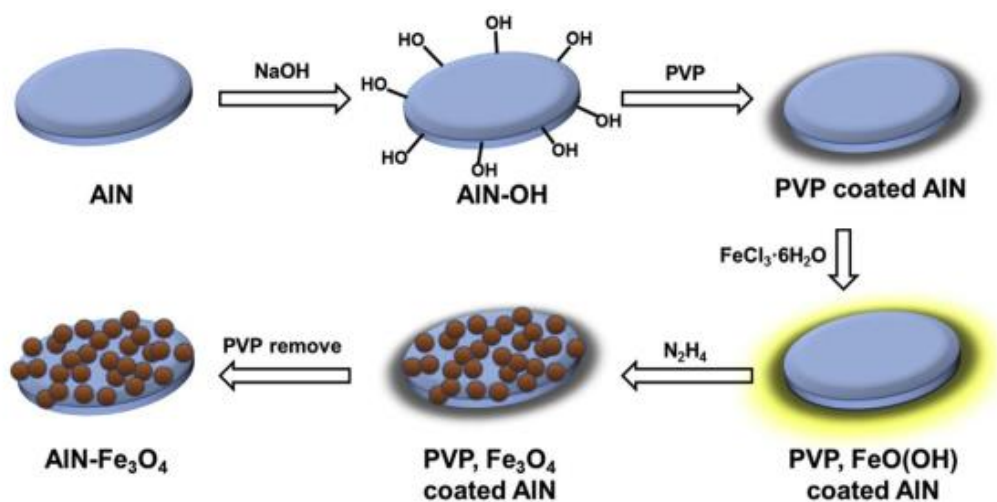


Figure 2.9 Fabrication procedure of the AlN-Fe₃O₄ hybrid filler [101].

Hot pressing uses mechanical forces to orient fillers. Initially, fillers are evenly blended with the polymer matrix, followed by subjecting the mixture to elevated temperature and pressure. Under pressure, the anisotropic fillers will tend to be aligned along the long side [103, 104]. The mechanism of heat transfer enhancement is similar to doctor blading and vacuum-assisted orientation [105-107]. The hot pressing and electrospinning methods can be combined to achieve the oriented arrangement of fillers. Yang et al. prepared BNNS/PVA thermally conductive composite films by electrospinning technology, followed by hot-pressing, and the fabrication process is illustrated in Figure 2.10 [105]. The in-plane thermal conductivity of BNNS/PVA film with 30 wt% BNNS significantly enhanced to $18.63 \text{ W m}^{-1} \text{ K}^{-1}$.

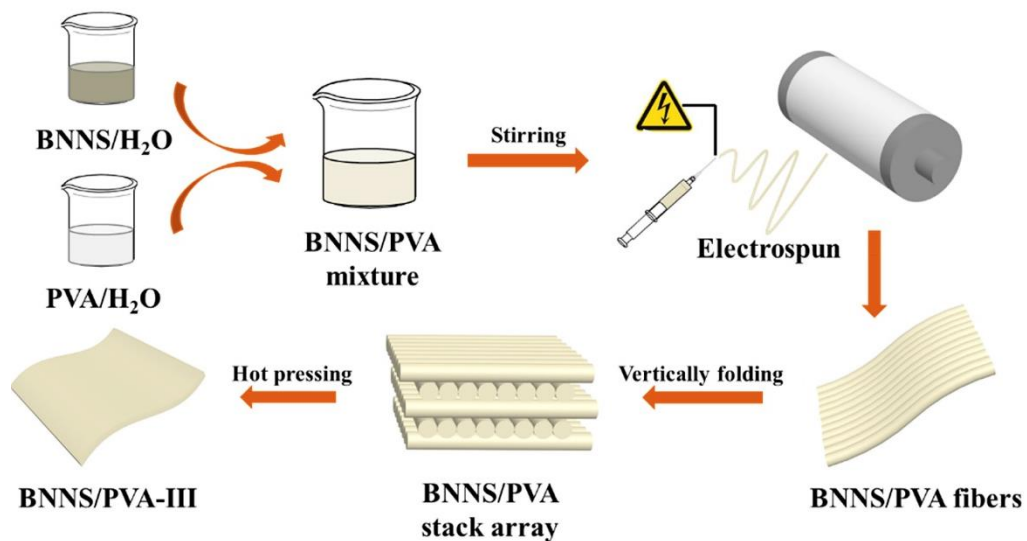


Figure 2.10 Schematic of the process for preparing BNNS/PVA films [105].

Stretching method is also applied to horizontally aligned fillers in composites [108, 109]. The tensile force generated during the stretching process can induce the fillers to align in the direction of the applied force. The BN/PVA film underwent stretching at ambient temperature, with a steady force manually applied to its elongated edges until the desired draw ratio was achieved. [93]. The in-plane thermal conductivity of stretched BN/PVA film which is twice the original length reached $30 \text{ W m}^{-1} \text{ K}^{-1}$ with

50 vol% BN. However, the issue is that when the film is stretched to twice its length, there is a noticeable necking phenomenon. The significant contraction occurring locally within the sample causes a reduction in the tensile strength of the film.

2.4.3 Polymer composites with 3D network fillers

Recently, researchers have paid more attention to constructing 3D heat conduction networks in polymer composites. Compared with the traditional inorganic particles randomly distributed in the polymer, the composite which has a 3D heat conduction network significantly improves the thermal conductivity at low content of fillers [59]. Several methods have been used to fabricate 3D structure networks in polymer composites.

self-assembly

In the preparation of composites, utilizing the filler self-assembly process to construct a thermal conductivity network is an important and efficient method to improve the thermal conductivity of materials.

A novel method of preparing a 3D BNNS network by using 3D cellulose as a skeleton based on the sol-gel and freeze-drying process has been reported by Chen et al. (Figure 2.11). In this study, the hydrogen bonding was used to attach the BNNS onto the cellulose fibres by the self-assembly method. At a BNNS content of 9.6 vol%, the thermal conductivity achieved $3.13 \text{ W m}^{-1} \text{ K}^{-1}$, which is 1400% higher than that of pure epoxy resin [110]. The results indicate that this method can significantly improve the thermal conductivity of BNNS composite at a low filler loading.

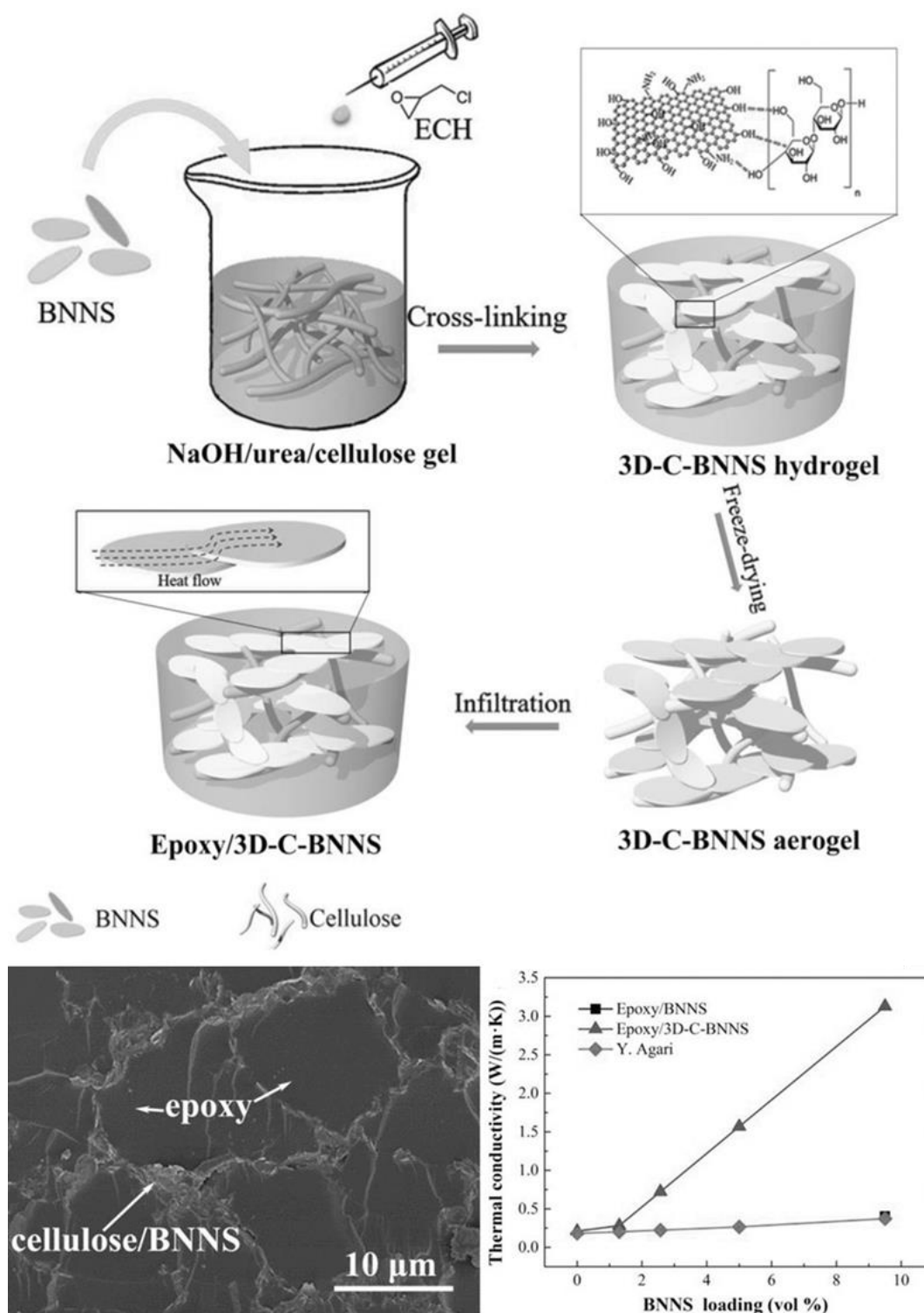


Figure 2.11 Schematic of 3D BNNS network preparation using sol-gel technique, and influence of BNNS loading on the thermal conductivity [110].

Freeze-casting (ice-templating) method

Freeze-casting or named ice-templating is a common method for preparing porous ceramics which has been used to prepare 3D filler networks in recent years [59, 111, 112]. The core principle of the ice templating technique involves controlled solidification, utilizing the ice crystals that emerge during the freezing of water as a template to create a structured network of fillers. [113].

The freeze casting process is illustrated in Figure 2.12 [114]. First, the slurry is poured into the mould and followed by freezing, then putting the frozen suspension into a vacuum circumstance to sublimate the frozen phase. There are two kinds of freezing methods which are homogeneous freeze casting and directional freeze casting. Homogenous freezing means the temperature distribution is uniform throughout the sample. By using this method, the microstructure of the sample is uniform since ice crystal growth is the same in all directions. However, when the freezing temperature distribution has a gradient, the ice crystal will grow along the temperature gradient. In the whole process, the state of slurry which is expected to be stable and dispersed uniformly is critical [115]. The most critical stage is the solidification of the prepared suspension because the crystal morphology determines the obtained microstructures which are homogeneous or directional. The crystal morphology is controlled by the freezing conditions, solid loading and solvent type; as a result, the structure of the materials can make a great change accordingly. Figure 2.13 shows the relationship between the freezing process and aqueous slurry states [116].

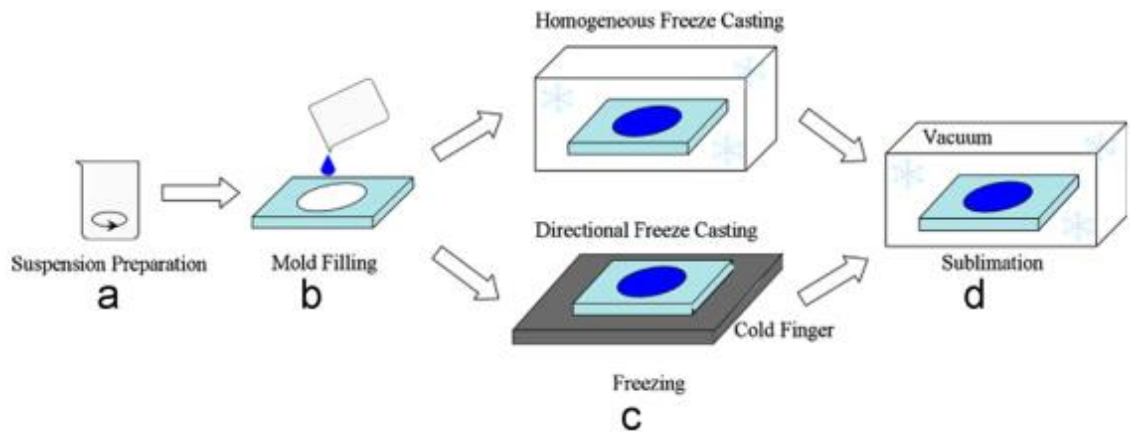


Figure 2.12 Illustration of the freeze casting process. [114]

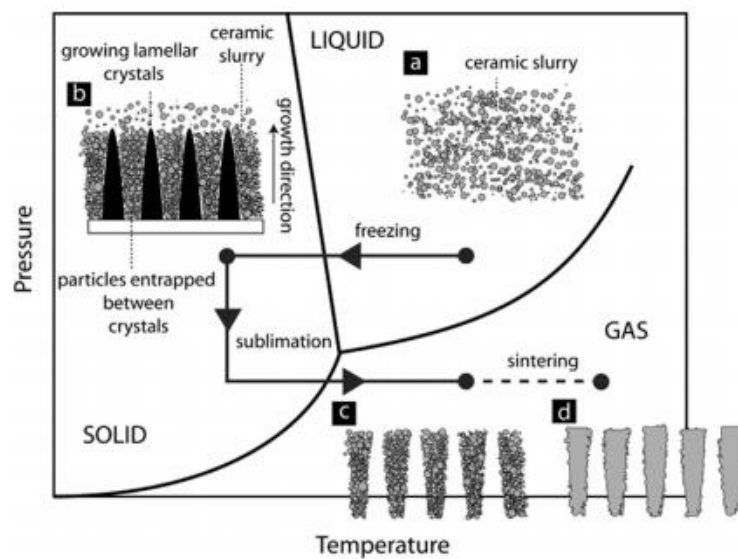


Figure 2.13 The relationship between the aqueous suspension states and the processing steps. [116]

In the directional freeze-casting process, the final microstructure depends on the particles which are expelled and entrapped by the moving solidification front [116]. The theory of freezing cast technique using water as the solvent is shown in Figure 2.14 [117]. When the aqueous suspension is frozen, the ceramic particles are rejected by the growing ice crystals, thus forming a layered structure oriented in the direction parallel to the direction of ice growing. But when the loading of ceramic is high, the moving speed of particles is lower than the rate of ice crystal growing in the highly concentrated suspension, which leads to some particles being entrapped within the ice

crystals. The entrapped ceramic particles form inorganic arms which become the bridge between adjacent walls. Due to this feature, the freezing cast technology can construct a 3D network of ceramic fillers by adjusting the fabrication parameters.

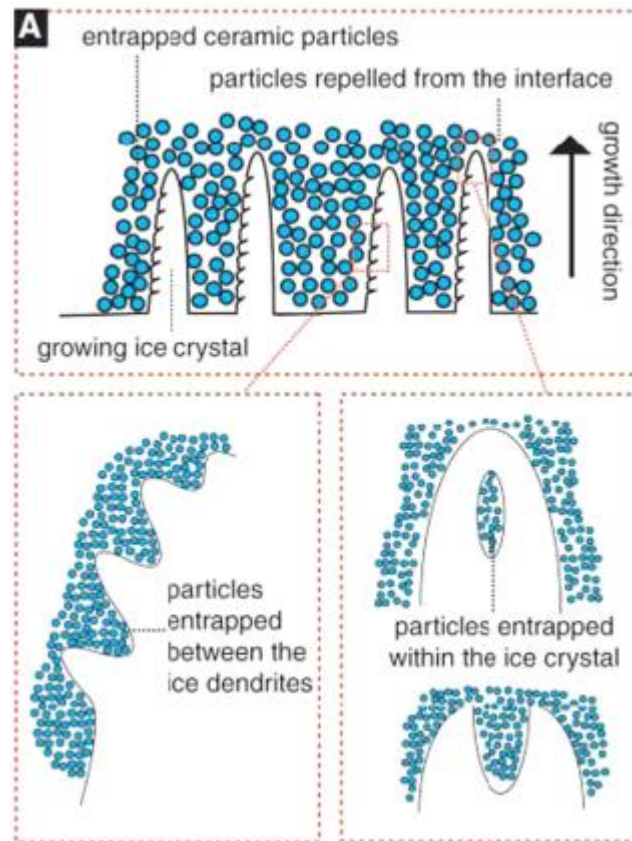


Figure 2.14 Schematic of freeze-casting principle. [117]

Zeng et al. used BNNS as the assembly unit to prepare a 3D structured BNNS with a controllable structure based on the ice-templating method (Figure 2.15) [118]. When the content of BNNS is 9.3 vol%, the through-plane and in-plane thermal conductivity of the composite are 2.85 and $2.40 \text{ W m}^{-1} \text{ K}^{-1}$, respectively. At the same BNNS content, the thermal conductivity of epoxy composite with random distribution BNNS is only $1.13 \text{ W m}^{-1} \text{ K}^{-1}$, which indicates the 3D BNNS network in the composite is beneficial to the formation of thermal conductivity network of composite results in improving the thermal conductivity of the composite.

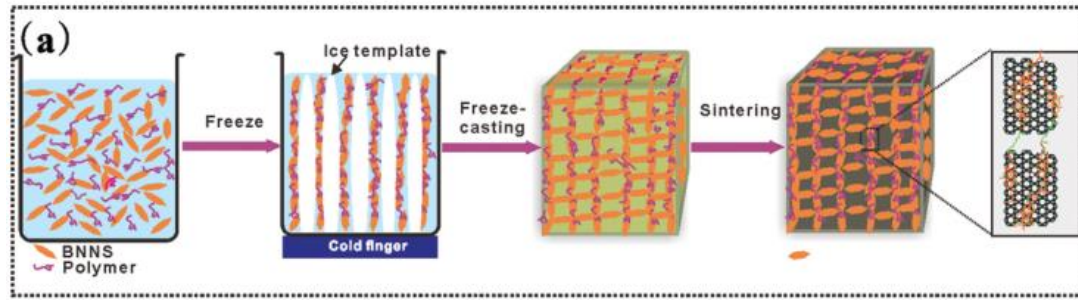


Figure 2.15 An illustration of the fabrication of 3D BNNS network [118].

Salt templating

The salt templating method involves controlling the dispersion of fillers by occupying the spaces created by the salt and maintaining the structural framework through the use of a binder to prepare 3D fillers. As shown in Figure 2.16, Cui et al. [119] fabricated poly (ethylene-co-vinyl acetate) (EVA) connected 3D BN skeleton by using a NaCl template. The h-BN platelets were connected by EVA binder and then epoxy resin was infiltrated into the 3D BN skeleton to prepare composite. A high thermal conductivity of $1.85 \text{ W m}^{-1} \text{ K}^{-1}$ is achieved at a relatively low BN loading of 16.8 vol%.

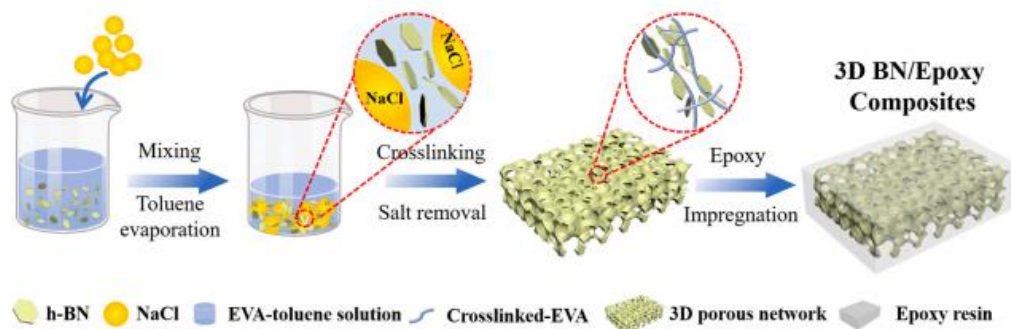


Figure 2.16 Schematic route for the preparation of 3D BN/Epoxy composites by salt templating method [119].

Polymer templating

The polymer templating method is depositing high thermal conductivity fillers on the surface of a 3D polymer to create an interconnected network structure. Qin et al. [120] utilized commercially available melamine-formaldehyde (MF) foam as the scaffold to prepare a 3D interconnected network structure of reduced graphene oxide (rGO). The process is immersing MF foam in a suspension of GO and subsequently removing excess GO from the pores through centrifugation. This procedure lets GO attach to the foam scaffold surface. After the chemical reduction of GO, a 3D interconnected network of rGO was obtained based on the MF scaffold. PDMS precursor was then poured into the 3D rGO foam to prepare a thermally conductive composites (Figure 2.17). By controlling the immersion time of the foam in the GO suspension and compressing the three-dimensional rGO foam from different directions to regulate the orientation and density of the rGO foam in the composites. With a 3D compression ratio of 70% and a rGO loading of approximately 4.82 wt%, the thermal conductivity of the composites reached $2.19 \text{ W m}^{-1} \text{ K}^{-1}$, which is about 12 times higher than that of the uncompressed composites.

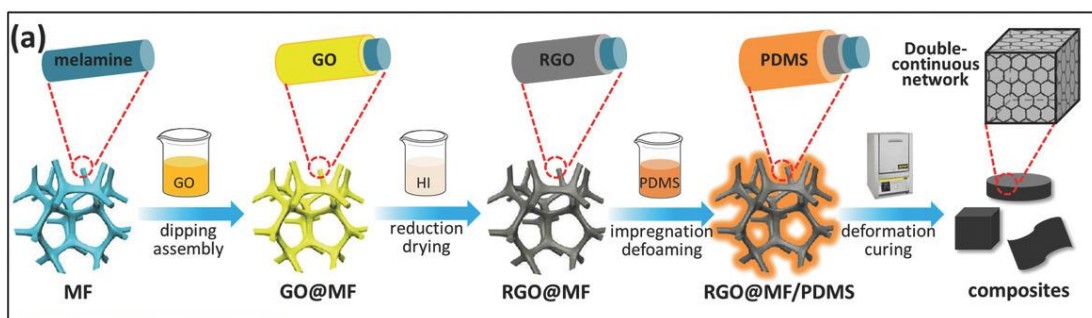


Figure 2.17 Illustration of preparation procedures of the Graphene network and the polymer nano composite [120].

2.5 Effect of fillers on CTE of polymer composites

In addition to low thermal conductivity, the high CTE also restricted applications of polymer in electronic packaging. Table 2.3 shows the CTE values of the most commonly used polymer. Typically, polymers exhibit a CTE within 25-200 ppm K⁻¹, significantly higher than metals and ceramics. The metals and ceramics possess CTE values ranging from a few up to 30 ppm K⁻¹ [121]. As shown in Table 2.4, the CTE values of polymer are much higher than other part of materials in electronic packaging. The CTE of the silicon chip is only 3 ppm K⁻¹, but the CTE of E-glass fibre reinforced epoxy commonly used as PCB is 11-20 ppm K⁻¹ in the X-Y direction, but 60 ppm K⁻¹ in the Z direction [13, 122]. Thermal stresses and warpage in electronic components primarily result from differences in CTEs. Therefore, it is essential to reduce the CTE of polymers.

Table 2.3 CTE values of the most commonly used polymer [123].

Material	CTE value (ppm K⁻¹)
Epoxy resin	45-75
Polypropylene (PP)	200
Polyethylene (PE)	180-200
Polycarbonate (PC)	65
Polyphenylene sulfide (PPS)	50
Polyvinyl chloride (PVC)	70
Polyetheretherketone (PEEK)	25-50
Polytetrafluoroethylene (PTFE)	112-125
Polyvinylidene difluoride (PVDF)	130

Table 2.4 CTE values of materials in electronic packaging. [13]

Material	CTE value (ppm K⁻¹)
E-glass Fibres reinforced Epoxy	11-20 (XY) 60 (Z)
Aluminium	23
Copper	17
Titanium	9.5
Solder-Sn63/Pb37	25
Sintered Ag paste	19.6

The glass transition temperature (T_g) is a critical property of thermoset polymers that denotes a change in mechanical characteristics or the onset of phase alterations. It typically denotes the temperature range where the polymer transitions from a rigid, glass-like state to a more flexible, rubbery state. For example, epoxy resin is a thermoset polymer. Above the glass transition temperature (T_g), thermoset polymers exhibit characteristics of a highly viscous liquid or a ductile solid, while below the T_g , they behave as a hard and brittle solid. All CTE values mentioned in this thesis are below the glass transition temperature. Many studies have found that the thermal expansion and T_g of polymer changed by adding fillers, such as nano-graphite [124], CNTs [125], BN [118], and silica [126]. The addition of graphite nano-platelets (GNPs) to the polymer has been observed to potentially reduce both linear and axial CTE [127]. GNPs effectively decrease the CTE of the composites and also enhances other functionalities such as the electrical conductivity of the composites. Warriar et al. integrated CNTs into the glass fibres epoxy composite, which resulted in a higher glass transition temperature and reduced CTE [125]. These results show the effectiveness of employing nano fillers to minimize residual stress in fibre-reinforced composites. BN filler can also lead to rapid reduction in the CTE at relatively lower

concentrations, primarily due to its high aspect ratios [118]. The reduction in CTE in polymer nanocomposites is attributed to the decrease in segmental motion of polymer chains, which is caused by the hindrance offered by nano fillers.

There are many factors that can influence the CTE of composites, for example, the size, shape, functionalization and the distribution of fillers in the polymer matrix. The single-walled CNTs are functionalized first before being mixed with epoxy resin to investigate the effect on CTE of composites [128]. Incorporating functionalized nanotubes into nanocomposites has been observed to reduce the CTE by up to 52%. However, with the pristine CNT, the reduction of CTE was negligible due to uneven distribution and weak bonding at the interface between CNT and epoxy. The capped CNTs which have smaller sizes lead to a lower CTE of CNT nanocomposites [128]. Ren et al. [129] chose two different shapes of silica (silica nanoparticles and silica nanofibers) to add to epoxy resin. Silica nanofibers filled epoxy exhibited lower CTE than silica nanoparticles filled epoxy, which indicates epoxy filled with high aspect ratio nanofibers demonstrated a notable decrease in the CTE. This occurs because fillers with elevated aspect ratios can impose substantial mechanical limitations on the polymer matrix's deformation, thus disrupting the distribution of thermal stress within the matrix.

Alignments of fillers in polymer matrix also influence the CTE of composites. The well-aligned 3D networks of rGO walls bridged by single wall CNTs (SWCNT) were constructed in epoxy resin [130]. The CTE value of rGO/SWCNT epoxy composite is reduced to 59.47 ppm K⁻¹ for the in-plane direction, which is ~17% decrease as compared to the pure epoxy resin. The reduction in CTE observed in nanocomposites can be ascribed to the 3D networks formed by rGO and SWCNTs. These networks employ a pinch-off mechanism to efficiently impede volume expansion. Because the

CTE of rGO differs between the in-plane (-1 ppm K^{-1}) and through-plane (28 ppm K^{-1}) directions [131], the CTE of rGO/SWCNT nanocomposites also exhibit anisotropy CTE. The anisotropic CTE in the in-plane and through-plane direction was also observed in 3D BNNS networks epoxy composites due to the anisotropic CTE of BNNS (-2.7 ppm K^{-1} in the in-plane direction, 38 ppm K^{-1} in the through-plane direction [132]). In the 3D structure, the alternative layered structure between BNNS and epoxy helps to suppress the volume change of composites. At the BN loading of 9.3 vol%, the CTE values of composites decreased from 69 ppm K^{-1} to 24 and 32 ppm K^{-1} in the through-plane and in-plane directions [118].

2.6 Dielectric properties of polymer composites

Dielectric properties are mainly including two parameters, dielectric constant and dielectric loss, which characterise the ability of a material to save and lose electrostatic energy in an electric field. Excellent dielectric properties are reflected in low dielectric loss.

2.6.1 Dielectric constant and dielectric loss

Dielectric constant is an important characterisation parameter to dielectric materials, which measures the polarization behaviour or the ability to store charge under the action of an electric field [133]. The dielectric constant determined by the material itself, independent of the applied electric field. The greater the polarization of the material, the larger the induced charge, leading to an increased dielectric constant.

Dielectric loss is mainly determined by the internal properties of the material and is defined as the amount of energy consumed per unit volume of dielectric per unit time to convert electrical energy in the form of heat into thermal energy. The measurement of the dielectric loss $\tan\delta$ under an alternating electric field is carried out on a spectrum

analyser, and the loss at a frequency of 1000 Hz is usually taken as the dielectric loss of the samples.

Reasons for dielectric loss can be described as follows: [134] (1) conductivity loss, under an applied electric field, the conductive carriers in the materials will move to form a current, so that part of the electrical energy is converted to overcome the resistance of the thermal energy. Whether it is an alternating electric field or a constant electric field, conductivity loss can not be avoided, but most polymers because of their poor conductivities, their conductivity loss is small. (2) polarization loss, only occurring in the alternating electric field, is the electric field and the materials to produce the result of energy exchange. Polarization is divided into orientation polarization and deformation polarization. Orientation polarization is a dipole in the electric field force under the action of the steering, part of the electric energy used to overcome the viscous resistance of the materials into heat of a relaxation process; deformation polarization arises when the material's intrinsic frequency of vibration matches the frequency of the electric field, this phenomenon was known as resonance absorption. This process, which is elasticity, results in maximal electric field energy loss. Conductivity loss occurs mainly in non-polar polymers, polarization loss occurs mainly in polar polymers.

2.6.2 Mechanism of dielectric properties

The various polarization mechanisms within the dielectric materials are described as follows. (1) Electron displacement polarization: under the external electric field, the electrons outside the nucleus of the atom are displaced, resulting in the separation of positive and negative charges, which is the most common polarization in materials. The establishment time of electron displacement polarization is basically in the optical

frequency range. (2) Ion displacement polarization: the movement of positive and negative ions under electric field force causes the ionic bond to be elongated, thus forming a dipole moment. Compared with the electron polarization, the ion mass is larger, so the polarization establishment time is about $10^{-12}\sim 10^{-13}$ s. (3) Orientation polarization: in a dielectric, disordered dipole moments will be aligned in the direction of the external electric field. This kind of polarization exists only in the polar dielectric, and the dipole can not be restored to its original state after the withdrawal of the electric field. This process will consume a certain amount of energy, and the time period is longer, about $10^{-2}\sim 10^{-10}$ s. (4) Space charge polarization: in non-uniform media, the chaotic distribution of space charge tends to become ordered due to defects, resulting in the production of an electric field. This polarization lasts for a long time, about $10^{-7}\sim 10^6$ s, mainly in the low-frequency role.

2.6.3 The research on thermally conductive dielectric composites

Power electronic devices operating under high electric fields, like energy storage and conversion devices, require dielectric composites characterized by a high dielectric constant and high dielectric breakdown strength [135, 136]. These energy storage devices suffer from high electric field intensity and poor heat dissipation [137, 138]. In this context, dielectric composites with high thermal conductivity are necessary to maintain the reliability of these devices [139, 140]. A thermally conductive insulating film permits the use of elevated voltages while ensuring electrical safety. Polymers often serve as dielectric materials because of their numerous benefits, such as superb breakdown strength, low dielectric loss, outstanding thermal stability, affordability, versatile processing options, and exceptional dependability. These attributes demonstrate considerable promise for use in energy storage and conversion devices

operating at high temperatures [141]. However, polymer dielectric is thermally insulating and has a thermal conductivity below $0.5 \text{ W m}^{-1}\text{K}^{-1}$ [142]. High dielectric constant ceramic fillers are extensively utilized in polymer to fabricate high-performance dielectric composites. However, the heat produced from excessive use or minor electrical discharges can lead to a rise in the temperature of insulation substances, gradually leading to the loss of dielectric performance, thus it is challenging to meet the urgent demands of thermally conductive dielectric materials in high power density electronic device applications. Nanocomposites using high dielectric and high thermally conductive fillers are promising to meet this challenge. However, random filler distribution in this composite is found to be quite challenging to achieve a balance between low dielectric loss and high thermal conductivity. Generally, to achieve the target thermal conductivity, a high loading is required to form continuous heat transfer pathways [143]. But high thermal conductivity composites are generally accompanied by high dielectric loss and dramatically decreased breakdown strength with the filler content [144, 145]. High dielectric losses cause the material to generate a lot of heat during use, which can lead to damage to the electronic. The generated heat could not be dissipated in time due to the low thermal conductivity. Meanwhile, the electric field surrounding high dielectric constant fillers is significantly stronger than that in other parts of the polymer. This heightened local electric field increases the likelihood of breakdown occurring. Enhancing the dielectric constant of composites is crucial without causing a rise in dielectric loss or a reduction in breakdown strength. There are several strategies have been employed to maintain high dielectric constant, low loss and dielectric breakdown strength as high as possible along with enhanced thermal conductivity, such as the alignment of fillers [146], core-shell structures [147], and design of multi-layered structure [148], and so on.

Employing a multilayered structure is a straightforward and efficient approach to achieve this objective. In this setup, a layer with high filler loading offers a high dielectric constant, while a layer with low filler content prevents an increase in leakage current [144]. It is proposed that the variance in filler distribution within these multilayered films can efficiently redistribute electric field intensity, thereby decreasing the internal field strength within the dielectric layer and enhancing the overall breakdown strength of these composites [149]. Studies have indicated that each layer in a multilayer structured film, formed by different filler loading, can leverage its advantages to enhance both the dielectric constant and breakdown strength of the overall composite [149-151].

h-BN platelets are excellent candidates for producing composites with both high thermal conductivity and desirable dielectric properties due to its large band gap (5.7 eV - 6 eV), and high thermal conductivity ($300 \text{ W m}^{-1}\text{K}^{-1}$ for the in-plane direction, and $30 \text{ W m}^{-1}\text{K}^{-1}$ along the through-plane direction) [105, 152, 153]. h-BN platelets are also easier to form horizontal distribution along (002) or (004) plane in polymer matrix. The 2D structure and significant aspect ratio contribute to the improvement of in-plane thermal conductivity [154]. Additionally, SiC whisker exhibits excellent insulating attributes along with a respectable theoretical thermal conductivity, approximately $120 \text{ W m}^{-1}\text{K}^{-1}$ [36, 155]. It is reported that the introduction of one-dimensional SiC whiskers, could filled the gap between the two-dimensional graphene nanosheet to prevent the accumulation, and thus a thermally conductive path is additionally constructed in the longitudinal direction [156]. The path and intensity of dielectric breakdown are greatly influenced by the nanocomposite's microstructure, specifically the size and arrangement of the fillers. Fillers having aspect ratio, $AR > 1$ (whiskers and platelets) should have higher barrier potential at

the interface between matrix and fillers for the carrier to overcome during the conduction process [157]. In the breakdown process, when electrical treeing encounters the filler, it propagates along with the interface between matrix and fillers due to the obstruction in treeing propagation. An increase in encountering frequency using the hybrid fillers (i.e. a mixture of h-BN platelets and SiC fibres) could effectively prevent electrical treeing, resulting in an enhancement in the insulation breakdown strength of the composite [157]. Meanwhile, the addition of SiC and BN can also help to increase the dielectric constant. Thus, SiC whiskers and h-BN platelets are anticipated to additionally enhance the dielectric constant while synergistically boosting in-plane thermal conductivity through the formation of conductive pathways in the in-plane direction.

2.7 Application of thermally conductive composites

Nowadays, the management of heat dissipation is a critical issue that influences safety, performance and durability of electronic devices. Thus, the demand for novel thermal conductive composites is increasing. Over the past few years, thermally conductive and electrically insulating composites gradually played an increasingly important role in the modern electronic industry. In some applications, the heat dissipation materials direct contact with the chip, so the materials need to possess both efficient thermal conductivity and good electrical insulation capabilities. Therefore, this thesis focuses on the application of thermally conducting and electrically insulating composites.

2.7.1 Electronic packaging

As shown in Figure 2.18, the thermal interface material is used as a medium for interface heat transfer between two materials, which can improve the interface heat transfer efficiency [158]. Due to the roughness of the solid surface morphology, at the

micro-nano scale, the solid surface is not smooth. When two solid materials contact each other, only a small percentage of the surface forms an effective physical connection, and the remaining voids at the interface are filled with air. However, the thermal conductivity of air is only $0.024 \text{ W m}^{-1} \text{ K}^{-1}$ which is much lower than that of many materials. Thus, even for substances with low surface roughness, how to improve the effective contact area is also an urgent technical issue to be solved.

In electronic packaging, the thermally conductive and electrically insulating composites are applied for the thermal interface materials (Figure 2.18b), which are placed between the heat-emitting chip and the integrated heat sink to establish an effective heat conduction channel, leading to significantly lower contact thermal resistance [158]. Thermal interface materials (TIMs) can fill the micro-voids and holes on the surface of two materials when they are joined or contacted. In practical applications, although the use of TIMs will add a new interface between the two materials, they still improve the overall thermal conductivity of the system.

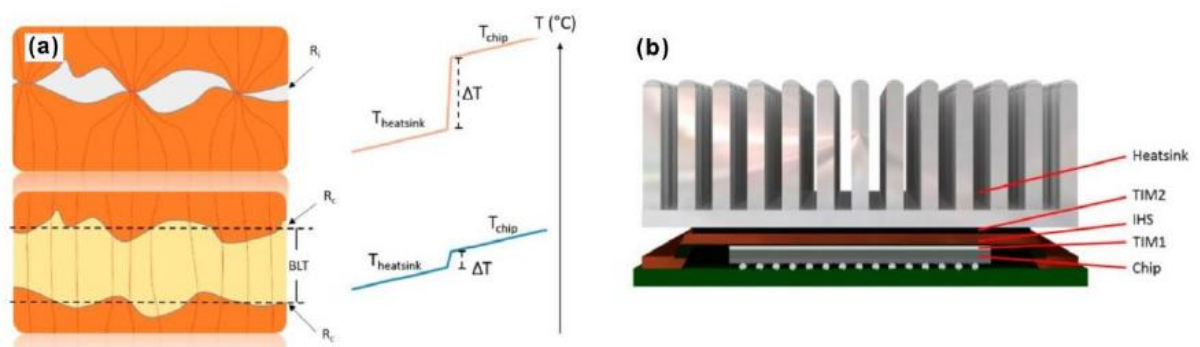


Figure 2.18 (a) Working principle of TIMs; (b) The electronics package with two TIMs. [158]

The substrate material is also an essential part of the electronic packaging system. PCBs are integral components in nearly all Electrical and Electronic Equipment (EEE). They typically constitute 4-7% of the total mass of electric and electronic devices. In

commercial products, this percentage is often higher, reaching up to 20-30% in mobile phones, 20% in computers, and 10% in televisions [159]. The functions of substrates are carrying the electronic components and making circuit connections, insulation, heat conduction and protection of components. Due to the continuous increase in power and integration of electronic devices, the distances between components are shrinking, resulting in an escalating heat dissipation requirement within limited space. If this heat is not promptly and effectively dissipated, it can lead to elevated temperatures of the components, posing a risk of damage to electronic devices. Thus, there is a growing demand for high thermal conductivity substrates to address these thermal management challenges. Thermally conductive composite polymers offer significant advantages in addressing these thermal dissipation issues. Meanwhile, thermally conductive polymer composites possess many advantages, including excellent dielectric properties, lightweight, cost-effectiveness, impact resistance, corrosion resistance, ease of processing, and suitability for large-scale production.

2.7.2 Light-emitting Diode (LED) devices

Globally, lighting electricity consumption accounts for nearly 20% of total electrical energy usage [160]. LED lighting, characterised by high energy efficiency (30%), instant start-up, long lifespan, and low power consumption, has gradually replaced traditional lighting sources such as fluorescent and incandescent lights [160, 161]. With the continuous improvement in lighting performance requirements and the sophisticated development of LEDs, there is a trend towards high power density and high integration. Currently, LED luminous efficacy has reached 220 lm W^{-1} (the initial luminous efficacy was only 0.1 lm W^{-1}) [162]. Simultaneously, the rapid development of LEDs has brought about thermal management challenges because 70% of the energy

in the LED is converted into heat [163]. Such a large amount of heat will seriously affect the working efficiency and stability of the LED. At a constant operating current, for every 10 °C rise in temperature, the luminous efficiency of the LED decreases by 5% and the working life decreases by 50% [8]. If this substantial amount of heat is not dissipated promptly, the temperature of the LED light-emitting chip will sharply rise, significantly affecting LED performance, resulting in decreased reliability, lower luminous efficiency, shortened lifespan, and irreversible damage. Additionally, in LED lighting, heat dissipation is mainly achieved using metal heat sinks, primarily composed of aluminium. However, in environments with conditions such as acidity, alkalinity, high temperature, and high humidity, metal materials often suffer from issues like scaling, corrosion and oxidation. In this situation, thermally conductive polymer composites stand out. They offer significant benefits including being lightweight, easily mouldable and resistant to corrosion.

2.7.3 Solar cells

In recent years, solar energy has garnered widespread attention as a renewable and sustainable energy source. Solar cells, also known as photovoltaic (PV) cells, are devices that convert sunlight directly into electricity through the photovoltaic effect. They are a key component of solar panels and are widely used in renewable energy systems to generate clean and sustainable power. Because solar cells have a relatively low efficiency in converting light to electricity, a large fraction of the solar energy they capture turns into heat within the cells. The photovoltaic conversion efficiency of solar cells decreases with an increase in operating temperature. For every 1 K rise, the output power of crystalline silicon-based cells drops by 0.4% [164, 165], and the efficiency of amorphous silicon cells drops by 0.25% [166]. To ensure the photovoltaic

conversion efficiency of solar cells, how to dissipate the heat generated within the cells becomes a significant challenge.

Figure 2.19 shows a typical solar cell module made by different layers [167]. Poly(ethylene vinyl acetate) (EVA) as a commonly used cell encapsulation material has a very low thermal conductivity ($0.23 \text{ W m}^{-1} \text{ K}^{-1}$). Besides, Polyvinylidene fluoride (PVDF) which is also a commonly typical backsheet component material in solar cells exhibits poor performance with a thermal conductivity of only $0.35 \text{ W m}^{-1} \text{ K}^{-1}$. Jaewon et al. investigated using three different kinds of backsheet materials in the solar cells. The study has shown that backsheet materials with an increased thermal conductivity contributed to decrease in the average cell temperature if more than $1 \text{ }^\circ\text{C}$ in general and of more than $2 \text{ }^\circ\text{C}$ on hot sunny days [168].

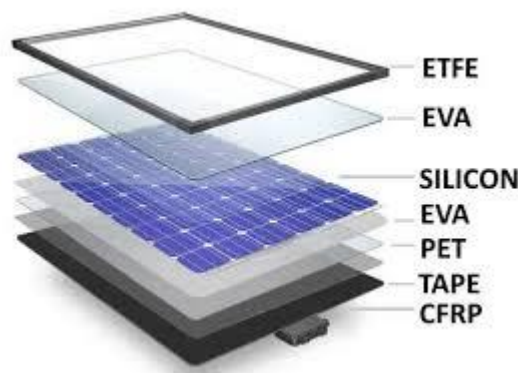


Figure 2.19 A solar cell module made by different layers [167].

Thermally conductive materials are also used as TIM in the solar cells as shown in Figure 2.20. A small percentage of graphene (1-6 wt%) is mixed with a commercial TIM to increase its thermal conductivity [169]. By using graphene-enhanced TIM, the efficiency of solar cells was enhanced by effectively eliminating unwanted heat. This method can recover up to 75% of the power loss [169].

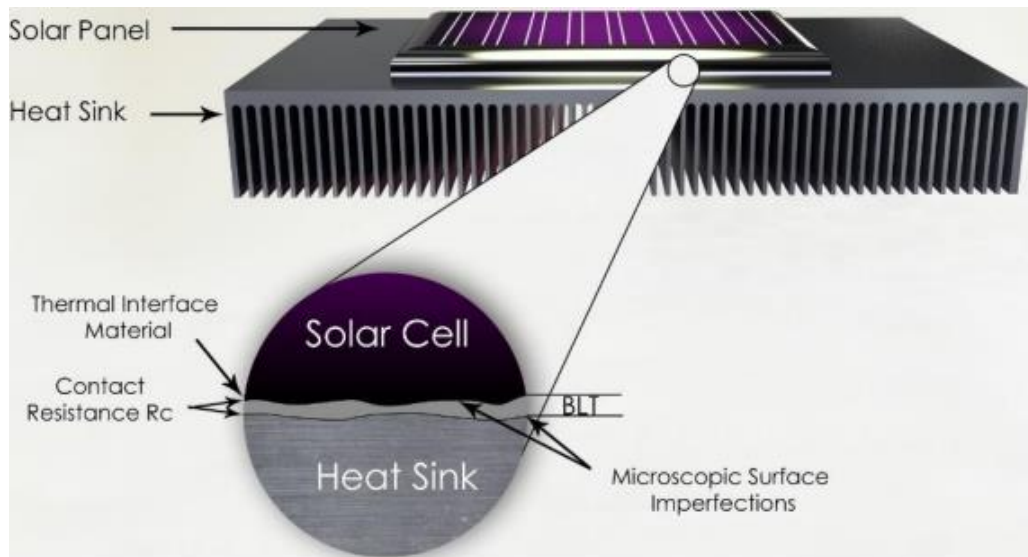


Figure 2.20 Illustration of operation of TIM in solar cell [169].

The polymer layers with low thermal conductivity become the bottleneck in the heat dissipation of photovoltaic cells. The most effective solution to address the heat dissipation issue is the introduction of electrically insulating thermally conductive fillers in the polymer.

2.8 Summary

From previous research, it is known that adding fillers to composites to construct a continuous thermal conduction network is key to enhancing the thermal conductivity of composite materials. The orientation behaviour of 1D and 2D fillers with anisotropic thermal conductivity can form composites with anisotropic thermal conduction properties. The orientation of the fillers can be achieved during the processing or through external fields, such as magnetic fields and electric fields.

Among the various fillers, 1D SiC fibres and 2D h-BN sheets are considered ideal fillers at this stage due to their high thermal conductivity, low expansion coefficient, high dielectric breakdown strength, and excellent oxidation resistance. These

properties make them well-suited for preparing materials with good insulating properties, thermal conductivity, and mechanical performance.

BN, as a 2D filler, has been widely used in past research. However, due to its sheet-like shape, BN tends to form thermal conduction pathways more easily in the horizontal direction, thereby increasing thermal conductivity horizontally. The freeze-drying and electromagnetic orientation methods can achieve vertical alignment of BN sheets, but both methods involve relatively complex preparation processes and require precise control over both the preparation and synthesis processes to achieve precise structural design. Therefore, there is an urgent need to find simpler methods for vertically aligning BN sheets. Compared to 2D fillers, 1D fillers with a high aspect ratio are expected to form long heat-conductive pathways along their longitudinal direction within the composites. However, these promising structures have been less explored in previous studies on thermally conductive composites.

In previous studies, SiC nanofibers were also added as fillers into epoxy resin, achieving a thermal conductivity of $1.67 \text{ W m}^{-1} \text{ K}^{-1}$ [59]. This is almost the highest thermal conductivity that SiC resin-based materials can achieve with a filler loading of less than 20%. However, SiC nanofibers are very expensive, which is not conducive to subsequent large-scale applications. Further research is needed to design and construct thermal conduction pathways using more affordable micron sized SiC fillers.

Although researchers have conducted extensive scientific studies on highly thermally conductive polymer-based materials, and these materials have seen initial applications, there are still significant challenges as follow.

- 1) The thermal conductivity of epoxy resin is very low; therefore, when the thermally conductive filler content is below 50%, the thermal conductivity of

composites with the epoxy resin matrix remains around $2 \text{ W m}^{-1} \text{ K}^{-1}$ [8, 12, 45, 170]. Therefore, the thermal conductivity of resin-based composites still needs to be improved.

- 2) Constructing 3D network structures using 1D materials to achieve highly thermally conductive composites has been less explored in previous studies.
- 3) The process for aligning BN vertically is complicated. It is necessary to explore simpler methods to vertically align BN in polymer composites for improving through-plane thermal conductivity.
- 4) The effect of the addition and alignment of 1D and 2D fillers on the CTE of composites also needs to be investigated.

Chapter 3 Methodologies

3.1 Raw materials and chemicals

SiC whiskers (SiCWs, diameter: $\sim 1.5 \mu\text{m}$, length: 5-55 μm) with a purity of 99% were purchased from Alfa Aesar by Thermo Fisher Scientific. h-BN platelets, averaging $\sim 5 \mu\text{m}$ and 70 nm in diameter, were acquired from M.K. IMPEX CORP. Analytical grade (99.99%) isopropyl alcohol (IPA) was purchased from Fisher Scientific. Graphene oxide dispersion (1%, Aqueous) was bought from William Blythe Ltd. Polyvinyl alcohol (PVA) was bought from Sigma-Aldrich Co., Ltd. The epoxy resin (WEST SYSTEM 105) and hardener (WEST SYSTEM 206) were obtained from Gougeon Brothers, Inc.

3.2 Preparation of 3D SiCW network aerogels (3D SiCW) and 3D SiCW-epoxy composites

3.2.1 Preparation of 3D SiCW network aerogels (3D SiCW)

Firstly, PVA was dissolved in water, and then different weights of SiCWs were added into the PVA solution under magnetic stirring for 1 h, followed by sonication for 30 min. Then the slurry was transferred into the polytetrafluoroethylene (PTFE) mould placed on a copper disk that was dipped in liquid nitrogen for 1 h, and this process is called unidirectional freeze casting. For the homogeneous freeze casting, the slurry was transferred into the PTFE mould with a PTFE bottom and also placed in liquid nitrogen for 1 h. Then all the samples are placed in the freeze dryer (Labconco). After freeze-drying at a low temperature ($-55 \text{ }^\circ\text{C}$) and low pressure (0.018 mbar) for 48 h, the frozen scaffolds (SiCW+PVA) were sintered at different temperatures (900/1000/1100/1200 $^\circ\text{C}$) for 6 h in the air to obtain ordered 3D SiC network aerogels.

The networks were controlled by adjusting the loading of added SiCWs (Table 3.1) and these aerogels prepared by the unidirectional freeze casting method were designated as 3D SiCW-X, in which X was the volume fraction of SiCWs in the composites. The SiCW aerogels prepared by homogeneous freeze casting were named Homo-freeze-SiCW. The networks of aerogels with different PVA contents were controlled by adjusting the addition of PVA in suspension and designated as SiCW-PVA-Y. The value of Y is the mass fraction of PVA in the suspension.

Table 3.1 The weight (W_{SiC} , W_{PVA}) and volume (V_{H_2O}) used to prepare SiCW aerogels with different SiC loadings; $R_{SiC/PVA}$ is weight ratio of SiC and PVA; SiC wt% and PVA wt% are the weight percentage of SiC and PVA in slurry.

Group	Aerogel	$W_{SiC}(g)$	$W_{PVA}(g)$	$V_{H_2O}(ml)$	$R_{SiC/PVA}$	SiC wt%	PVA wt%
A	SiCW-2.5	0.5	0.05	10	10:1	4.7%	0.47%
B	SiCW-3.6	0.8	0.05	10	16:1	7.4%	0.46%
C	SiCW-4.6	1.1	0.05	10	22:1	9.9%	0.45%
D	SiCW-5.7	1.4	0.05	10	28:1	12.2%	0.44%
E	SiCW-6.7	1.7	0.05	10	34:1	14.5%	0.42%
F	SiCW-8.2	2.0	0.05	10	40:1	16.6%	0.41%
G	SiCW-10.2	3.0	0.05	10	60:1	23.0%	0.38%

3.2.2 Preparation of 3D networks SiCW-epoxy Composites (3D

SiCW-epoxy)

The composites were prepared by vacuum infiltration of epoxy resin into 3D SiCW aerogels. First, the hardener and epoxy resin were uniformly mixed in a 1:5 mass ratio by manual stirring at room temperature. Subsequently, the as-prepared SiCW aerogels were completely immersed into the epoxy resin mixture and then moved to a vacuum

oven for 30 minutes to expel any air. Due to capillary force and a low-pressure environment, the liquid epoxy resin mixture effectively impregnated the 3D SiCW aerogels. After that, the mixture was cured at 90 °C for 30 min. Finally, the extra epoxy resin matrix adhering to the composite surface was removed by grinding using sandpaper (400 and 1200 grits). The obtained composites were denoted as 3D SiCW-epoxy-X, where X is the volume fraction of SiCWs in epoxy resin composites. For comparison, SiCW composites with randomly distributed SiCWs at the same loading were also prepared by uniformly mixing loose SiCW into epoxy resin using a Speed mixer at 2000 rpm min⁻¹ for 5 min. The SiCWs composites with randomly distributed SiCWs were named as R-SiCW-epoxy-Z, where Z is the volume fraction of SiCWs in epoxy resin composites. The SiCW composites prepared by homogeneous freeze casting were named as Homo-freeze-SiCW-epoxy. The whole preparation process is shown in Figure 3.1.

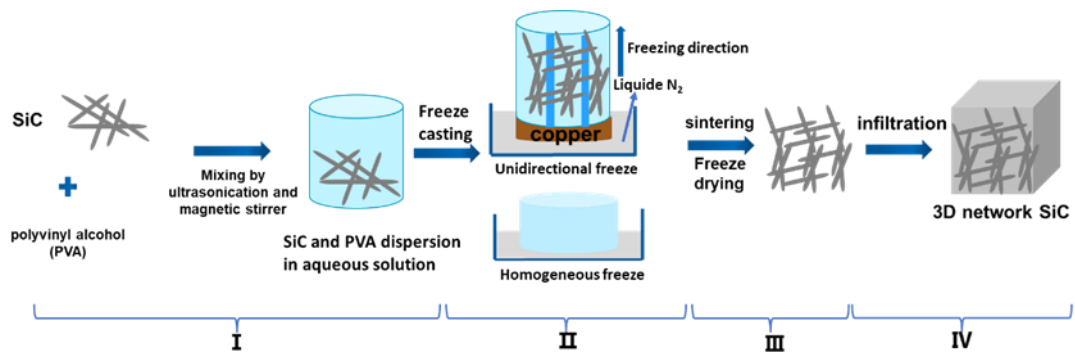


Figure 3.1 Schematic of the fabrication of 3D SiCW-epoxy. The experimental process consists of four steps: (I) preparation of an aqueous slurry containing SiC and PVA; (II) freezing the slurry in liquid nitrogen; (III) freeze-drying and sintering the aerogels; (IV) polymer infiltration.

3.3 Fabrication of BN/SiC bi-layered epoxy resin composites

First h-BN (0.4 g) and IPA (50 ml) were put into a 100 ml beaker, and then the suspension was stirred by magnetic stirrers for 30 min, followed by sonication for 20 min to disperse the h-BN uniformly. Then 0.2 g SiC whiskers were also added to IPA (50 ml) in another beaker. The SiC suspension was also stirred by magnetic stirrers for 30 min, followed by sonication for 20 min. The BN/SiC bilayer was prepared by a sequential vacuum filtration process. The h-BN suspension was filtered first through a vacuum system equipped with a polycarbonate filter paper (47 mm in diameter, 5.0 μm in pore size). A flat BN layer formed on the filter paper as soon as the IPA was completely filtered out. Immediately after that, SiC suspension was poured onto the BN layer for filtration to obtain a SiC layer on top of BN. The obtained BN/SiC bilayer was peeled from the filter papers and dried at room temperature for 12 h. Then, the Epoxy/BN/SiC bi-layered composites were fabricated by vacuum-assisted impregnation of epoxy. Before the impregnation, two-part epoxy resin was uniformly mixed in a 1:5 mass ratio by manual stirring at room temperature. The BN/SiC bilayer was then immersed into the epoxy with the assistance of a vacuum for 30 minutes. Finally, the samples were cured in an oven at 90 °C for 30 min. The whole process and the amount of materials used in experiments are shown in Figure 3.2 and Table 3.2. The randomly mixed BN/SiC epoxy composite (EBNSiC_R) was also prepared for comparison. The same loading of BN and SiC were added into epoxy resin and mixed randomly by magnetic stirring and finally, the mixture was poured into a mould, and waiting for cured at room temperature. The single layer BN and the single layer SiC epoxy composites (EBN and ESiC) with same filler loading were also prepared by vacuum-assisted filtration first and followed by epoxy resin impregnation.

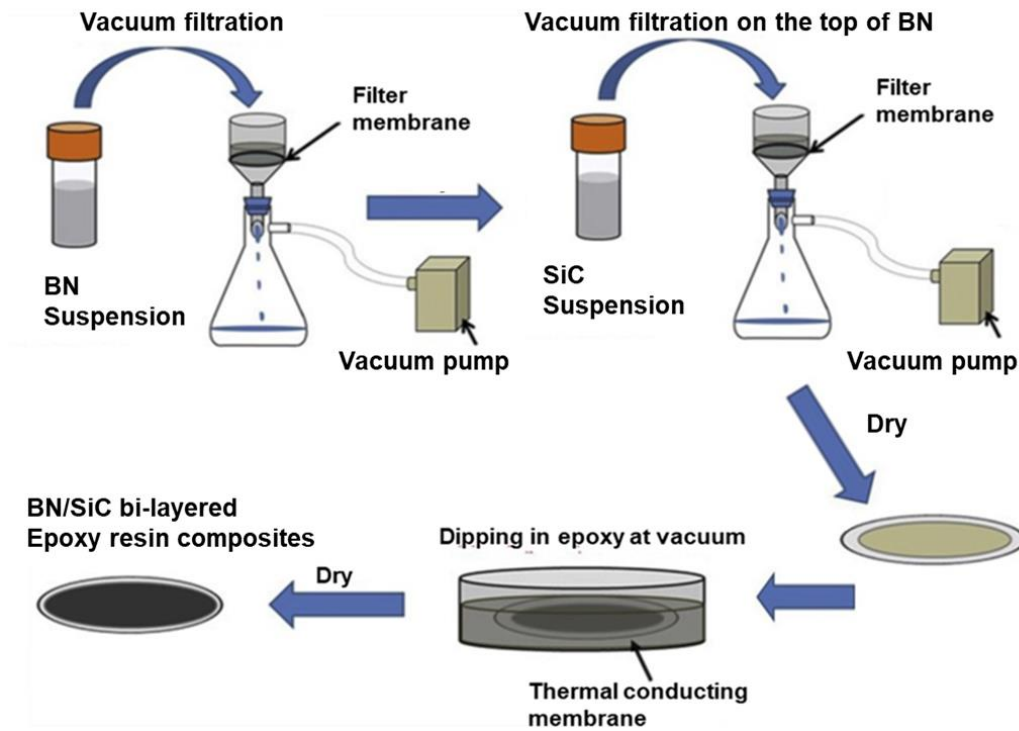


Figure 3.2 Schematic for fabricating BN/SiC bi-layered epoxy resin composite by sequential vacuum-assisted filtration.

Table 3.2 The details of materials used in the experiment. W_{BN} is the weight of BN; W_{SiC} is the weight of SiC; V_{IPA} is the volume of IPA.

Sample name	W_{BN}/g	W_{SiC}/g	V_{IPA}/ml
EBN	0.54	0	50
ESiC	0	0.76	50
EBNSiC_R	0.40	0.20	50
EBNSiC_2L	0.40	0.20	50

3.4 Constructing vertically aligned Boron Nitride-Graphene Oxide (BN-GO) epoxy composites by vacuum-assisted filtration method

Firstly, h-BN (0.5 μm) and GO (4 g together) were mixed with 100 ml deionised water in the beaker and then magnetically stirred and sonicated for 30 min and 20 min to form a homogeneously dispersed suspension. The mass of GO as a percentage of the total mass of BN and GO was 1wt%, 3wt%, 5wt% and 7wt%, respectively. With vacuum-assisted filtration, the homogeneous BN-GO suspension was assembled into a BN-GO “cake” with a diameter of 4.5 cm and height of 2 cm. The pure BN “cake” was also prepared by the same process. 4 g h-BN (0.5 μm) were dispersed with 100 ml Methylated spirit solution by sonication for 30 mins, followed by vacuum-assisted filtration. Then, these “cakes” were longitudinally sliced into sections. These slices were flipped 90° and spread out on the desk to be dried for 24 hours. The epoxy resin parts A and B were mixed in a ratio of 5:1 by manual stirring. Afterwards, the obtained slices were put into the mould, and the epoxy resin was infiltrated into the slices with the help of a vacuum for 15 min. Finally, the samples were cured in a vacuum oven at 90 °C for 10 min. The obtained BN-GO slices were named BN-GOX (X is the weight percentage of GO in the BN-GO cake). The obtained composites were named BN-GOX-epoxy. Table 3.3 shows the details of the materials used in each sample. To further try to improve the thermal conductivity of composites, nano BN (70 nm) was added to epoxy resin before infiltrating into the BN-GO5. The epoxy resin and nano BN were mixed by Speed mixer with 2000 rpm min⁻¹ for 5 min. The proportions of BN nanoparticles in the epoxy resin are 5 wt% and 10 wt% respectively. The obtained

composites were ground with sandpapers (400 and 1200 grits). The whole process is illustrated in Figure 3.3.

Table 3.3 The details of materials used in the experiment. W_{BN} is the weight of $0.5 \mu\text{m}$ BN; W_{GO} is the weight of GO; W_{BN70} is the weight of 70 nm BN nanoparticles.

Name	W_{BN}/g	W_{GO}/g	W_{BN70}/g
BN	4	0	0
BN-GO1	3.96	0.04	0
BN-GO3	3.88	0.12	0
BN-GO5	3.80	0.20	0
BN-GO7	3.72	0.28	0
BN-GO5-70-5wt%	3.80	0.20	0.18
BN-GO5-70-10wt%	3.80	0.20	0.36

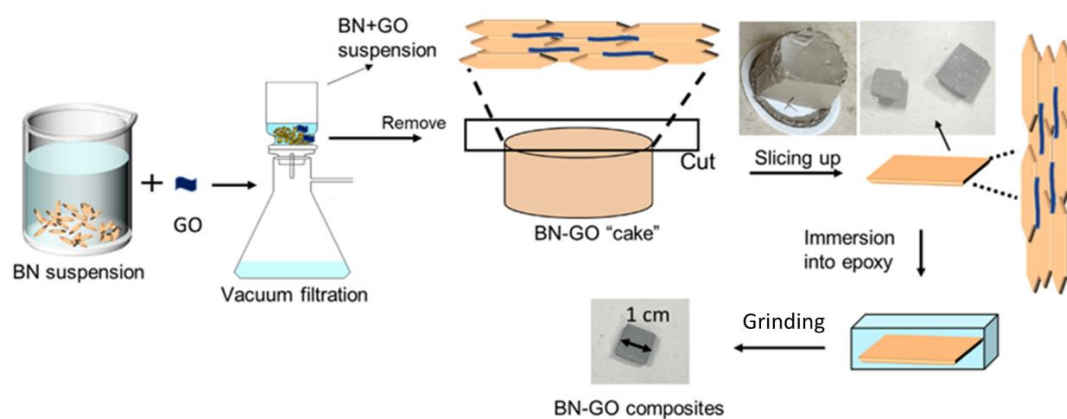


Figure 3.3 Schematic of preparing vertically aligned BN-GO composites by vacuum-assisted filtration.

3.5 Microstructural Characterisation Methods

3.5.1 Scanning Electron Microscopy (SEM)

SEM produces images of samples' morphology by scanning the surface with a focused beam of electrons. Figure 3.4 shows the SEM operating principle. The focused electron

beam interacts with the sample to generate secondary electron emission (and other signals). The secondary electron emission varies depending on the surface morphology of the samples. The detector collects and converts the secondary electron signal into an electrical signal, which is subsequently amplified and displayed on high-resolution monitor. Finally, the secondary electronic image reflecting the surface morphology of the sample is obtained.

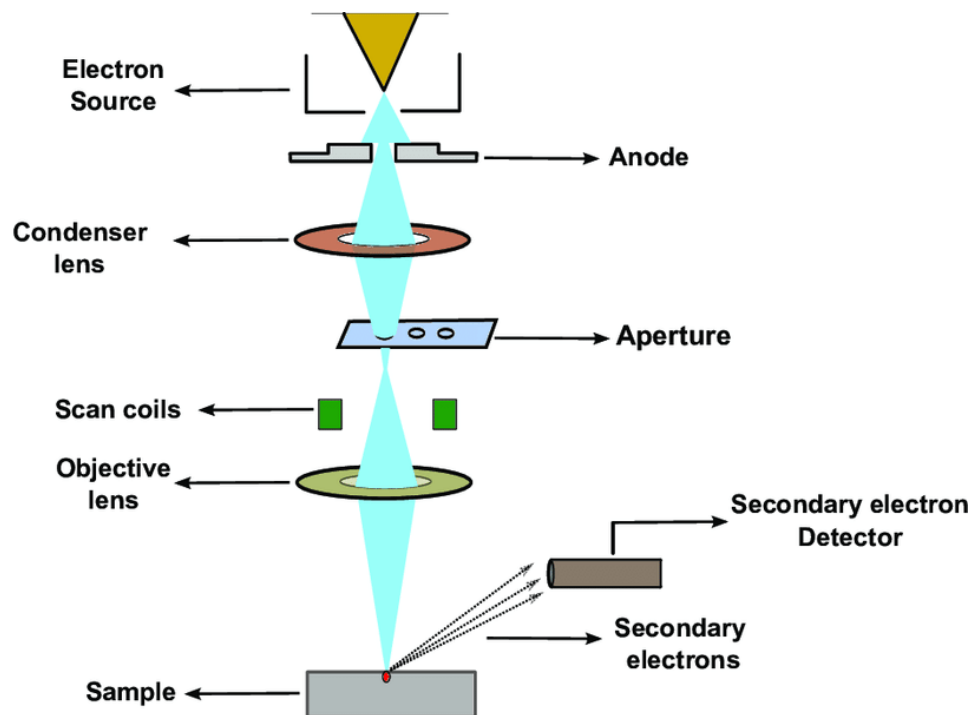


Figure 3.4 SEM probe model and operating principle.[171]

In this thesis, A JEOL 7100F field emission gun scanning electron microscope (FEG-SEM) system with an accelerating voltage of 15 kV and a working distance of 10 mm was applied to examine the microstructure of the samples. The powder samples were attached to a conductive tape. The polymer composite samples were attached to the sample holders with carbon cement for observation. All samples were coated with 10 nm Iridium using a sputtering device.

3.5.2 Focused Ion Beam Scanning Electron Microscopy (FIB-SEM)

Focused Ion Beam Scanning Electron Microscopy (FIB-SEM) is a powerful imaging technique that combines two microscopy methods: Focused Ion Beam (FIB) and Scanning Electron Microscopy (SEM). Figure 3.5a shows the schematic image of the FIB-SEM system [172].

In FIB-SEM, a focused beam of ions (typically gallium ions) is used to cut away layers of a sample, allowing for precise cross-sectional imaging and 3D reconstruction. This cutting process can be controlled with high precision, enabling researchers to precisely expose specific regions of interest within the sample. By combining FIB and SEM imaging capabilities, FIB-SEM allows for the characterisation of complex structures and materials at high resolution, making it a valuable tool in various fields such as materials science, biology, geology, and nanotechnology.

In this thesis, The FEI Quanta200 3D Dual Beam FIB-SEM was used to prepare samples for the transmission electron microscope (TEM). First, the powder sample was stuck on the SEM sample holder and then the needle picked up one SiC fibre and put this fibre on the holder to be used in TEM analysis (Figure 3.5b and c).

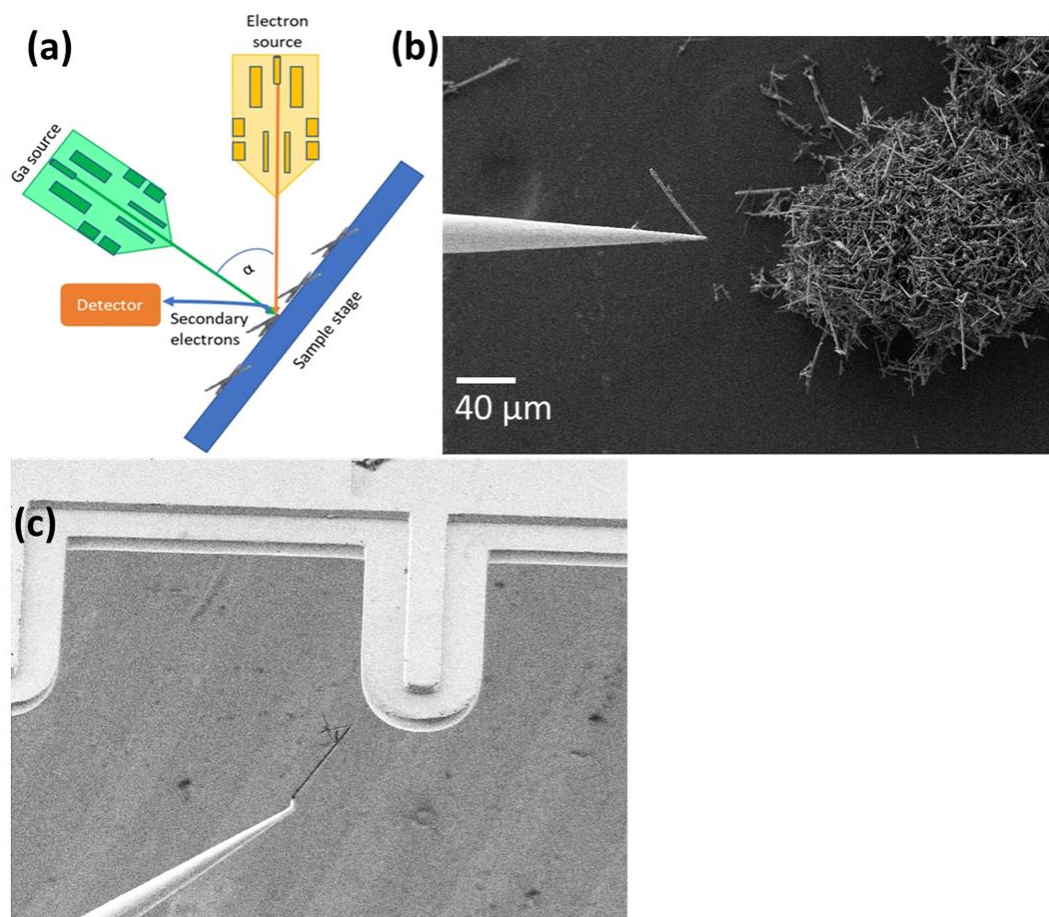


Figure 3.5 (a) Schematic image of FIB-SEM system [172]; (b) the images of picking one fibre by a needle; (c) the images of putting the fibre on the holder.

3.5.3 Transmission Electron Microscope (TEM)

Transmission Electron Microscopy (TEM) is a powerful microscopy technique used to study the internal structure and morphology of materials at the nanoscale. The basic working principle of TEM is shown in Figure 3.6. In TEM, a beam of electrons is accelerated through high voltage (typically 200 kV) and transmitted through an ultrathin specimen, interacting with the sample to generate a high-resolution image. In some cases, the samples must be carefully prepared using polishing and etching to be thin enough. This technique provides detailed information about the atomic structure, crystallography, and defects within materials, allowing researchers to observe features with dimensions as small as a nanometre. TEM is widely used in various fields such

as materials science, nanotechnology, biology, and semiconductor research for characterizing nanomaterials and investigating their properties at the atomic level. Selected Area Electron Diffraction (SAED) is a technique used in TEM to study the crystal structure of materials. By focusing an electron beam on a small, selected area of a thin sample, a diffraction pattern is produced. This pattern consists of spots or rings that provide information about the sample's crystal structure, including lattice parameters, orientation, and symmetry. SAED is particularly useful for identifying phases, studying crystal defects, and analysing nanomaterials.

In this thesis, the transmission electron microscope (TEM, JEOL 2100+) technology with a working voltage of 200 kV was used to obtain the images of samples. SiC samples were cut by FIB-SEM before being imaged by TEM.

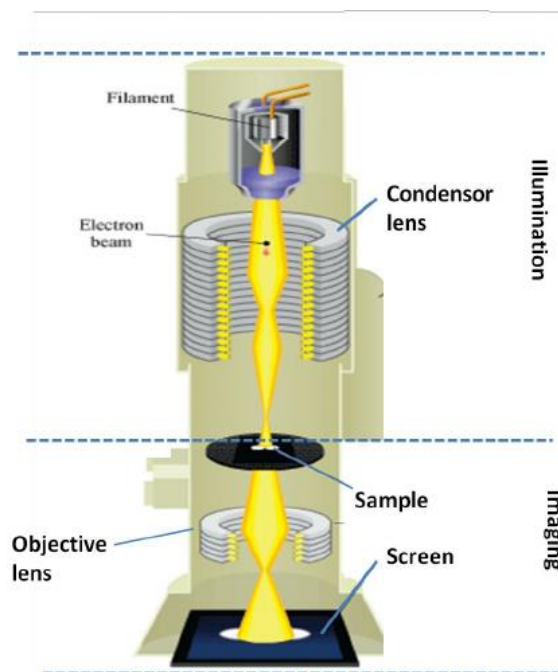


Figure 3.6 Schematic diagram of TEM system [173].

3.5.4 Energy Dispersive Spectroscopy (EDS)

Energy Dispersive Spectroscopy (EDS) is a powerful analytical technique used primarily within the field of material science and engineering for characterizing materials. EDS works by bombarding a sample with a focused beam of electrons to induce the emission of characteristic X-rays from the sample's constituent elements [174]. These X-rays are then detected and analysed to determine the elemental composition of the sample. EDS can be integrated with SEM and TEM, which makes it an invaluable tool for identifying the composition of nano particles and thin films [175]. Both SEM-EDS and TEM-EDS were used in this thesis.

3.5.5 X-ray Diffraction (XRD)

XRD (X-ray Diffraction) is a widely used method of characterising the crystal structure of materials and their changing patterns. The basic principle of X-ray diffraction is shown in Figure 3.7. X-ray diffraction operates on the principle of constructive interference between monochromatic X-rays and a crystalline structure. When a monochromatic X-ray beam strikes a crystal, the spacing between atoms arranged in a regular pattern closely matches the wavelength of the incoming X-ray. This causes the X-rays scattered by various atoms to interfere with one another, leading to pronounced X-ray diffraction at specific angles. This implies that when the incident rays interact with the sample, they produce constructive interference (resulting in a diffracted ray) under conditions that meet Bragg's Law, which is defined as $n\lambda = 2d \sin \theta$. The orientation and intensity of diffracted rays in space are intricately linked to the structure of the crystal. These diffraction patterns serve as a reflection of the law governing atomic distribution within the crystal, revealing both the position and intensity of diffraction peaks through the X-ray diffraction pattern. By comparing with

the standard card, the composition, structure, crystallinity and particle size of the material can be obtained. The texture coefficient (Tc) is used to describe the degree of preferred orientation of crystallites. The intensity of the crystallographic planes in the XRD pattern of sample is used to calculate Tc by following the Harris Equation 3.1.

$$T_c(h_i k_i l_i) = \frac{I_m(h_i k_i l_i)}{I_0(h_i k_i l_i)} \left[\frac{1}{n} \sum_{i=1}^n \left(\frac{I_m(h_i k_i l_i)}{I_0(h_i k_i l_i)} \right) \right]^{-1} \quad \text{Equation 3.1}$$

where I_m is the measured diffraction intensity, I_0 is the diffraction database intensity value, and n is the number of peaks being calculated, in this case $n = 3$, $(h k l)$ is Miller index.

In this thesis, the XRD analysis was carried out by Bruker a D8 Advance system with 40 kV and 35 mA working conditions using Cu $K\alpha$ radiation and the wavelength (λ) is 0.154 nm. The samples were measured with the range of 10-90° at a scanning step of 0.02°, with 0.12 s time step at room temperature. The EVA software is used to analyse the XRD data.

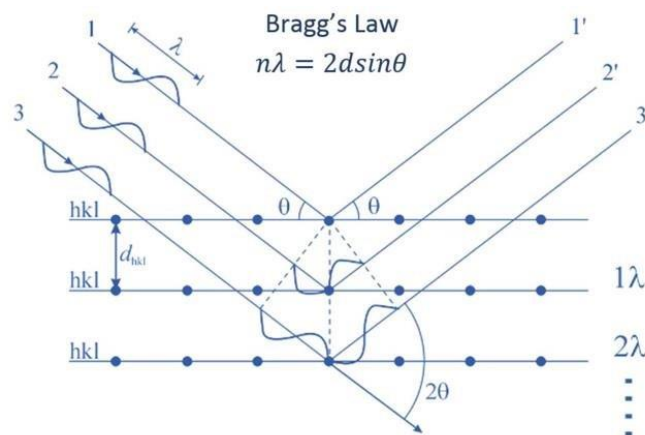


Figure 3.7 Principle of X-ray diffraction.[176]

3.5.6 Density measurement

In this thesis, the density of the samples was measured and calculated following the Archimedes principle. According to Archimedes principle, an object submerged in a fluid is subject to an upward buoyant force that matches the weight of the fluid the object displaces. First, the object is immersed into water, as shown in Figure 3.8. Since the object maintains a state of static equilibrium, the force exerted on it can be depicted by the following below.

$$W_a + F - W = 0 \quad \text{Equation 3.2}$$

where W_a is the tension in the string (the apparent weight of the object), and W is the weight of the object. The buoyant force F is described by the following.

$$F = \rho(\text{water})Vg \quad \text{Equation 3.3}$$

where V is the volume of the object, $\rho(\text{water})$ is the density of water, and g is the acceleration of gravity. Using Equations 3.2 and 3.3 can get the density of the object ρ as following.

$$\rho = \frac{m}{m-m_a} \rho(\text{water}) \quad \text{Equation 3.4}$$

where m is the mass of the object, and m_a is its apparent mass, $m_a=W_a/g$.

In this thesis, the weight of the sample was first measured in the air and then in the water. Because the density of water is 1 g cm^3 , all the densities of samples were calculated by Equation 3.4. Distilled water and an analytical balance with an accuracy

of 0.0001 mg were used. The weight measurements in air and water were repeated three times to avoid errors.

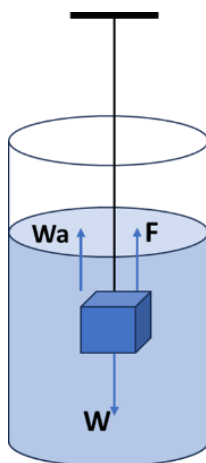


Figure 3.8 Archimedes Principle.

3.6 Evaluation of mechanical properties

The compressive strength of a material refers to the maximum stress it can withstand under a compressive load applied perpendicular to its surface. It is typically expressed as the ratio of force to unit area, measured in Pascals (Pa) or Megapascals (MPa). Compressive strength reflects the material's resistance to compression or squeezing and indicates its ability to withstand external pressure. For elastic samples like aerogels, the compressive stress-strain curves show linear elasticity, plateau and densification regimes. The linear elasticity regime corresponds to the elastic bending of the cell walls of aerogels; the plateau corresponds to the elastic buckling of the cell walls; and the densification regime corresponds to densification of the aerogels. For brittle samples, the samples will break under compression, resulting in a sudden stress drop in the compressive stress-strain curve. In this thesis, an instrument Instron-5969 was used to investigate the compressive behaviour of SiC aerogels and BN-GO slices. For testing SiC aerogels, a 100 N load cell was used, and for testing BN-GO slices, a 500

N load cell was used. The cylindrical SiC aerogels (diameter of 27 mm and height of 4 mm) and BN-GO slices (1 mm×1 mm×2 mm) were compressed at a speed rate of 0.5 mm min⁻¹.

3.7 Evaluation of Thermal Performance

3.7.1 Thermal diffusivity test

Thermal diffusivity represents the speed at which a material conducts heat. A higher thermal diffusivity indicates that heat can spread more quickly through the material. In this thesis, the thermal diffusivities of the composite samples were measured using the LFA 467 HyperFlash laser apparatus (NETZSCH, Germany). As shown in Figure 3.9, one side of a plane-parallel sample is heated by a laser pulse. Then, the temperature rise on the rear surface is measured versus time using an IR detector. According to the mathematical model of the unsteady heat conduction process, the thermal diffusivity of the sample can be determined. By using different holders, LFA can achieve testing through-plane and in-plane thermal diffusivity. The diameter of the samples for the through-plane thermal diffusivity test is 12.7 mm. The diameter of samples for the in-plane thermal diffusivity test is 25.4 mm, and the thickness is below 1 mm. Before the measurement, the samples were spray-coated with a thin layer of graphite on both sides to increase the absorption ratio of light energy and the infrared emissivity of the surface. The thermal diffusivity tests for all composite samples were repeated three times to avoid errors.

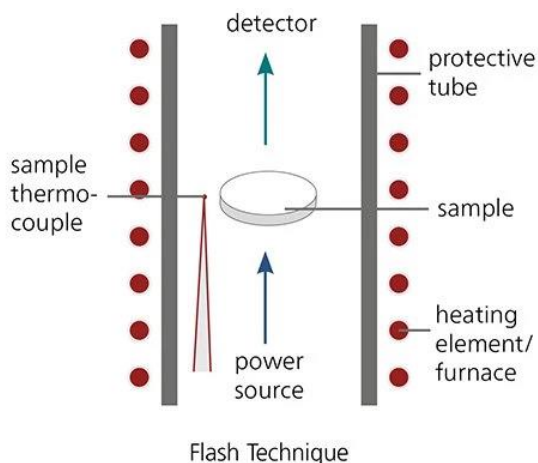


Figure 3.9 Schematic of the measurement of the thermal diffusivity. [177]

3.7.2 Differential Scanning Calorimetry (DSC) and Modulated DSC (MDSC)

DSC is a thermal analysis technique used to test the heat flow change in a sample as a function of temperature or time. It is commonly used to characterise the thermal properties of materials, including melting point, T_g , crystallization temperature, and heat capacity. However, standard DSC still has some limitations, e.g. DSC can only measure the sum or average of the changes in heat flow during heating or cooling, resulting in unclear attribution of absorptive or exothermic peaks, or masking of some characteristic peaks.

MDSC is an advanced variation of DSC that applies a small modulation to the heating rate during the analysis. By superimposing a small oscillation on the heating rate, MDSC separates the reversing and non-reversing heat flow components of the sample. The heat flow signal contains all the information on thermal transformations as in a standard DSC. Reversible heat flow contains information on glass transition, melting, etc. Irreversible heat flow contains information on kinetic phenomena such as solidification, volatilisation, decomposition, etc. This separation allows for a more

detailed analysis of the sample's thermal behaviour, particularly in complex systems or when overlapping thermal events occur. MDSC is particularly useful for studying phase transitions, glass transitions, and thermal stability in materials.

In this thesis, the samples were measured by TA DSC2500. MDSC was used to get the specific heat capacity of composites. The samples were cut to small size first which had an average mass of about 10 mg. The tests were carried out under an N₂ atmosphere from room temperature to 200 °C with a ramping rate of 3 °C min⁻¹.

3.7.3 Thermal conductivity

Thermal conductivity is a fundamental property of materials that describes their ability to conduct heat. It quantifies how efficiently a material can transfer heat through it by conduction. The thermal conductivity (K , W m⁻¹ K⁻¹) is calculated by

$$K = \lambda \cdot \rho \cdot C_p \quad \text{Equation 3.5}$$

where λ (mm² S⁻¹) is the thermal diffusivity and ρ (g cm⁻³) is the density of the samples; C_p is the specific heat capacity.

In this thesis, before testing the thermal diffusivity, the density of samples was measured by the method described in section 3.5.6. For through-plane thermal conductivity test, the samples were cut and ground to 12.7 mm diameter and 1.5 mm thickness. For in-plane thermal conductivity test, the samples were cut and ground to 25.4 mm diameter and 1 mm thickness. The samples were spray-coated with a thin layer of graphite. Then, the samples were put into the specific holder for using in LFA 467 to get the thermal diffusivity. After testing thermal diffusivity, the samples were cut into small pieces with a weight of only about 10 mg. Then the specific heat capacity was obtained by the method described in section 3.7.2. After getting density, thermal

diffusivity and specific heat capacity, the thermal conductivity of samples was calculated by Equation 3.5.

3.7.4 The coefficient of thermal expansion (CTE)

The CTE is a measure of how much a material expands or contracts in response to changes in temperature. CTE can be defined as the fractional increase in length per unit rise in temperature. The obtained CTE can be described as:

$$\alpha = \frac{\Delta L}{L\Delta T} \quad \text{Equation 3.6}$$

where L is the length of material in the direction being measured; ΔL is the change in length of material in the direction being measured; ΔT is the change in temperature over which ΔL is measured.

In this thesis, the CTE of the composites was evaluated by thermomechanical analysis (TMA, Q400 TMA) from room temperature to 100 °C with 5 °C min⁻¹ heating rate under 0.02 N force. In this thesis, the CTE values of the samples are calculated before the glass transition temperature (T_g).

3.7.5 Thermogravimetric Analysis (TGA)

TGA is a method employed to track variations in the weight of a sample over temperature or time. During a TGA experiment, the sample is heated or cooled at a controlled rate in an inert atmosphere (usually nitrogen) or in the presence of a specific gas (such as oxygen). As the temperature changes, the mass of the sample is continuously monitored using a highly sensitive balance. This allows researchers to analyse thermal stability, decomposition, oxidation, and other temperature-dependent processes of the sample. TGA is widely used in various industries and research fields

to study the thermal properties of materials, determine their composition, and assess their stability under different conditions. In this study, TGA experiments were performed using SDT Q600. The samples were placed in an aluminium oxide crucible, and their weight change was recorded with the temperature change from room temperature to 700 °C in the air with a 5 °C min⁻¹ heating rate.

3.8 Electrical resistance measurement

Electrochemical Impedance Spectroscopy (EIS) is a powerful analytical technique used to study the electrical properties of materials, particularly those involved in electrochemical processes. It involves applying a small amplitude alternating current (AC) signal to a material or electrochemical system across a range of frequencies and measuring the resulting impedance response. In this study, the size of samples is 10 mm in diameter and 1 mm in thickness. EIS tests were conducted using the ModuLab XM Materials Test System (Solartron, Hampshire, U.K.), with measurements recorded at room temperature across a frequency range of 0.01 to 1 MHz. Impedance plots were analysed using Zview software (Scribner Associates, Inc.). The values of electrical resistance (R) were obtained from the intercept of the corresponding semicircle on the real part of the impedance, and the corresponding electrical conductivity was calculated by taking the reciprocal of the obtain.

3.9 Evaluation of dielectric properties

3.9.1 Dielectric constant measurement

The prepared composites samples were ground with fine sandpaper (1200 mesh), and the thickness of samples was measured. The size of samples is 10 mm in diameter and 1 mm in thickness. Then, a layer of conductive silver paste was evenly applied to both sides of the samples, which were then placed in a drying oven to dry at 70°C for 1

hour. Afterwards, a ModuLab XM Materials Test System (Solartron, Hampshire, U.K.) was used to test the dielectric loss and capacitance at different frequencies (10^2 - 10^6 Hz). The results were analysed using Zview software (Scribner Associates, Inc.). The dielectric constant (ϵ) is calculated by Equation 3.7.

$$\epsilon = \frac{Cd}{\epsilon_0 S} \quad \text{Equation 3.7}$$

where C is the capacitance of the sample; d (m) is the thickness of the sample, S (m^2) is the surface area of the sample, and ϵ_0 is the vacuum permittivity.

3.9.2 Breakdown strength

A breakdown strength test evaluates the dielectric strength of insulating materials. It determines the highest electric field that a material can endure before it breaks down and becomes conductive. During the test, the material is subjected to increasing voltage until electrical failure occurs. The breakdown strength is calculated as the voltage at failure divided by the material's thickness. This test is crucial for assessing the suitability of materials used in high-voltage applications, ensuring safety and reliability in electrical and electronic systems.

In this thesis, MEGGER performs an 'AC Hipot Test' in which ramp voltage is applied across the insulating material up to the predefined voltage. When a short circuit is detected in a specimen, time to breakdown was noted down until the failure is detected in each specimen. The size of samples is 10 mm in diameter and 1 mm in thickness.

Chapter 4 3D SiC Whiskers Networks for Polymer Composites with Improved Thermal Conductivity

In this chapter, drawing inspiration from the reported directional freeze casting method, herein, we chose micro-sized SiC whiskers (SiCWs) as fillers to construct 3D networks by using an anisotropic mould made of different materials. In this work, we demonstrate that the freeze casting method can be applied to tailor the microstructure of SiCW aerogels. Furthermore, the impact of sintering temperature on SiCW aerogels in the sintering process was first investigated. The formation of SiO₂ layer on SiC fibres was demonstrated, and the effect of the SiO₂ layer on the thermal conductivity of composites has been investigated in this chapter. We also establish the relationship between the microstructures and thermal conductivity of 3D SiCW-epoxy composites, which enables the optimization of the properties of the thermally conductive composites in electronic devices.

4.1 Fabrication and characterisation of 3D SiCW network aerogels

As illustrated in section 3.2 and Figure 3.1, the process of creating 3D SiCW epoxy composites unfolds in four stages: (1) freeze-casting the SiC suspension; (2) freeze drying to sublimate the ice; (3) sintering to produce SiCW aerogels; (4) impregnations of epoxy resin. As shown in (Figure 4.1), our mould was made of Cu dish as the bottom and thermally insulating PTFE as the surround. 3D SiCW network aerogels of various shapes, such as cylinder and cuboid, could be conveniently manufactured by employing various moulds (Figure 4.1a), which was advantageous for use in various electrical devices. Figure 4.1b shows the 3D SiCW network aerogels after being

sintered. The obtained aerogels have low density and high porosity as shown in Table 4.1. The 3D SiCW network aerogel exhibits a light skeleton that was put on ear of wheat without bending the ears (Figure 4.1c). It is worth noting that the 3D SiCW aerogel can support up to 1800 times its own weight (235g, Figure 4.2a), as shown in Figure 4.2c, while it is very light weight (about 0.13g, Figure 4.2b). To further investigate the strength of aerogels, the through-plane compressive test is performed to determine the mechanical properties. The compressive stress-strain curve of 3D SiCW aerogel is shown in Figure 4.1d. The 3D SiCW aerogel exhibits classical foam behaviour, in which an elastic region at low strain (<9%) is followed by compaction with increasing compressive strain [178]. The yielding behaviour occurred due to the collapse of 3D network structure [179]. Before collapse the compressive strength of the 3D SiCW aerogel is 32.5 kPa at 8% compressive strain. These results reveal that the obtained SiCW aerogels have strong mechanical strength. The robustness of the networks favourably ensured their preservation throughout the following epoxy composite fabrication process.

Table 4.1 The solid volume loading, density and porosity of 3D SiCW aerogels with different solid loading.

Group	Aerogel	Solid loading (vol%)	Density (g/cm ³)	Porosity
A	SiCW-2.5	2.5 vol%	0.089	97.2%
B	SiCW-3.6	3.6 vol%	0.1276	96.1%
C	SiCW-4.6	4.6 vol%	0.1590	95.0%
D	SiCW-5.7	5.7 vol%	0.1910	94.0%
E	SiCW-6.7	6.7 vol%	0.2117	93.0%
F	SiCW-8.2	8.2 vol%	0.2710	91.5%
G	SiCW-10.2	10.2 vol%	0.3425	89.3%

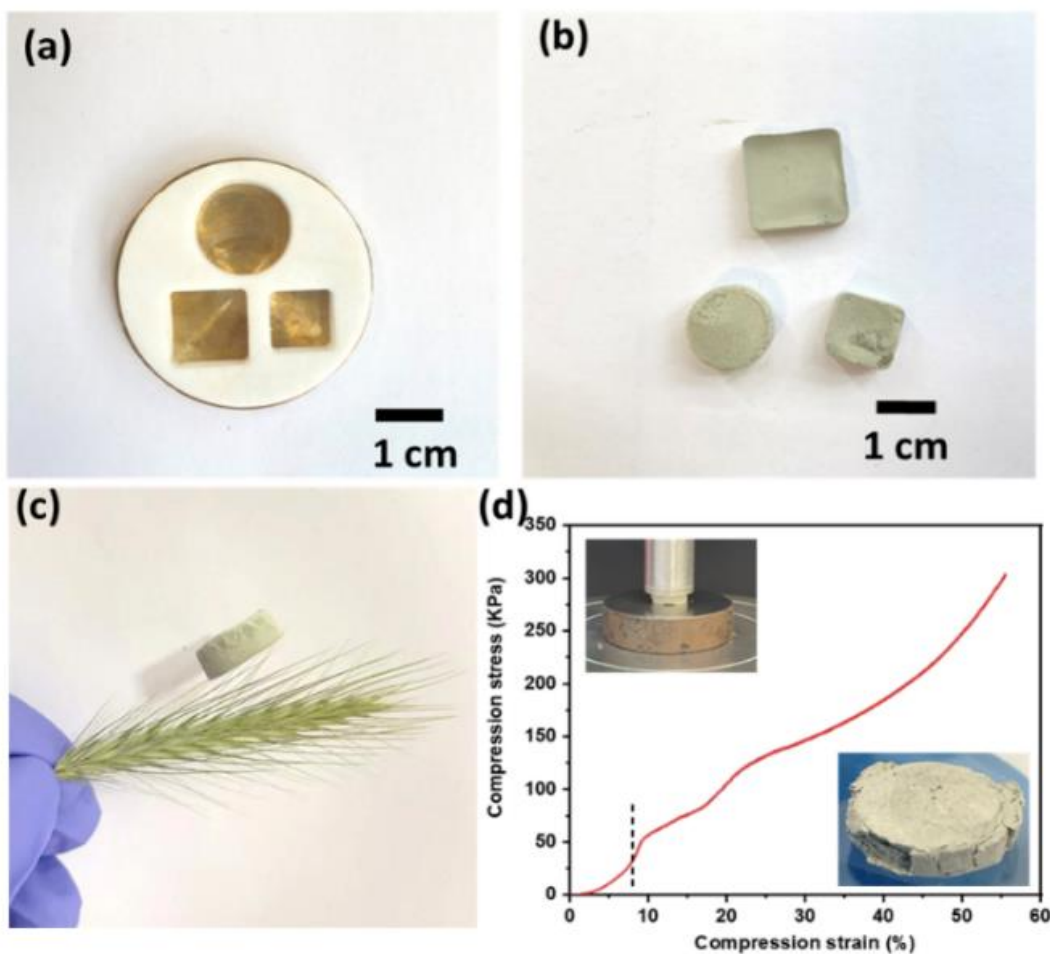


Figure 4.1 Photographs of (a) the mould; (b) 3D SiCW aerogels; (c) Photograph of the 3D SiCW aerogel standing on ear of wheat without bending the ears, demonstrating its light weight; (d) Compression stress-strain curves of 3D SiCW aerogel; inset of (d) shows the process of compression test and the 3D SiCW aerogel after compression.

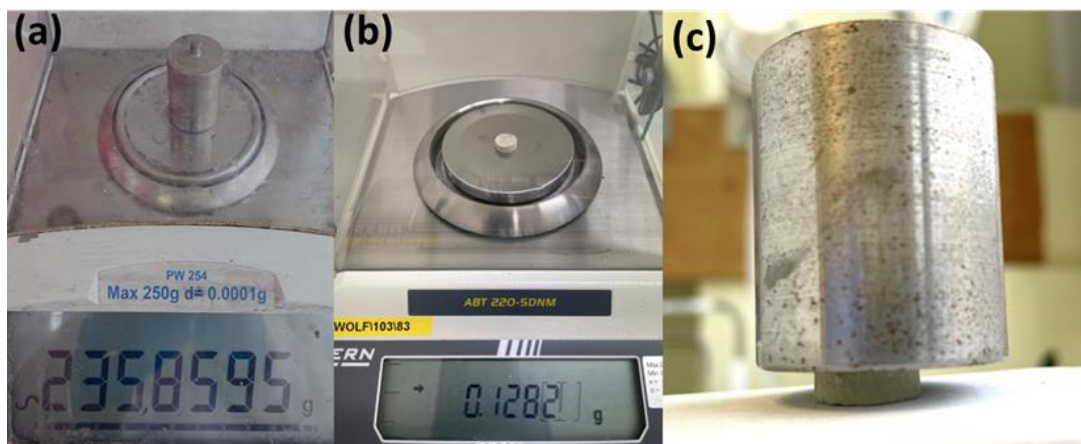


Figure 4.2 Photograph of showing the weight of (a) heavy object, (b) SiCW aerogel, (c) favourable strength of 3D SiCW aerogels.

Figure 4.3a and b show the characteristic morphology of SiC whiskers, with lengths ranging from 5-55 μm and diameters between 1-2.5 μm . The XRD pattern (Figure 4.3e) shows distinctive peaks of cubic β -SiC located approximately at 35.6° , 41.4° , 60.0° , 71.7° and 75.4° . These peaks correspond to the crystal planes (111), (200), (220), (311) and (222), respectively. The minor peak in front of the strongest peak is due to the stacking faults [180]. As shown in the inset of Figure 4.3b, the vertically aligned SiC whiskers are responsible for the reflection from (111) and (222) planes. Therefore, in order to further investigate the orientation of SiC whiskers, the texture coefficient values for (111) and (222) were determined, providing insights into the degree of orientation of SiC whiskers along the through-plane direction, which is parallel to the direction of ice growth, according to the results of XRD (Figure 4.3e and f). As shown in Table 4.2, there is no obvious difference in the text coefficient values of each sample, which indicates the unique structure of SiCW aerogels prepared by the ice-templated method. This can be attributed to the fact that SiC whiskers are not all along the ice growth direction (through-plane direction), and they were woven together in various directions to form SiC layers (Figure 4.3c and d). This is different from aligned aerogels prepared from 2D materials, such as BN, where the orientation of each BN platelet tends to be parallel to the ice crystal growth direction [181].

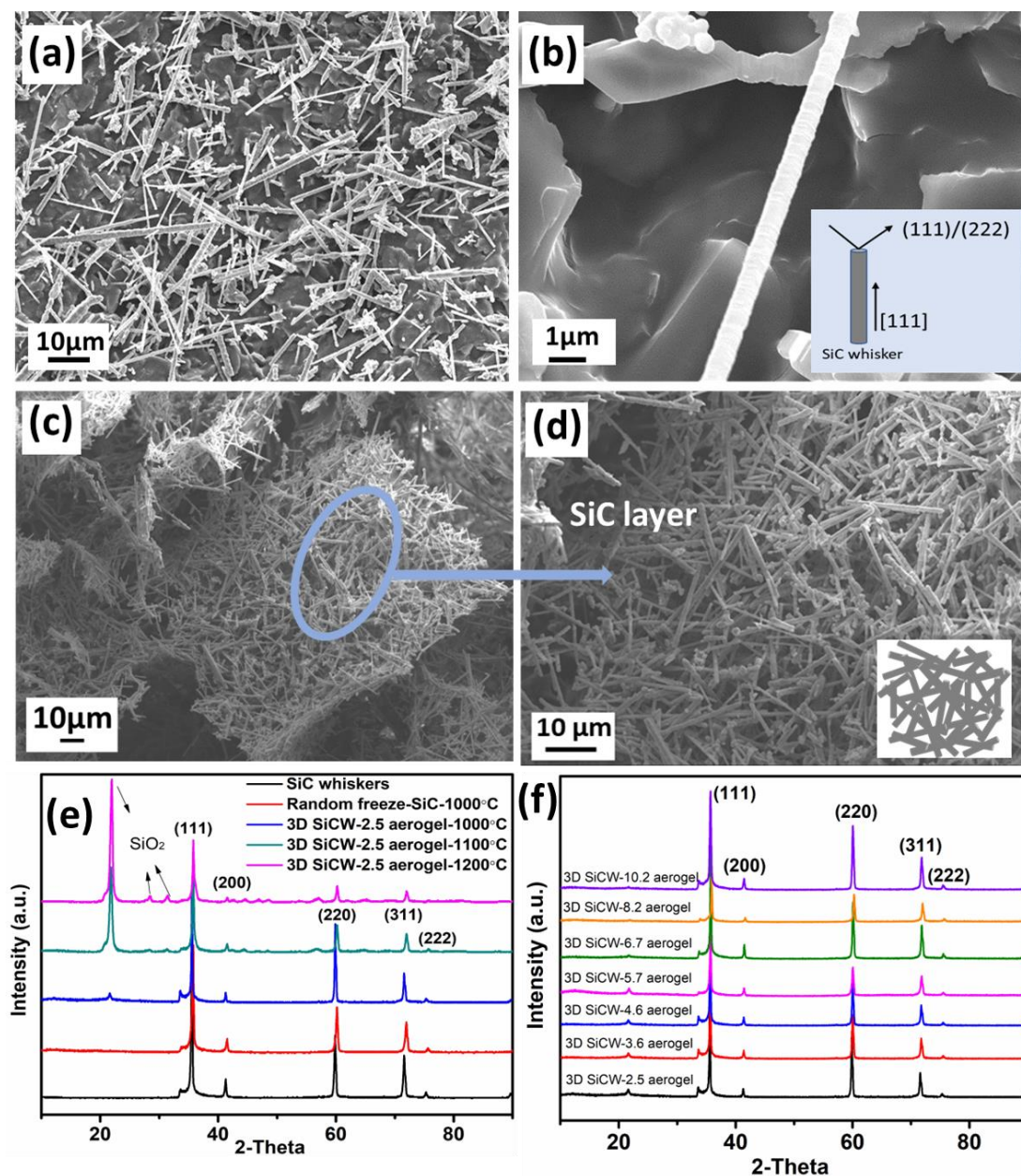


Figure 4.3 SEM images of (a) a cluster of SiC whiskers, (b) an individual SiC whisker; the inset of (b) is the illustration of the effect of SiC whisker orientation on the XRD pattern; (c) (d) SEM images of SiCW aerogel layer at different magnifications; inset of (d) is the schematic illustration of SiCW aerogel layer, (e) XRD pattern of SiC whiskers, Homo-freeze-SiC aerogel and 3D SiCW-2.5 aerogel sintering at 1000 °C, 1100 °C and 1200 °C; (f) XRD pattern of 3D SiCW aerogels with different loading sintering at 1000 °C.

Table 4.2 The Texture coefficient (Tc) of SiC whiskers (SiCWs), Homo-freeze-SiCW aerogel and 3D SiCW aerogels.

Plane	Tc for SiCWs	Tc for Homo-freeze-SiCW	Tc for 3D SiCW-2.5	Tc for 3D SiCW-3.6	Tc for 3D SiCW-4.6	Tc for 3D SiCW-5.7	Tc for 3D SiCW-6.7	Tc for 3D SiCW-8.2	Tc for 3D SiCW-10.2
(111)	2.77	2.65	2.43	2.69	2.68	2.65	2.72	2.26	2.32
(200)	0.33	0.35	0.22	0.25	0.22	0.32	0.31	0.24	0.28
(220)	1.06	1.12	1.63	1.32	1.44	1.11	1.16	1.37	1.50
(311)	0.72	0.75	0.62	0.63	0.60	0.77	0.70	0.95	0.77
(222)	0.11	0.12	0.10	0.11	0.10	0.16	0.11	0.18	0.13

To further investigate the structure of aerogels constructed with SiC whiskers, the SEM images were captured to investigate the microstructures of SiCW aerogels, as shown in Figure 4.4a-g. Figure 4.4a shows that the layers made of woven SiC are vertically aligned, which is due to the preferred growth of ice crystals from surface of the copper disk along the temperature gradient direction in freeze-casting. Therefore, SiCWs were expelled by growing ice crystals, forming a layered microstructure oriented in the direction parallel to the movement of the freezing front. Given the critical influence of the SiCW skeleton's microstructure on the composite's thermal conduction efficiency, SiCW aerogels featuring tailored microstructures were produced by adjusting the SiCW concentration in the initial SiCW-PVA slurry. The amounts of each material used in the experiments were shown in Table 3.1. The porosity and volume fraction of SiC aerogels in epoxy resin are shown in Table 4.1. By increasing the volume fraction of SiC aerogels from 2.5 vol% to 10.2 vol%, the SiCW aerogels with different microstructures were obtained. All these aerogels exhibit a layered hierarchical structure composed of aligned, thin whiskers. But with an increased SiC loading, during the freezing process, growing ice crystals ensnare some

SiC whiskers, positioning them perpendicular to the direction of ice formation. This is likely due to the increased solid content limiting the mobility of SiC whiskers in the freeze-casting phase. These entrapped whiskers form inorganic arms which become the bridge between the adjacent walls. As the concentration of SiC whiskers in the mixture rises, the quantity of bridges grows accordingly. As a result, the corresponding microstructure manifested to be a honeycomb-like structure in SiCW-5.7 aerogel, as shown in Figure 4.4d. Fascinatingly, as the volume fraction increases to 6.7 vol%, the SiC layers manifest a curled form, induced by the compressive forces of the ice crystals. When the volume fraction increased to 10.2 vol%, the SiCW aerogel forms a dense 3D woven structure, as shown in Figure 4.4g, a large number of SiC fibre “bridges” are formed in the middle of the vertical layer structure. Figure 4.5 shows the SiCW aerogel prepared by homogeneous freeze casting method which was named as Homo-freeze-SiCW. Comparing Figure 4.4a with Figure 4.5c, it is apparent that the Homo-freeze-SiCW with a 2.5 vol% loading still displays some aligned structure. However, the layered structure appears less defined, characterised by a multitude of randomly distributed fibres observed between the layers. This phenomenon is attributed to the random growth direction of ice under homogeneous freezing conditions, resulting in a less ordered structure in Homo-freeze-SiCW-2.5 compared to SiCW-2.5 prepared using the unidirectional freeze casting method. In addition, the structure of Homo-freeze-SiCW with a 10.2 vol% loading is completely disordered (Figure 4.5d), attributed to the high solid loading which increases the slurry concentration, subsequently hindering fibre movement and blocking ice growth.

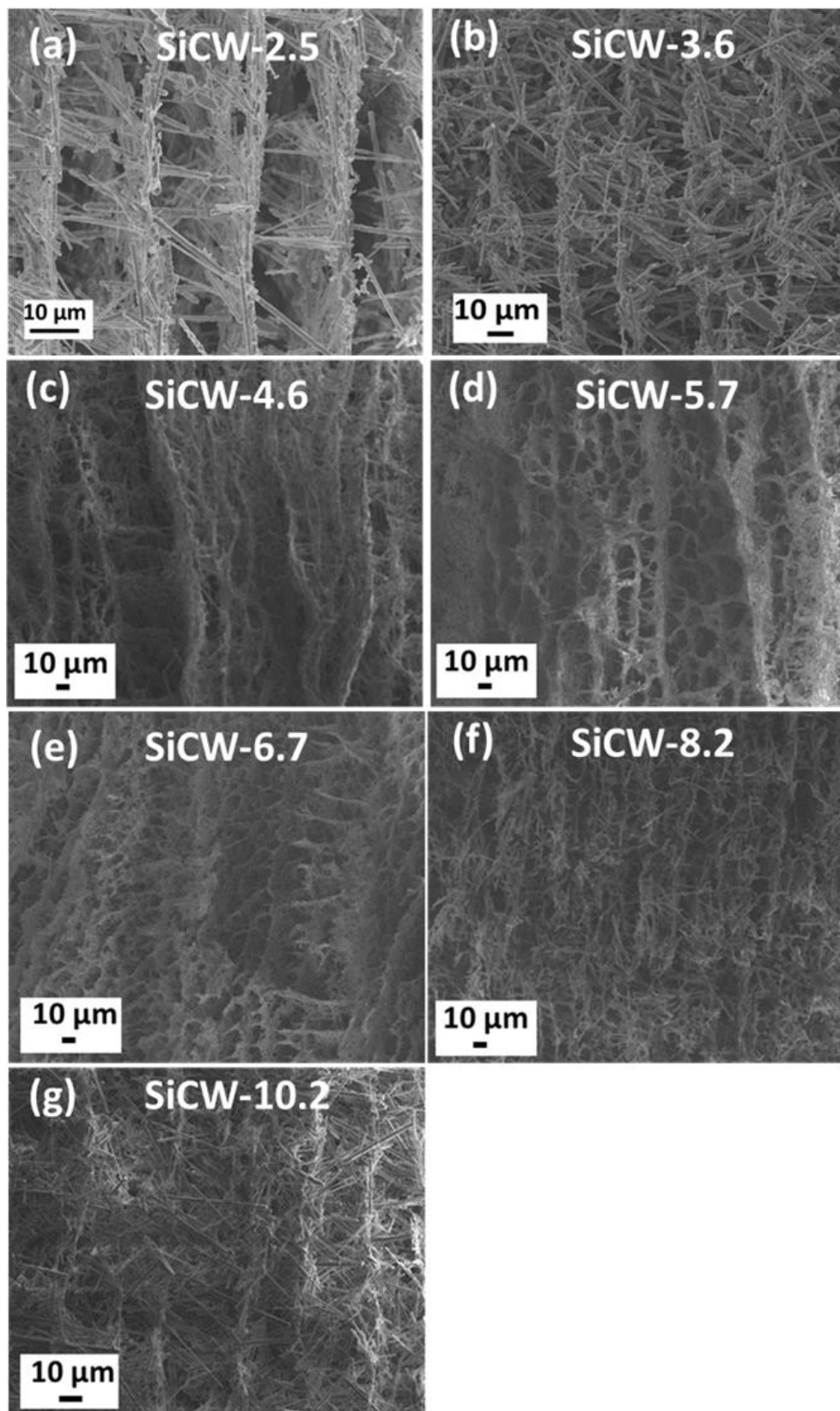


Figure 4.4 SEM images of the cross-section of 3D SiCW aerogels with various solid loadings (a) SiCW-2.5; (b) SiCW-3.6; (c) SiCW-4.6; (d) SiCW-5.7; (e) SiCW-6.7; (f) SiCW-8.2; (g) SiCW-10.2.

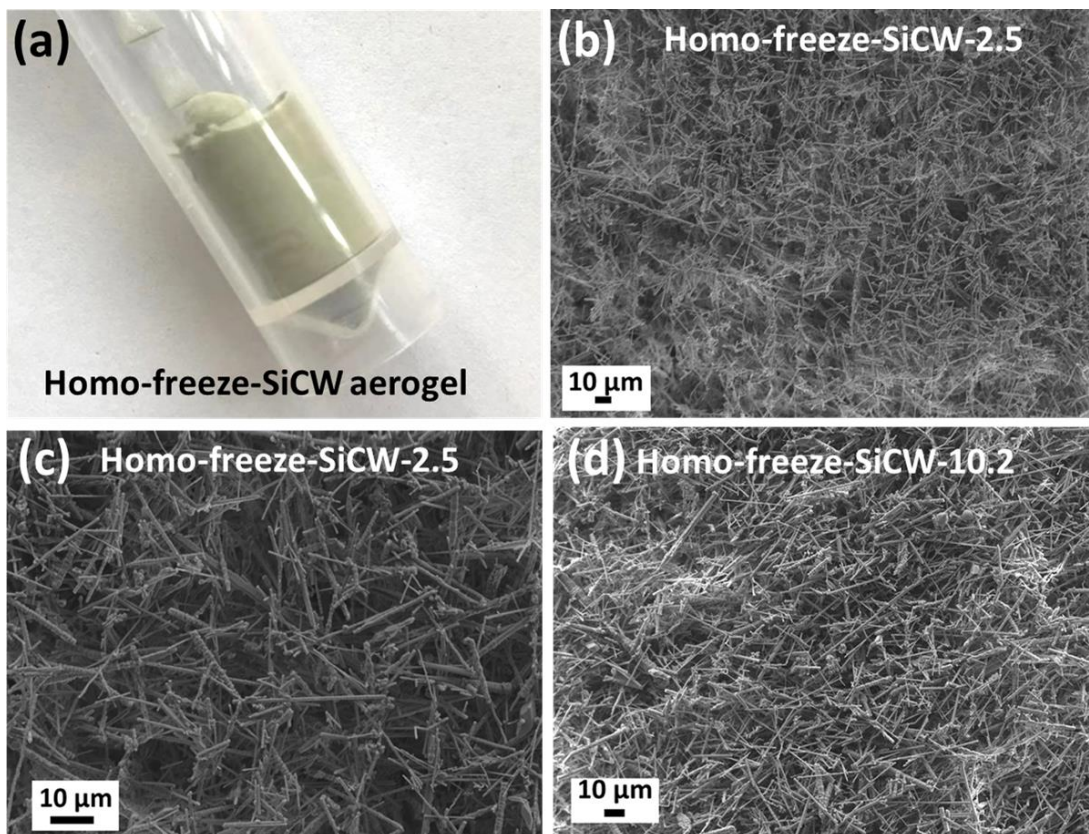


Figure 4.5 (a) Digital photograph of SiCW aerogel fabricated by homogeneous freeze casting method; SEM images of (b) (c) SiCW aerogel with 2.5 vol% loadings fabricated by homogeneous freeze casting method followed by sintering at 1000 °C for 3 hours; (d) SiCW aerogel with 10.2 vol% loadings fabricated by homogeneous freeze casting method followed by sintering at 1000 °C for 6 hours.

PVA served not just as a binding agent, but also as a mechanism to regulate the movement of the whiskers within the suspension. To illustrate the impact of PVA, a sequence of experiments was carried out to prepare SiC suspensions containing different concentrations of PVA (Table 4.3). Figure 4.7a-g shows the morphology of the aerogels with 3.6 vol% loading of SiC prepared from suspensions with PVA concentrations of 0.5, 0.9, 1.4, 2.7, 3.6, 4.4, 8.5 wt%. Clearly, the aerogels' microstructure is significantly influenced by the PVA concentration, which dictates the slurry's viscosity. The number of bridges increases with the increasing PVA concentration in the slurry, but when the PVA concentration is higher than 4.4 wt%,

the aligned structure gradually disappeared. The microstructure of the aerogel is completely disordered when the concentration of PVA is up to 8.5 wt%. The reason is the high viscosity of slurry inhibits the movement of SiC whiskers and ice growth, most SiC whiskers are entrapped in ice crystals. In addition, the high concentration of PVA in aerogels leads to obviously shrinkage of the aerogel because the sintering process removes PVA and the SiC whiskers are not sufficient to maintain the original shape of the aerogels as shown in Figure 4.7h. Figure 4.7i-l shows SEM images of the cross-section of SiCW-PVA-4.4 aerogels with PVA before sintering. The majority of SiC fibres are encased in PVA, and the aligned microstructure could still be observed inside the aerogel, but Figure 4.7k and l demonstrate that the aligned material is predominantly composed of PVA rather than SiC fibre woven layers. In this sample, SiC whiskers are randomly dispersed and surrounded by PVA polymer. During the process of sintering, PVA is removed leaving the SiC fibres unsupported. Consequently, the fibres bond closely to support each other, leading to overall structural shrinkage and increased density, as depicted in Figure 4.6 and Table 4.4.

Therefore, the concentration of SiCW and PVA used in the preparation of aerogels needs to be within a certain range for the microstructure of aerogels to exhibit an aligned or network structure while maintaining the shape of the aerogel. The concentration range of SiCW needs to be from 4.7 wt% to 23.0 wt% in the beginning slurry, and the corresponding aerogels were prepared in composites with a volume loading from 2.5 to 10.2 vol%. For PVA concentration, as shown in Figure 4.6, as the PVA content increases, the volume of the aerogel is gradually reduced after sintering, but when the PVA content is less than 1.4 wt%, the volume reduction is smaller, and the aerogel also has a 3D network structure at the same time. Therefore, the

concentration range of PVA needs to be from 0.4 wt% to 1.4 wt%. Meanwhile, the mass ratio of SiC to PVA should ideally be higher than 5 to 1.

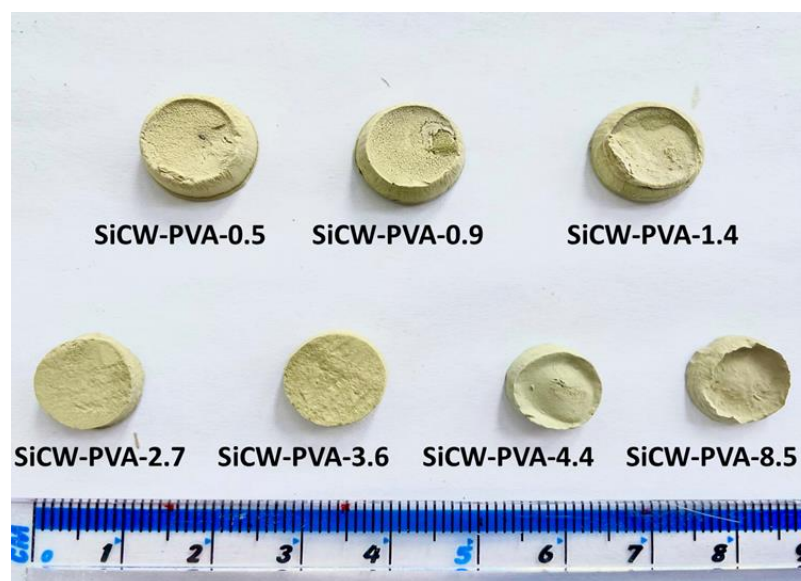


Figure 4.6 The photos of SiCW-PVA aerogels with different PVA contents.

Table 4.3 The weight (W_{SiC} , W_{PVA}) and volume (V_{H_2O}) used to prepare SiCW aerogels with different PVA contents; SiC/PVA is the weight ratio of SiC and PVA, SiCwt% is the weight percentage of SiC in the suspension; PVAwt% is the weight percentage of PVA in the suspension.

Group	Named	$W_{SiC}(g)$	$W_{PVA}(g)$	$V_{H_2O}(ml)$	SiC/PVA	SiC wt%	PVA wt%
B	SiCW-PVA-0.5	0.8	0.05	10	16:1	7.4%	0.5%
B1	SiCW-PVA-0.9	0.8	0.1	10	16:2	7.3%	0.9%
B2	SiCW-PVA-1.4	0.8	0.15	10	16:3	7.3%	1.4%
B3	SiCW-PVA-2.7	0.8	0.3	10	16:6	7.2%	2.7%
B4	SiCW-PVA-3.6	0.8	0.4	10	16:8	7.1%	3.6%
B5	SiCW-PVA-4.4	0.8	0.5	10	16:10	7.1%	4.4%
B6	SiCW-PVA-8.5	0.8	1.0	10	16:20	6.8%	8.5%

Table 4.4 The density and porosity of SiCW aerogels with different PVA contents.

Group	Aerogel	Density (g/cm ³)	Porosity
B	SiCW-PVA-0.5	0.1276	96.1%
B1	SiCW-PVA-0.9	0.1380	95.7%
B2	SiCW-PVA-1.4	0.1497	95.3%
B3	SiCW-PVA-2.7	0.1680	94.7%
B4	SiCW-PVA-3.6	0.1760	94.5%
B5	SiCW-PVA-4.4	0.2089	93.5%
B6	SiCW-PVA-8.5	0.3325	89.6%

Sintering plays a vital role in the formation of aerogel skeletons. Under high magnification SEM, the aerogel reveals interconnected parts of SiC fibres in joint with each other (Figure 4.8). Specifically, the originally rough surface of SiC fibres due to stacking faults transitions to a smooth texture after sintering [182]. To explore the impact of sintering on SiC fibres, the SiC aerogels are sintered at 1000 °C, 1100 °C and 1200 °C, respectively. XRD was first used to detect changes in samples. A new peak associated with SiO₂ is clearly observed in the XRD pattern of SiC whiskers and SiC aerogels after sintering (Figure 4.3e). In addition, the results of SEM-EDS also show an aligned distribution of element O which is almost the same as element Si (Figure 4.9a-c).

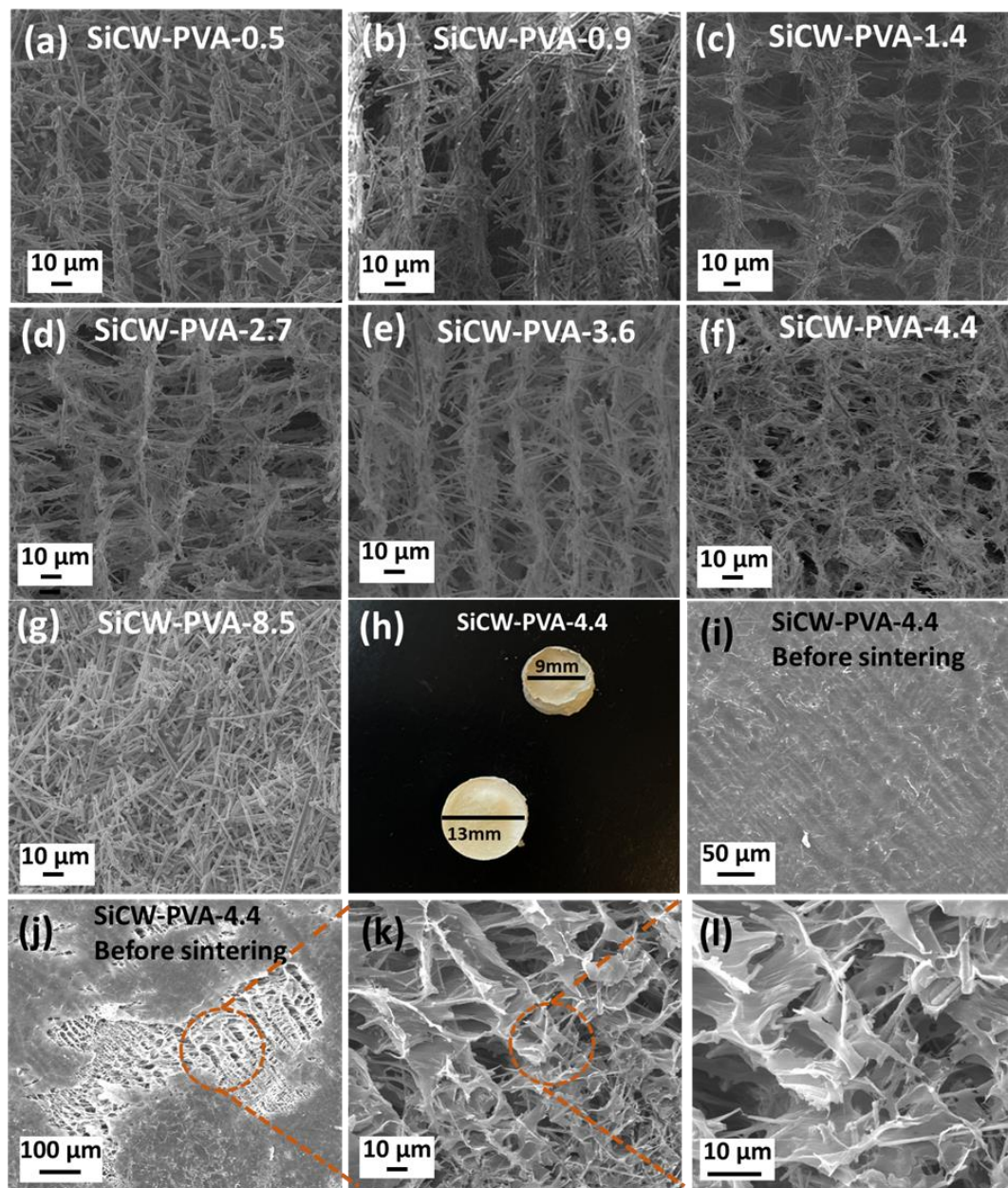


Figure 4.7 Cross-sectional SEM images of SiCW aerogels with different PVA contents: (a) 0.5 wt%, (b) 0.9 wt%, (c) 1.4 wt%, (d) 2.7 wt%, (e) 3.6 wt%, (f) 4.4 wt%, (g) 8.5 wt%; (h) Digital photo of SiCW-PVA-4.4 aerogel before and after sintering; (i-l) Cross-sectional SEM images of SiCW aerogels before sintering with 4.4 wt% PVA content in slurry at different magnifications.

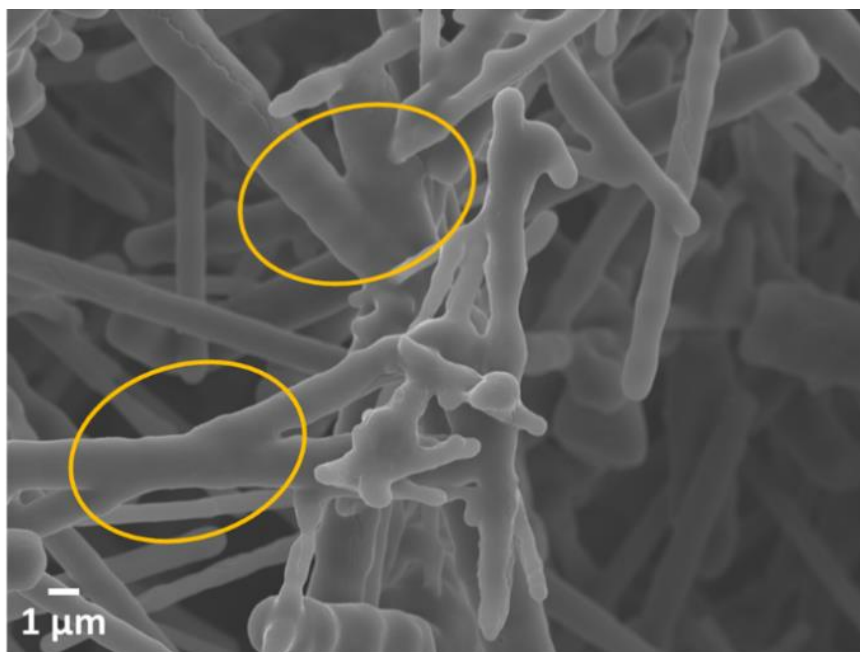


Figure 4.8 SEM image of SiC whisker junctions in 3D SiCW aerogel.

TEM were also applied to investigate the effect of sintering conditions on SiC fibres. In order to obtain clear TEM images, firstly, the FIB-SEM technique was applied to thin SiC fibres. Figure 4.9d shows the process of picking out a SiC fibre which has been sintered at 1100 °C for 6 hours using the needle of FIB-SEM. After putting this fibre on the stage, the focus ion beam was used to thin it to expose the cross-section of SiC fibre (Figure 4.9e). It can be easily observed under SEM that the SiC fibre has a layer on the surface that is completely different from the internal structure, like “a finger biscuit covered with chocolate sauce”. This SiC fibre was subsequently observed under TEM, as shown in Figure 4.9g. The difference between the internal and external structures were analysed separately by Selected Area Electron Diffraction (SAED) (Figure 4.9f). The crystalline structure inside the SiC fibres is clearly observed, however, the outer layer is an amorphous shell because the SAED pattern only have a bright spot in the centre. The observation of the local surface using TEM-EDS reveals that this outer layer contains both O and Si elements (Figure 4.9h-j). All these results

indicate that high temperature treatment can lead to the formation of SiO₂ on the surface of SiC fibres.

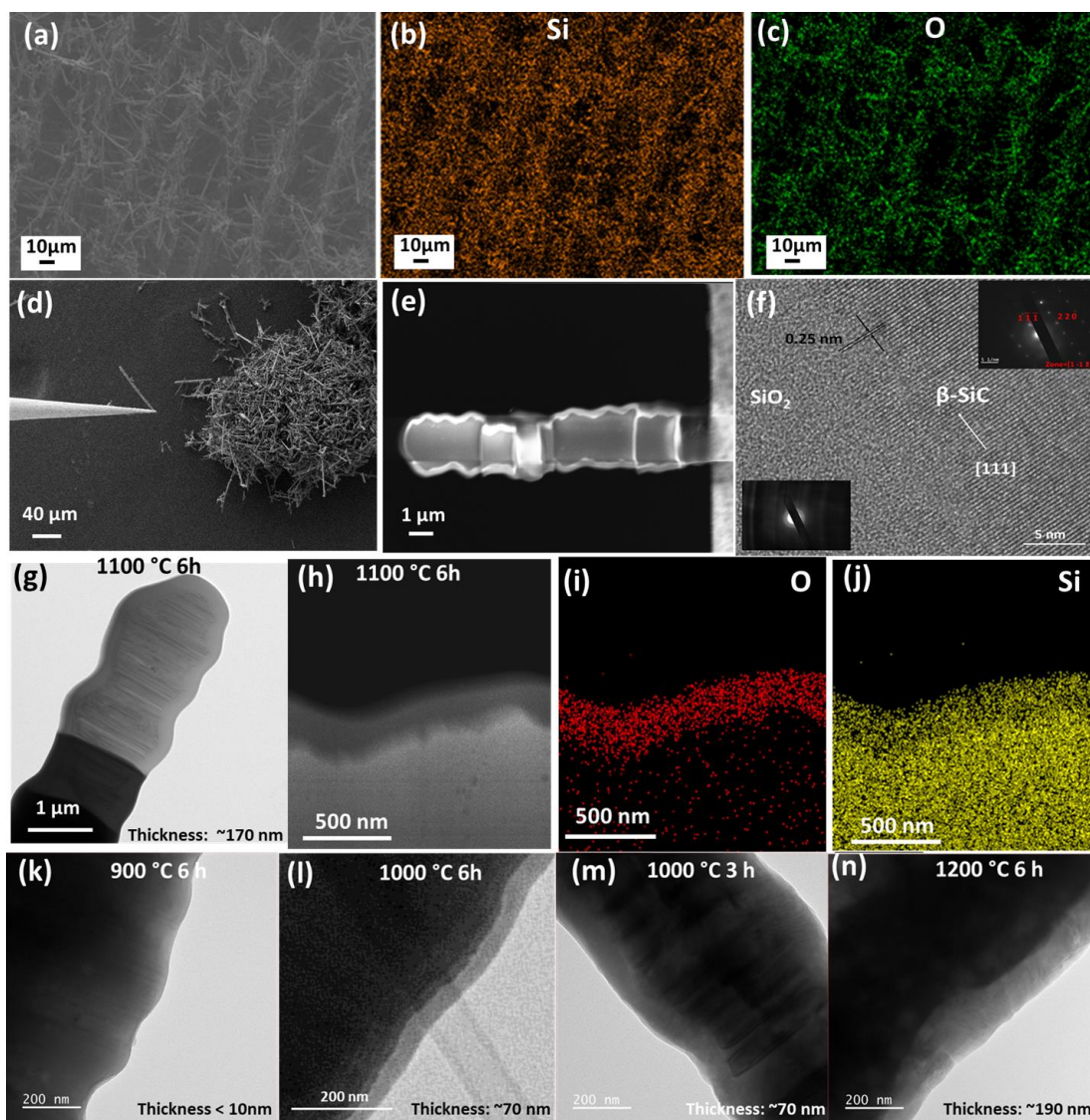


Figure 4.9 (a) SEM images for EDS scanning of SiC aerogel after sintering at 1200 °C; (b) Elemental mapping of Si; (c) Elemental mapping of O. (d) FIB-SEM images of picking out a SiC fibre by the needle; (e) SEM images of SiC fibre after polishing by focus ion beam; (f) high magnification TEM image of transfer interface, the insets of (f) show the SAED pattern of inner core and outer layer of SiC fibre; (g) TEM images of SiC fibre sintered at 1100 °C for 6 hours after polishing by FIB-SEM; (h) TEM images of local surface for EDS scanning of fibre shown in (g); (i) Elemental mapping of O; (j) Elemental mapping of Si. TEM images of SiC fibre sintered at (k) 900 °C for 6 hours, (l) 1000 °C for 6 hours, (m) 1000 °C for 3 hours, (n) 1200 °C for 6 hours.

The thickness of SiO₂ on the surface of SiC fibre sintered at 1000 °C is about 70 nm, much less than that of sintered at 1100 °C (thickness, ~170 nm) and 1200 °C (thickness, ~190 nm) (Figure 4.9g, l and n). This result is consistent with the XRD results of increasing intensity of the peak related to SiO₂ with increasing temperature. The most important thing is that newly generated SiO₂ on the surface of SiC whiskers fill the gaps left by the removal of PVA and promote fibre-to-fibre bonding (Figure 4.8), resulting in the robust mechanical strength of the networks. To further reveal the role of SiO₂, the SiCW aerogel with PVA has also been tried to treat at 600 °C to remove PVA, instead of being treated at 1000 °C or higher, but the aerogel collapses and becomes powder again, because there is no SiO₂ formed at 600 °C.

4.2 Structural characterisation of 3D network SiCW-epoxy composites

After impregnation, the epoxy resin fills the pores of the 3D SiCW network, depicted in Figure 4.10. Minimal distortion happened during the infiltration phase due to the stable interconnected structures. The existence of aligned white lines in Figure 4.10a indicates that SiC structures remain intact within the epoxy resin. The composite's parallel polymer sections are encased by the vertically structured SiC layers, positioned between these sections. The orderly distribution of SiC whiskers within the composites was further confirmed by EDS (Figure 4.10b and c). The elemental EDS mapping for Si and O shows that the SiC whiskers and epoxy resin are neatly layered alternately along the alignment. Such characteristics are advantageous for improving the heat transfer capabilities of SiC composites. The in-plane SiC bridges between the SiC layers could also be observed in the cross-section of the composites, as shown in the white circle in Figure 4.10d. However, the horizontal bridges are less visible compared to the vertically aligned SiC whisker layers, owing to their relatively less in

number. Importantly, the SiC whiskers demonstrate strong adherence to the epoxy resin; there is no noticeable separation at the interface between the epoxy and SiC fibre, as indicated by A in Figure 4.10d and e, based on the cross-sectional analysis of broken 3D SiCWs-epoxy composites. But for the fibre marked B in Figure 4.10d and f, a gap between it and the epoxy can be observed, which is formed during the brittle fracture, suggesting that the interface between them is non-wetting [183]. As a result, some cavities (red circle in Figure 4.10d) on the epoxy can also be seen in the SEM image due to the SiC fibre being flaked off during the fracture process. Figure 4.11a and b show SEM images of SiC composites prepared by a randomly directly mixing method which were named R-SiCW-epoxy. The SiC whiskers in the R-SiCW-epoxy samples are completely randomly distributed in the epoxy resin.

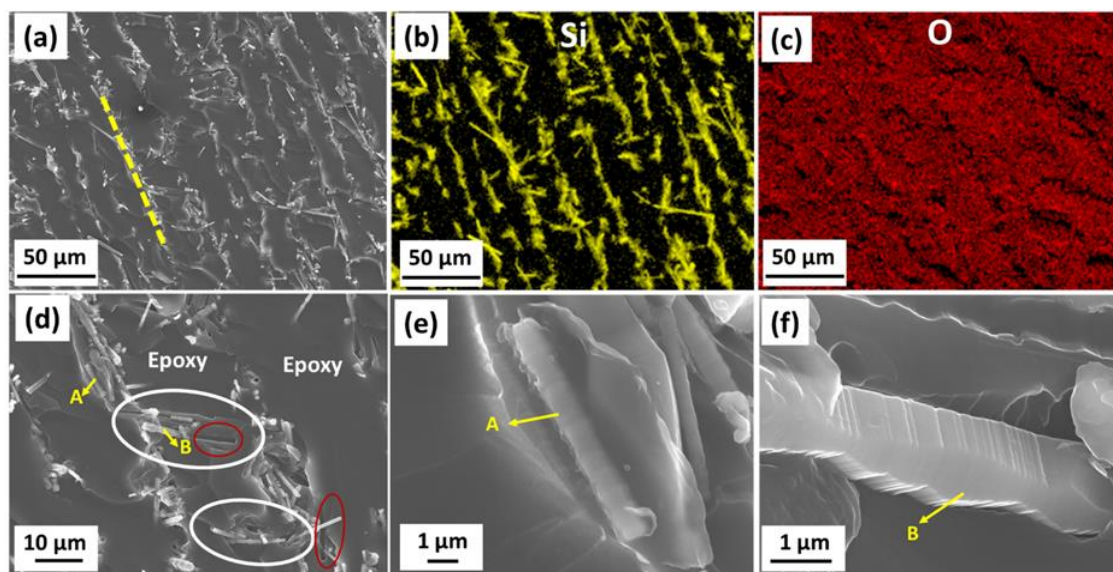


Figure 4.10 (a) SEM images of the fracture morphology in 3D SiCW-3.6-epoxy composites; EDS elemental mapping of (b) Si (c) O; (d) high-resolution SEM images of (a); (e) high-resolution SEM images of the SiC fibre marked A in (d); (f) high-resolution SEM images of the SiC fibre marked B in (d).

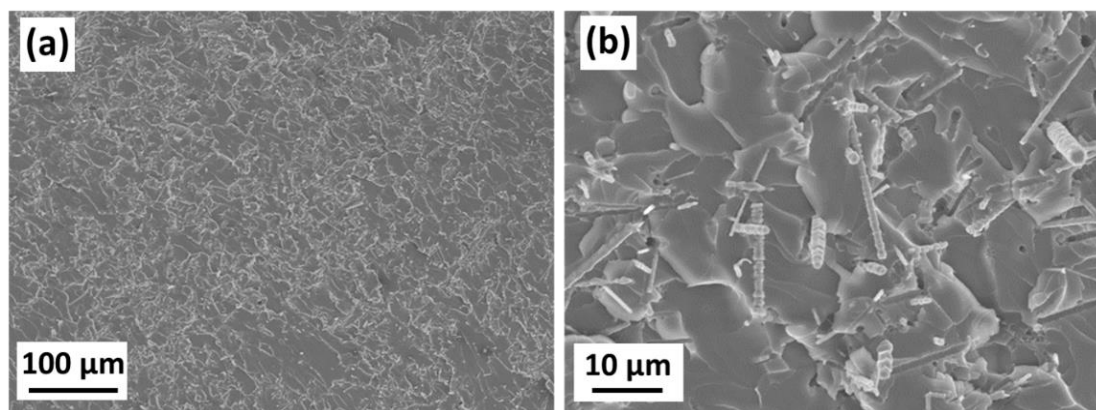


Figure 4.11 (a) (b) SEM images of the cross-section of R-SiCW-epoxy composites at different magnification.

4.3 Thermal and electrical properties of 3D SiCW-epoxy composites

The thermal conductivities of the composites in both through-plane and in-plane directions as a function of SiCW loadings are shown in Figure 4.12a. Pure epoxy resin has an extremely low thermal conductivity of $0.12 \text{ W m}^{-1} \text{ K}^{-1}$ which corresponds closely to the results reported in previous literatures [55, 112]. As expected, thermal conductivity values of 3D SiCW-epoxy composites increased with the SiCW loadings. For example, when the volume loading of SiCW was 2.5 vol%, the thermal conductivity of composites is $0.60 \text{ W m}^{-1} \text{ K}^{-1}$, which was 3.1 times higher than that of pure epoxy resin. At the highest volume loading (10.2 vol%), thermal conductivity values in the through-plane direction for the composites reach $1.55 \text{ W m}^{-1} \text{ K}^{-1}$, which was 8.1 times that of pure epoxy resin. Significant improvement may be attributed to that the vertically aligned SiCW networks served as thermally conductive pathways array throughout the composites (Figure 4.12b). Because of the anisotropic microstructure of 3D SiCW network, there is a distinct contrast in thermal conductivity between the through-plane and in-plane directions under the same loading. It is interesting to note that the in-plane thermal conductivity also increases gradually with

SiCW loading, and there is a dramatic increase as the loading rises from 4.6 to 5.7 vol%, which corresponds to the results shown in Figure 4.4. This is due to more and more cross-linked bridges formed in the in-plane direction, thus creating a pathway for in-plane thermal conductivity. The SiCW loading range from 4.6 to 5.7 vol% marks a critical transition phase for the in-plane thermal conductivity of the composites. This range is the first to demonstrate such changes for SiC fibres using the freeze casting method, as the loading of SiC is usually below 4 vol% in previous studies [36, 59, 184]. Within this range, the SiC whiskers reach a percolation threshold in the in-plane direction, forming continuous and interconnected networks that significantly enhance heat transfer. The number of contact points between whiskers increases, facilitating efficient phonon coupling, and the alignment and orientation of the whiskers improve, creating effective thermal pathways. This leads to a non-linear and substantial increase in thermal conductivity. This range highlights the importance of precise control over filler content and dispersion to achieve high-performance, thermally conductive composites. This phenomenon can also be observed in studies constructing 3D structures BNNS using freeze casting method [118]. When the BNNS loading increases from 5.9 to 9.3 vol%, the in-plane thermal conductivity of the 3D-BNNS epoxy resin composites also shows a significant non-linear increase, indicating that the critical transition range for BNNS is between 5.9 and 9.3 vol% [118].

Another key factor affecting the thermal conductivity of SiCW composites is the filler alignment. The corresponding through-plane thermal conductivity of 3D SiCW-epoxy composites and those of epoxy composites with randomly dispersed SiCWs and Homo-freeze-SiCWs aerogels at the same filler loading is shown in Figure 4.12c. The differences in thermal conductivity among various samples highlight the significance of a connected network and alignment with the direction of heat flow. For example,

the thermal conductivity of 3D SiCW-epoxy resin is $0.60 \text{ W m}^{-1} \text{ K}^{-1}$ at a loading of 2.5 vol%, but that of R-SiCW-epoxy composite is only $0.32 \text{ W m}^{-1} \text{ K}^{-1}$ due to the lack of thermal transfer pathways. Since SiCW aerogels formed under homogeneous freezing conditions could still form an aligned structure locally, the thermal conductivity of composites filled with Homo-freeze-SiCW aerogels is higher than that of composites filled with completely randomly distributed SiCWs at the same loading. Theoretical thermal conductivity (λ) values of SiCW-epoxy composites predicted by Agari's model are shown in Figure 4.12e and f. The logarithmic equation of Agari was given in Equation 4.1 [170].

$$\lg \lambda_c = V_f \times C_f \times \lg[\lambda_f / C_m \lambda_p] + \lg(C_m \lambda_p) \quad \text{Equation 4.1}$$

Where C_m represents the effect of SiCW on the epoxy resin structure; C_f represents the ability of SiCW to continuous thermal conductive chains, the easier formation of thermally conductive channels of fillers, the higher the C_f obtained. V_f represents the volume fraction of fillers; λ_c , λ_f and λ_p represents the thermal conductivity of the composites, fillers and polymer matrix, respectively.

Figure 4.12e and f show the logarithmic values of the thermal conductivity as a function of the SiCW volume fraction. Herein, λ_f is $120 \text{ W m}^{-1} \text{ K}^{-1}$ and λ_p is $0.12 \text{ W m}^{-1} \text{ K}^{-1}$ [184]. According to Equation 4.1, the parameters of C_f and C_m for 3D SiCW-epoxy composites are calculated to be 3.53 and 1.67, respectively. The C_f value for R-SiCW-epoxy composites stands at merely 2.79, indicating that the 3D network structure of SiC possesses a more potent capacity for creating uninterrupted pathways for thermal transfer within the composites.

The through-plane thermal conductivity of 3D SiCW-epoxy composites with SiC aerogels sintered at different temperatures is also shown in Figure 4.12d. When the

sintering temperature is above 1000 °C, the thermal conductivity of 3D SiCW-epoxy composites decreases with the increasing sintering temperature. This is because thicker SiO₂ layer generated on the surface of SiC, which affects the heat transfer (Figure 4.9k-n). It is worth noting that at 900 °C sintering temperature, the thermal conductivity of 3D SiCW-epoxy-10.2 vol% is slightly lower than that of the sample sintered at 1000 °C. As depicted in Figure 4.13, there is a minimal variation in the thermal conductivity of the 3D SiCW-epoxy-10.2% when SiCW-10.2 aerogel was sintered at 1000 °C for different durations. This is because the thickness of the SiO₂ remains consistent at the same sintering temperature. However, a prolonged sintering duration may enhance the bonding between SiC fibres, resulting in a slightly elevated thermal conductivity in samples sintered for 6 hours. Figure 4.13b demonstrates how increasing the PVA content negatively impacts the through-plane thermal conductivity of the composites. This occurs because the creation of cross-linked bridges in the in-plane direction decreases the quantity of aligned SiC fibres in the through-plane direction.

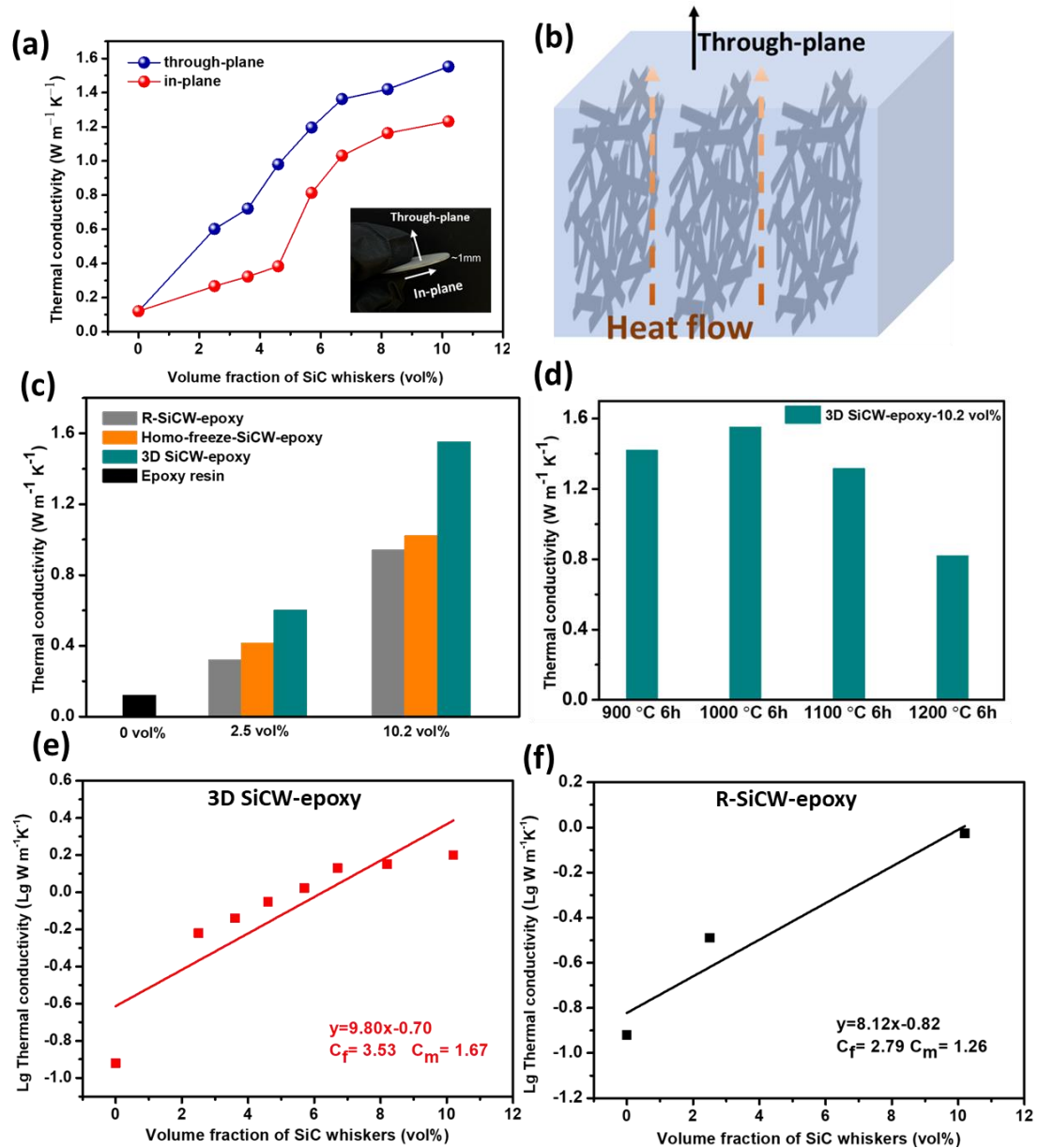


Figure 4.12 (a) Through-plane and in-plane thermal conductivity of 3D SiCW-epoxy composites with aerogels sintered at 1000 °C for 6 hours as a function of filler tested at room temperature; (b) Schematic of the heat dissipation through the 3D SiCW-epoxy resin; (c) Through-plane thermal conductivity of SiCW composites fabricated by different method; Homo-freeze-SiCW-epoxy was prepared by homogeneous freeze-casting method and followed by sintering at 1000 °C for 6 hours; 3D SiCW-epoxy was prepared by unidirectional freeze-casting method and followed by sintering at 1000°C for 6 hours; R-SiCW-epoxy was prepared by mixing SiCW and epoxy directly; (d) The through-plane thermal conductivity of 3D SiCW-epoxy-10.2 vol% with SiC aerogels sintered at different temperature; (e) logarithmic values of the

through-plane thermal conductivity of 3D SiCW-epoxy composites with aerogels sintered at 1000 °C for 6 hours as a function of the SiCW volume fraction; (f) logarithmic values of the through-plane thermal conductivity of R-SiCW-epoxy composites as a function of the SiCW volume fraction.

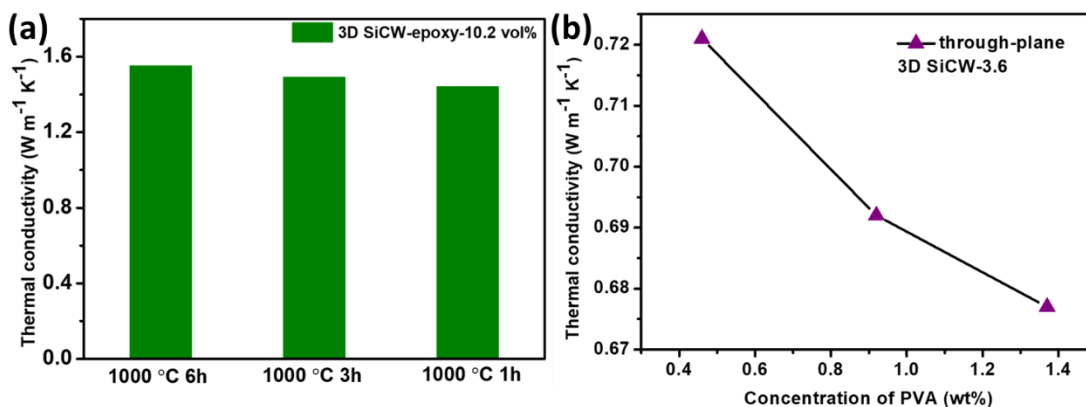


Figure 4.13 (a) Thermal conductivity of 3D SiCW-epoxy-10.2 vol% composites with 3D SiCW-10.2 aerogels sintered at 1000 °C for different hours; (b) Through-plane thermal conductivity of SiCW-3.6-epoxy composites with aerogels prepared by different concentrations of PVA.

Dimensional stability is also a crucial aspect for thermally conductive materials in ensuring the reliability of electronic devices. The influence of SiC loading on the CTE and T_g is analysed in Figure 4.14 to assess dimensional stability and thermal reliability. The CTE values in both the through-plane and in-plane directions of the 3D SiCW network composites were determined through TMA analysis. As shown in Figure 4.14a, the CTE values for 3D SiCW-epoxy composites decreased dramatically with SiCWs loading. At the SiCW loading of 10.2 vol%, the CTE values in the through-plane and in-plane directions are only 48 ppm K⁻¹ and 35 ppm K⁻¹, which were much lower than that of pure epoxy resin (95 ppm K⁻¹). The findings showed that the 3D network composites improved dimensional stability in comparison to pure epoxy resin. The glass transition temperature (T_g), associated with changes in the state of polymer chain motion, is another critical factor influencing the processability and applicability

of polymer composites. Figure 4.14b shows the effect of SiC loadings on T_g for the composites. The results showed that T_g values for 3D SiCW-epoxy composites were all higher than that of pure epoxy resin ($46\text{ }^\circ\text{C}$), which also demonstrated the constraint motions of epoxy resin chains. It is worth noting that, with the increase of SiC loadings of composites, the T_g values first fall and then rise. The reason could be explained as followed: In polymer nanocomposites, because of the non-wetting interface (Figure 4.10f), there is a region surrounding each nanoparticle, and the polymer in this region has high mobility, thus this region was named as “liquid-like interaction zone” [185]. Therefore, when the filler loading increases, the number of “liquid-like interaction zone will increase accordingly. Because of the high mobility of the polymer in these regions, the polymer chains in these regions start to move preferentially when the temperature starts to rise, which means that the more of these regions there are, the easier it is for the polymer chain to mobile at the same temperature, leading to the decrease of the T_g [183, 185, 186]. However, T_g does not decrease further as even more SiC whiskers are added, because saturation occurs [185].

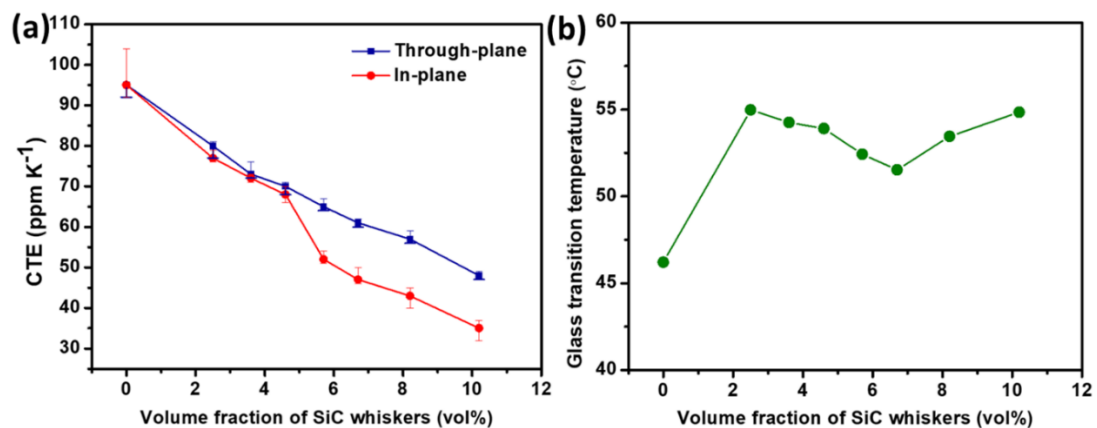


Figure 4.14 (a) CTE values (b) T_g values of 3D SiCW-epoxy composites as a function of SiCW loadings.

A high electrical resistivity for thermally conductive materials is crucial for electrical insulation applications. Figure 4.15 presents the volume resistivity property of the 3D SiCW composites. Compared with the pure epoxy ($1.5 \times 10^{10} \Omega \text{ cm}$), the volume resistivity of 3D SiCW composites decreased by 1 order of magnitude. This could be due to the improved movement of charge carriers along the SiCW. Despite the electrical resistivity dropping to $2.0 \times 10^9 \Omega \text{ cm}$, which remains above the threshold for electrical insulation ($10^9 \Omega \text{ cm}$), it signifies the effective electrical insulation properties of the 3D SiCWs network composites.

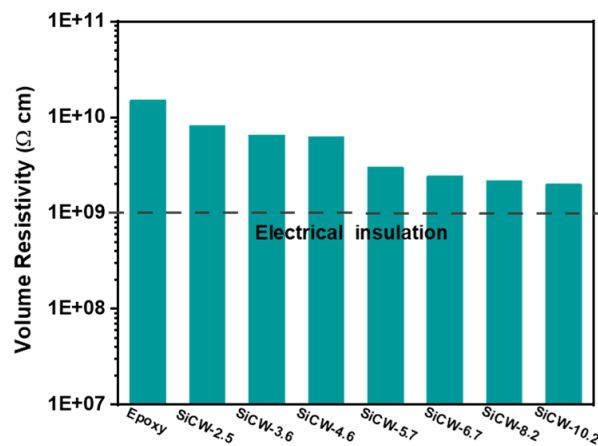


Figure 4.15 Volume resistivity of 3D SiCW-epoxy composites with different SiCW loadings.

To investigate the potential of 3D SiCW-epoxy composites in thermal management application, the changes in surface temperature of composites over time during heating were investigated using an infrared thermal imager. For this purpose, samples of epoxy, R-SiCW-epoxy, and 3D SiCW-epoxy composites were positioned on the heating plates ($\sim 50 \text{ }^\circ\text{C}$) to assess the ability to absorb heat (Figure 4.16). The changes in surface temperature over time, along with the related infrared thermal images, are displayed in Figure 4.16b-f. Figure 4.16b shows the temperature of the samples at the beginning which is $25.1 \text{ }^\circ\text{C}$, and after 25 s, the temperature of epoxy resin, R-SiCW-epoxy and

3D SiCW-epoxy is 38.7 °C, 42.0 °C and 44.7 °C (Figure 4.16c, d and e) respectively. It is worth noting that, in the first 5 s, the surface temperature of the 3D SiCW-epoxy composite increases with time at a higher rate (Figure 4.16f). In order to compare the surface temperature changes of the three samples more visually, all samples were placed together on the hot plate (Figure 4.16g). After 30 seconds, the surface temperature of the 3D SiCW-epoxy was the highest, indicating that the 3D SiCW-epoxy composite can conduct heat the fastest to reach the highest temperature with the same heat source.

In addition to the infrared imaging results, the through-plane thermal conductivity of 3D SiCW-epoxy was found to be $1.55 \text{ W m}^{-1} \text{ K}^{-1}$, and the through-plane CTE was measured at 48 ppm K^{-1} . These results are better than the previously published studies on the enhanced thermal conductivity of composites with aligned SiCW filler networks. For instance, Xiao et al. demonstrated that aligned SiC whisker networks improve thermal conductivity in polymer composites, achieving a thermal conductivity of $0.43 \text{ W m}^{-1} \text{ K}^{-1}$ with 3.91 vol% loading [184]. Similarly, research by Shen et al. on the SiC microwires networks of polymer composites reported a thermal conductivity of $0.62 \text{ W m}^{-1} \text{ K}^{-1}$ highlighted the importance of filler alignment in achieving superior thermal performance [36].

When comparing these findings to commercial materials, such as FR4 (a widely used composite material in PCBs), the advantages of 3D SiCW-epoxy composites become evident. FR4 typically has a through-plane thermal conductivity of around $0.3 \text{ W m}^{-1} \text{ K}^{-1}$ and a CTE of approximately 64 ppm K^{-1} in through-plane direction [187, 188]. The 3D SiCW-epoxy composites exhibit a significantly higher thermal conductivity and a lower CTE, demonstrating their superior thermal management capabilities.

These findings indicate that 3D SiCW-epoxy composites possess significant potential for use in thermal management applications. The high thermal conductivity and low CTE, combined with the rapid heat absorption observed in the infrared imaging, make these composites highly suitable for applications requiring efficient thermal management.

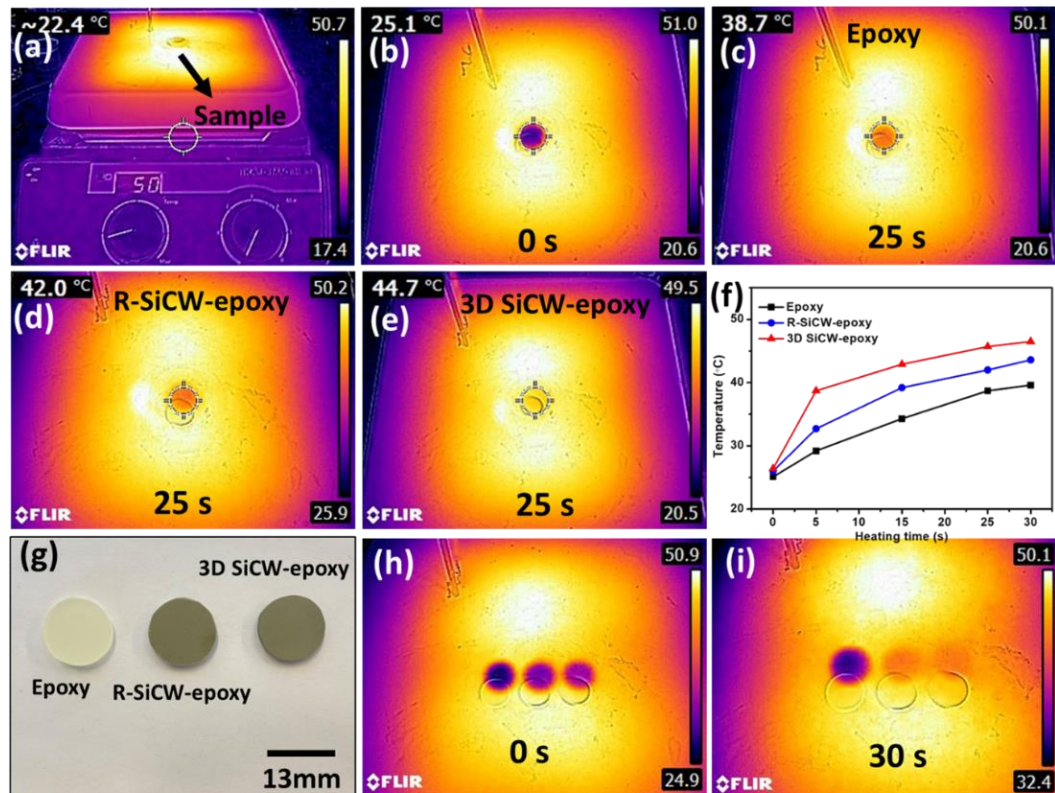


Figure 4.16 (a) Experimental setup for thermal infrared imaging; Infrared thermal images of (b) (c) epoxy, (d) R-SiCW-epoxy, (e) 3D SiCW-epoxy composites; (f) Surface temperature variation with heating time; (g) Optical images of epoxy, R-SiCW-epoxy and SiCW-epoxy composites placed on a hot plate; (h) Infrared thermal images of samples corresponding to (g) at the beginning of heating; (i) Infrared thermal images of samples corresponding to (g) after heating 30 seconds.

4.4 Discussion

4.4.1 The effect of SiCW aerogel structure on thermal conductivity of composites

In this thesis, SiC whiskers were chosen to be thermally conductive fillers to construct aerogels. Fillers act as bridges for constructing thermal conduction pathways, thus the structure of fillers within a polymer matrix is crucial to the thermal conductivity of the composites. The microstructure of SiC aerogels is shown in Figure 4.4, Figure 4.5 and Figure 4.7. SiC nanowires were used to prepare aerogels in previous literature as shown in Table 4.5. The highest through-plane thermal conductivity of SiC nanowire composite is $1.67 \text{ W m}^{-1} \text{ K}^{-1}$ [59]. However, the cost of SiC nanowires is prohibitively high, making it unsuitable for subsequent industrialization and practical applications. In contrast, the price of SiC whiskers is almost only one-hundredth of that of SiC nanowires. The highest thermal conductivity of 3D SiCW-epoxy composite reaches $1.55 \text{ W m}^{-1} \text{ K}^{-1}$ which is quite the same as that of 3D SiC nanowire composite.

This previous research on SiC nanowire aerogels also noticed the SiC nanowires were jointed after sintering but no further details of this process were investigated [59]. In this chapter, XRD (Figure 4.3), SEM and TEM (Figure 4.9) results demonstrate the SiO_2 layer formed on the SiC whisker during the sintering. TEM results confirm the thickness of the SiO_2 layer increases with the increase of sintering temperature. The thermal conductivity results of SiCW composites are related to the variation of SiO_2 thickness. The thermal conductivity of composite with 3D SiC aerogels sintering at $1000 \text{ }^\circ\text{C}$ is the highest. When the sintering temperature exceeds $1000 \text{ }^\circ\text{C}$, the thickness of SiO_2 is increased gradually. Since the thermal conductivity of SiO_2 is lower than that of SiC, SiO_2 layer hinders the heat transmission and increased the thermal resistance at the interface between fillers, leading to a reduction in thermal

conductivity. As the sintering temperature increases from 1000 to 1200 °C, the thermal conductivity of the 3D network SiCW composite decreases from 1.55 to 0.82 W m⁻¹ K⁻¹ (Figure 4.12). However, when the sintering temperature is 900 °C, only a 10 nm thick SiO₂ layer formed on SiC surface cannot facilitate a strong joint between SiC fibre, hence cannot provide an efficient heat transfer path (Figure 4.9m), resulting in a lower thermal conductivity (1.42 W m⁻¹ K⁻¹). This study fills the gap in research on the sintering conditions of aerogels and their impacts on thermal conductivity.

The SEM results demonstrate unidirectional freeze casting is an effective method for preparing 3D network SiC aerogels. These aerogels display a layered hierarchical structure with the SiC bridges between the layers. The 3D network architecture emerges from the intricate balance between the rate of ice formation and the movement speed of the whiskers. If the ice forms too quickly or the whiskers move too slowly, ice crystals grow before the whiskers move to gaps between the ice, and some SiC whiskers are entrapped in the ice, leading to the creation of perpendicular connecting structures. The higher concentration of solids may impede the SiC whiskers' ability to move swiftly during freezing. Therefore, as the concentration of SiC whiskers in the suspension increases, the microstructure exhibits a honeycomb-like pattern among the layers. As the number of horizontal thermal conduction pathways increases, the in-plane thermal conductivity also rises with the increasing SiC loading. Additionally, the increase in SiC loading leads to a tighter weave of the SiC layers vertically, establishing more pathways for thermal conduction. The highest through-plane and in-plane thermal conductivities are 1.55 W m⁻¹ K⁻¹ and 1.23 W m⁻¹ K⁻¹ with the highest loading of 10.2 vol%. The differences in thermal conductivity among composites produced using various techniques highlight the crucial role of the microstructure of fillers in influencing the thermal conductivity. SiCW aerogel prepared under

homogeneous freezing condition (Homo-freeze-SiCW) has less aligned structure. Thus, the thermal conductivity of composites filled with Homo-freeze-SiCW aerogels has lower thermal conductivity than 3D SiCW-epoxy composites. The randomly mixed SiCW composites (R-SiCW-epoxy) exhibit the lowest thermal conductivity among composites. Because there is no connected network in composites, phonon has to jump from one expressway to another, leading to a relatively longer time. The presence of more gaps and a smaller contact area resulted in increased contact resistance, which naturally led to reduced thermal conductivity.

Some previously reported thermally conductive composites for improving through-plane thermal conductivity are summarized in Table 4.5. Compared the through-plane thermal conductivity value for 3D SiCW-epoxy with previously reported values for polymer composites, the thermal conductivity value of our sample was among the high levels at the identical loading in the literature. To evaluate the thermal conductivity enhancement efficiency, enhancement per 1 vol% loading (η) is introduced as

$$\eta = \frac{K - K_m}{100V_f K_m} \times 100\% \quad \text{Equation 4.2}$$

where K and K_m are the thermal conductivity of the composites and epoxy resin, respectively, and V_f is the loading of fillers. Figure 4.17 shows the η variations for through-plane direction at different filler loadings. The maximum η value reaches 160% at a filler loading of 2.5 vol%. The η value decreases significantly when the fillers loading is higher than 6.7 vol%, which corresponds to the results of the structural changes in the SiCW aerogels. When the filler loading is higher than 6.7 vol%, there are more SiC fibres in the in-plane direction to form the 3D network structure. These horizontally aligned SiC fibres have less contribution of through-plane thermal conductivity, thus decreasing the through-plane thermal conductivity enhancement

efficiency. Table 4.5 summarizes the η of previously reported polymer composites in through-plane direction. The Thermal conductivity and η values of our samples were among high levels compared to previous reported. Compared to other SiC fibres composites, our composites do not exhibit the highest η ; the highest is observed in SiC nanowires. However, nanowires are prohibitively expensive, making them unsuitable for large-scale production. Additionally, their CTE characteristics remain unexplored, and there is a lack of research on composites with SiC nanowires loadings greater than 2.17 vol%. Compared to BN fillers, the thermal conductivity of BNNS composite is higher than that of our SiCW-epoxy with similar filler content using the same freeze casting method. However, the η is comparable between the SiCW and BNNS. This indicates that 2D materials have an advantage over 1D materials in constructing thermal pathways. However, our study also addresses a gap in the research on the use of 1D materials for constructing thermal pathways.

Furthermore, alternative strategies based on the application of electric or magnetic fields and template method have been proposed to align the fillers. For example, the previously reported vertically aligned BN@Fe₃O₄, SiC@Fe₃O₄, AlN@Fe₃O₄ epoxy composites were prepared by magnetic field alignment. By using magnetic field method, Fe₃O₄ needed to be decorated on the fillers first, and the whole process was complex compared to freeze casting method. In addition, the thermal conductivity of composites prepared by magnetic field method is lower than composites prepared by freeze casting at same volume loading. When the volume loading of filler is 10 vol%, the through-plane thermal conductivity of SiC@Fe₃O₄-epoxy is only 0.65 W m⁻¹ K⁻¹, which is only half of the thermal conductivity of 3D SiCW-epoxy composite [189]. Among the freeze casting, electric or magnetic field and template method, our freeze

casting approach is comparatively much more efficient and facile for the enhancement of thermal conductivity.

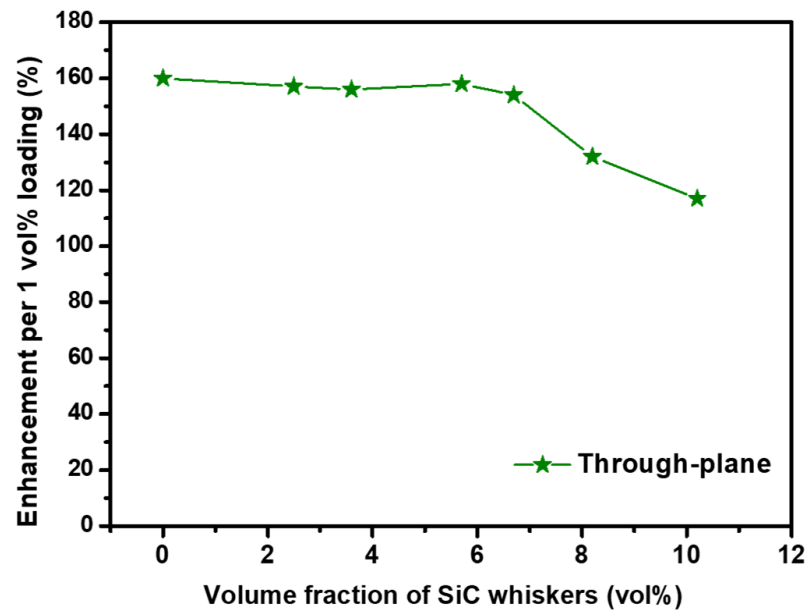


Figure 4.17 Thermal conductivity enhancement efficiency (η) of the composites with different SiC whiskers volume loading.

In this chapter, the relationship among the SiCW loadings, the microstructure of SiCW aerogels and the thermal conductivity has been revealed. This research provides guidance for the subsequent preparation of thermally conductive composites using micrometre-scale fibre materials.

Table 4.5 Comparison of thermal conductivity and CTE of our 3D SiCW-epoxy composite with epoxy-based composites filled with other fillers in the published literature.

Matrix	Filler	Method	Loading (Vol%)	Through-plane Thermal conductivity ($\text{W m}^{-1} \text{K}^{-1}$)	η (%)	CTE (ppm K^{-1})	Reference
Epoxy	SiC nanowire	Freeze casting	2.17	1.67	406	-	[59]
Epoxy	CNF/SiCWs	Freeze casting	1.32	0.62	218	21.9	[36]
Epoxy	SiC nanowire	Template method	3.91	0.43	29	-	[184]
Epoxy	BN	Freeze casting	14	~1.2	36	~40	[111]
Epoxy	BNNS	Freeze casting	9.29	2.85	181	~24	[118]
Epoxy	BN@Fe ₃ O ₄	Magnetic field	~13.5	0.85	28	~28.7	[132]
Epoxy	SiC@Fe ₃ O ₄	Magnetic field	10	0.65	26	-	[189]
Epoxy	AlN@Fe ₃ O ₄	Magnetic field	20	1.754	38.8	-	[101]
Epoxy	BN@Fe ₃ O ₄ /SiC@Fe ₃ O ₄	Magnetic field	10	~1.2	57	-	[190]
Epoxy	BN nanotube	Surface modified	18.5	2.77	73.5	53	[191]
Epoxy	RGO /SWCNT	Freeze casting	3.65	0.69	78	59.42	[130]
Epoxy	Micro SiCW	Freeze casting	10.2	1.55	117	48	This work
Epoxy	Micro SiCW	Freeze casting	2.5	0.60	160	80	This work

4.4.2 The effect of SiCW aerogel structure on CTE

CTE is the major physical property when the materials are exposed to a temperature changing environment. It can be observed from the Table 4.5 that there has been

limited research on the CTE of thermally conductive composites in previously published studies, thus this gap needs to be filled urgently.

CTE results (Figure 4.14) show the dramatic decrease with the increase in SiC loading. This reduction is attributed to the suppression of the volume change in the alternate layered structure between SiCWs and epoxy in the interstitial space. Another possible reason is that the epoxy resin molecular chains were constrained in the SiCWs networks and therefore their motion ability was limited. What is more, the increased SiC has lower CTE than epoxy resin, therefore, when fillers with a lower CTE occupy an increased volume in the polymer, the overall CTE of the composite naturally decreases. In addition, the 3D SiCW-epoxy composites exhibit anisotropic CTE in the through-plane and in-plane directions. The CTE values in the in-plane direction are lower than those in the through-plane direction, which is because there are more layered structures perpendicular to the in-plane direction than parallel to the in-plane direction. These results demonstrate CTE values rely on the orientation of fibres and fibre volume fraction.

CTE is influenced by the material's structure. In single-phase materials, CTE is determined by atomic bonding, molecular structure, and assembly. As temperature rises, thermal energy increases, leading to greater atomic movement. Materials with weak atomic bonds and low bonding energy exhibit larger CTEs due to increased interatomic distances. In multiphase materials like composites, CTE depends on each component phase, their interactions, volume fraction and composite architecture. Weak interfacial bonding fails to effectively combine the contributions of each phase, whereas strong interfacial bonding allows for a balanced thermal expansion behaviour. Strong interfacial bonding ensures effective load transfer and constrains the matrix's

expansion, leading to a lower overall CTE. Poor interfacial bonding can result in differential expansion, causing internal stresses and potential failure.

In this study, the tight bonding between SiC and epoxy resin, along with the high aspect ratio of SiC fibres, effectively suppresses thermal expansion. Previous research has also found that fibrous materials with a high aspect ratio have a greater inhibitory effect on thermal expansion compared to particulate materials. Silica nanofiber filled epoxy showed 1.4 times greater CTE compared to spherical nanoparticle filled epoxy [129].

To analyse the change mechanism of CTE, the simple Rule of Mixture (ROM) was first introduced to describe the CTE of 3D SiCW-epoxy composite. The simple ROM can be given by the following equation [192].

$$\alpha_c = V_f \alpha_f + V_m \alpha_m \quad \text{Equation 4.3}$$

where V_f is volume fraction of fillers, α_f is the CTE of fillers, V_m is the volume fraction of matrix, α_m is the CTE of matrix and α_c is the CTE of the composite.

The CTE of SiC is 3.5 ppm K⁻¹, and CTE of epoxy resin is 92 ppm K⁻¹. When the SiCW loading is 10.2 vol%, the CTE of 3D SiCW-epoxy is 48 ppm K⁻¹ in the through-plane direction (axis direction) [193, 194]. If the theoretical CTE obtained from the calculation using the simple ROM should be 83 ppm K⁻¹, so the simple ROM does not apply and that the rules for the variation of the CTE need to be described by other models. This implies that solely considering the volume fraction and CTE of the filler is insufficient to describe the CTE changes in composites. The arrangement of the filler should also be considered.

Many models such as Turner's model, Mori-Tanaka model, Kerner model and Schapery model which are commonly used to predict the CTE of composite are all tried but they could not fit the results [195-198]. Hirsch model was finally chosen to describe the CTE of the composites [199, 200]. The model is expressed as:

$$\alpha_c = \beta(\alpha_f V_f + \alpha_m V_m) + (1 - \beta) \left(\frac{\alpha_f V_f E_f + \alpha_m V_m E_m}{V_f E_f + V_m E_m} \right) \text{ Equation 4.4}$$

where V_f is volume fraction of filler, α_f is the CTE of filler, V_m is the volume fraction of matrix, α_m is the CTE of matrix and α_c is the CTE of the composite. E_f and E_m are the Young's modulus of the filler and polymer matrix, respectively. β is a parameter ($0 \leq \beta \leq 1$) representing the ratio of the parallel portion. Based on the rule of mixtures, there are two forms of the mechanical responses which are parallel and series. The Hirsch model combines the parallel portion and series portion [201].

The data for calculation the CTE of composites is summarized in Table 4.6 [194, 195, 202, 203]. For the through-plane CTE, to fit the experiment result, the β was determined to be 0.5 when the fillers loading is 10.2 vol% [200]. The calculated CTE results by Hirsch model is approximately 47 ppm K^{-1} which is quite same as the experiment result (48 ppm K^{-1}). This also indicates that when the filler forms a 3D network structure, the mechanical response of the composite has half parallel portion and half series portions.

Table 4.6 The properties of SiC and epoxy. [194, 195, 202, 203].

	CTE (ppm K^{-1})	E (GPa)
Epoxy resin	95	3.2
SiC	3.5	420

4.5 Summary

In summary, 3D SiCW network reinforced polymer composites have been prepared by freeze casting method, for improved thermal conductivity. By adjusting the proportion of raw materials in the suspension, SiCW aerogels with tailored microstructure can be achieved. An optimised 10.2 vol% SiCW loading have been proposed for the preparation of SiCW aerogels by freeze-casting method. The obtained 3D SiCW-epoxy composites exhibit enhanced thermal conductivities, compared with that of random SiCW composite and pure epoxy resin. At the highest SiCWs loading (10.2 vol%), the through-plane thermal conductivity of 3D SiCWs-epoxy reaches $1.55 \text{ W m}^{-1} \text{ K}^{-1}$, which was 8.1 times that of pure epoxy resin, and 1.6 times that of R-SiCW-epoxy composite. This improvement results from the vertically aligned and 3D interconnected network of SiCWs in epoxy resin composites, which provide heat transfer pathways. We have also demonstrated that after sintering, the formation of SiO_2 on the surface of SiCWs has led to a strong structure of the aerogels. However, a thicker SiO_2 layer would form at excessively high sintering temperatures, resulting in lower thermal conductivity. Furthermore, the 3D SiCWs-epoxy composites present a lower through-plane (48 ppm K^{-1}) and in-plane CTE (35 ppm K^{-1}) compared to the pure epoxy resin (95 ppm K^{-1}). This work provides a simple method to fabricate vertically aligned filler networks in polymer composites to improve their thermal performance, which shows promise for use in thermal management applications.

Chapter 5 Development of thermally conductive dielectric bi-layered nanocomposite

In this chapter, bi-layered epoxy composites were fabricated by utilizing epoxy resin as polymer matrix and h-BN platelets and SiC whiskers as thermally conductive fillers, which are anticipated to enhance the thermal conductivity and dielectric constant, keep low dielectric loss and maintain the dielectric breakdown strength of the composites. The thermal conductivity and dielectric properties of Epoxy/BN/SiC bi-layered composite have been investigated in this research. This research aims to gain a more profound insight into how bi-layer embedded fillers of varying dimensions influence the thermal conductivity and dielectric properties of the polymer composites.

5.1 Characterisation of BN/SiC bi-layered film

Following the procedure illustrated in Section 3.3 and Figure 3.2, BN/SiC bi-layered film composite was prepared by carrying out the filtration process of BN and SiC separately, the sample could be clearly divided into two layers which are SiC layer and BN layer as shown in Figure 5.1a and b. The vacuum-assisted filtration process allows the fillers to be evenly distributed, resulting in smooth and uniform surface for the filtered BN/SiC bi-layered film. The grey-green layer is consisting of SiC and the white layer comprises BN. Figure 5.1d and e shows SEM images of the surface of SiC layer and BN layer. It can be observed that both SiC fibres and BN sheets are uniformly distributed in the layers, meanwhile the BN sheets are all flat, which means they were aligned in the horizontal direction. SiC fibres also overlapped each other in the layers and formed an interconnected network in the horizontal direction. This demonstrates

that vacuum-assisted filtration allows the SiC whiskers and BN platelets to be stacked in a uniform and orderly way.

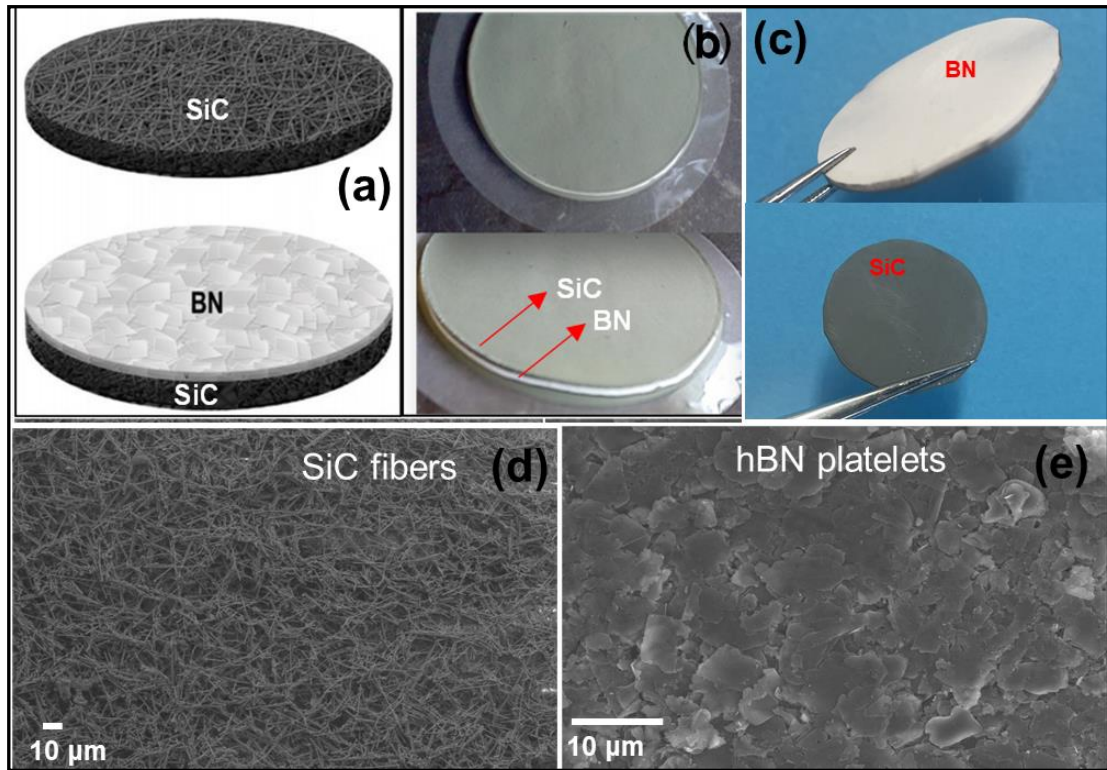


Figure 5.1 (a) Illustration of layer-by-layer structure, (b) Optical images of layered structures (BN/SiC bi-layer), (c) Epoxy/BN/SiC bi-layered composite after epoxy infiltration, SEM image of (d) SiC surface of BN/SiC bi-layer and (e) h-BN surface of BN/SiC bi-layer.

5.2 Characterisation of Epoxy/BN/SiC bi-layered composite

The Epoxy/BN/SiC bi-layered composite was also observed by SEM, as shown in Figure 5.2a-c. The total thickness of Epoxy/BN/SiC bi-layered composite is about 460 μm, of which the SiC layer thickness is 196 μm. In Figure 5.2a, the cross-sectional SEM images shows a distinguishing characteristic in the microstructure bilayer-structured composites: the interfaces between two layers are seamlessly integrated, and no voids or other defects can be observed in the composites, which represents epoxy resin was successfully filled into the BN/SiC bi-layers under the vacuum. Figure 5.2b

and c show microstructure of the surface of each layer. In the layer of EBN, the h-BN platelets are still aligned in the in-plane direction due to the force of vacuum-assisted filtration. The SiC whiskers can also be observed in the SiC layer (Figure 5.2b). The alignment of BN platelets and SiC whiskers was not disrupted by the impregnation of epoxy resin. The surface morphology of the Epoxy/BN/SiC random composite, as seen in Figure 5.2d, showed a stark contrast to that of the bi-layered composites, with BN and SiC particles dispersed randomly across the matrix.

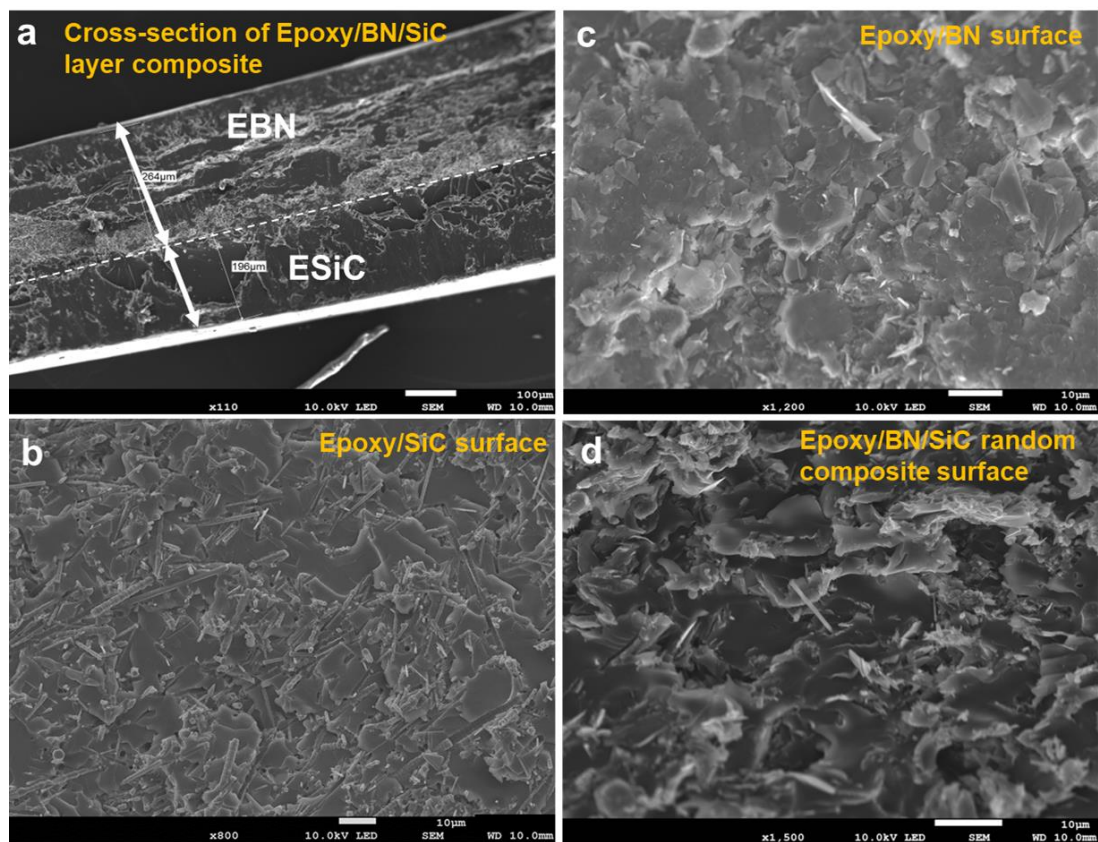


Figure 5.2 SEM images of (a) the cross-section of Epoxy/BN/SiC layered composite; (b) the surface of Epoxy/SiC layer; (c) the surface of Epoxy/BN layer; (d) the surface of Epoxy/BN/SiC random composite.

To further demonstrate the alignment of BN platelets in epoxy matrix, XRD was carried out for SiC whiskers, BN platelets, Epoxy/BN/SiC-Random (EBNSiC_R) composite and the surface on both sides (BN and SiC surface) of Epoxy/BN/SiC bilayered composite (EBNSiC_2L), as shown in Figure 5.3. The XRD pattern of SiC whiskers shows that the peaks at 35.6° , 41.4° , 60.0° , 71.7° and 75.4° correspond to the reflection from cubic β -SiC. For BN platelets powder XRD pattern, the characteristic peaks located at 26.66° , 41.58° , 50.11° and 54.95° correspond to the reflection from (002), (100), (102) and (004) plane of hexagonal BN. These characteristic peaks can also be observed in the XRD patterns of EBNSiC_2L and EBNSiC_R composites, but the intensities of these peaks were different in these composites. The alignment of h-BNs, both horizontally and vertically, contributes to reflections from the (002) and (100) planes respectively [71], as denoted in the inset of Figure 5.3b. To investigate the alignment direction of BN platelets, texture coefficients (T_c) for pure BN powder, EBNSiC_R, EBNSiC_2L-BN surface along three diffraction planes i.e., (002), (100), and (102), were computed and presented in Figure 5.3b [204]. The T_c for a plane denoted by Miller indices (hkl) for n number of peaks calculated (here, $n = 3$) suggests a preferred orientation along that specific plane. For pure h-BN platelets powder, as shown in Figure 5.3b, the $T_{c(002)}$ value is 2.57. This value increased to 2.68 in EBNSiC_2L-BN surface, showing a shift of preferred orientation towards (002) plane. At same time, the $T_{c(100)}$ value of layered structure reduced from 0.32 to 0.21. These results confirm that the BN platelets in layered structure are preferentially orientated along (002) plane which is in-plane direction.

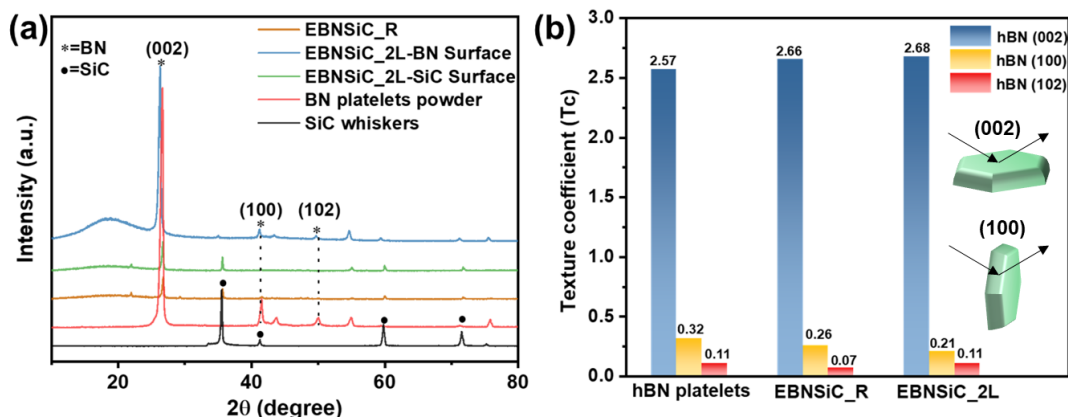


Figure 5.3 (a) XRD patterns of pure BN platelets powder, SiC whisker, EBNSiC_2L-SiC surface, EBNSiC_2L-BN surface and EBNSiC_R; (b) Tc analysis of BN platelets, EBNSiC_2L-BN surface and EBNSiC_R calculated from intensity values of XRD peak data; inset of (b) illustrates the impact of BN orientation on the XRD pattern.

5.3 Thermal properties of Epoxy/BN/SiC bi-layered composite

The interconnected BN platelets aligned along in-plane direction could generate thermally conductive pathways through the composites. To demonstrate the effect of the bilayer structure and the arrangement structure on the thermal conductivity, single layer BN epoxy, single layer SiC epoxy composites and randomly mixed BN/SiC epoxy composites with the same filler loading were fabricated, namely, EBN, ESiC and EBNSiC_R. The measured through-plane and in-plane thermal conductivities of the pure epoxy and different epoxy resin composites are shown in Figure 5.5. From the TGA results (Figure 5.4), the volume loading of fillers in composite is determined as 15.5 vol%. The pure bulk epoxy resin exhibits a low thermal conductivity of $0.12 \text{ W m}^{-1} \text{ K}^{-1}$, which is consistent with previous reports [59]. The presence of fillers increases the through-plane thermal conductivities of all epoxy composites. It is interesting to note that h-BN composite (EBN) shows much higher through-plane

and in-plane thermal conductivity than SiC composite (ESiC). This is due to the intrinsic thermal conductivity of SiC is lower than that of BN.

Figure 5.5 also shows that the through-plane thermal conductivities of the EBN, EBNSiC_R and EBNSiC_2L are quite similar. Since these three samples have limited thermal conductivity paths in the through-plane direction at the same loading. To verify if there is a significant difference between the through-plane and in-plane thermal conductivity of each sample, the data for every composite was analysed statistically. An independent sample t-test statistical method was used to compare the through-plane and in-plane thermal conductivity, and the results are shown in Table 5.1. The t values were calculated by the following equation.

$$t = \frac{\bar{x}_{\parallel} - \bar{x}_{\perp}}{SE} \quad \text{Equation 5.1}$$

$$S = \sqrt{\frac{1}{n-1} \sum_{i=1}^n (x_i - \bar{x})^2} \quad \text{Equation 5.2}$$

$$SE = \sqrt{\frac{s_{\parallel}^2}{n_{\parallel}} + \frac{s_{\perp}^2}{n_{\perp}}} \quad \text{Equation 5.3}$$

where \bar{x}_{\parallel} is the average value of the in-plane thermal conductivity; \bar{x}_{\perp} is the average value of the through-plane thermal conductivity; SE is standard error; S is standard deviation; \bar{s}_{\parallel} is standard deviation of the in-plane thermal conductivity data; \bar{s}_{\perp} is standard deviation of the through-plane thermal conductivity data; n is the number of samples. In this case, n=3. Using a t-distribution table or statistical software with degrees of freedom equal to 4, we can get the P-value. When the P-value is less than 0.05, there is a significant difference between the two groups of data. The statistical analysis of the in-plane and through-plane thermal conductivity data for EBN shows a P-value which is less than 0.05. Therefore, it can be concluded that there is a significant difference between these two sets of data, indicating that the in-plane thermal

conductivity of EBN is significantly higher than the through-plane thermal conductivity. The same applies to EBNSiC_2L composite. However, for ESiC and EBNSiC_R, the P-value for the statistical analysis of their in-plane and through-plane thermal conductivity data is greater than 0.05, indicating that there is no significant difference in their in-plane and through-plane thermal conductivities.

It is worth noting that the sample EBNSiC_2L with two layered structure achieves the highest in-plane thermal conductivity ($2.16 \text{ W m}^{-1} \text{ K}^{-1}$) with 15.5 vol% loading of total fillers. The improved in-plane thermal conductivity of these layered composites is ascribed to the orientation of BN platelets and SiC whiskers aligned with the direction of heat flow. This arrangement allows the better in-plane heat conducting characteristics of BN platelets and SiC whiskers to be fully utilized, resulting in improved thermal conductivity. Therefore, due to the random distribution of fillers in the EBNSiC_R sample, its in-plane and through-plane thermal conductivities show minimal difference.

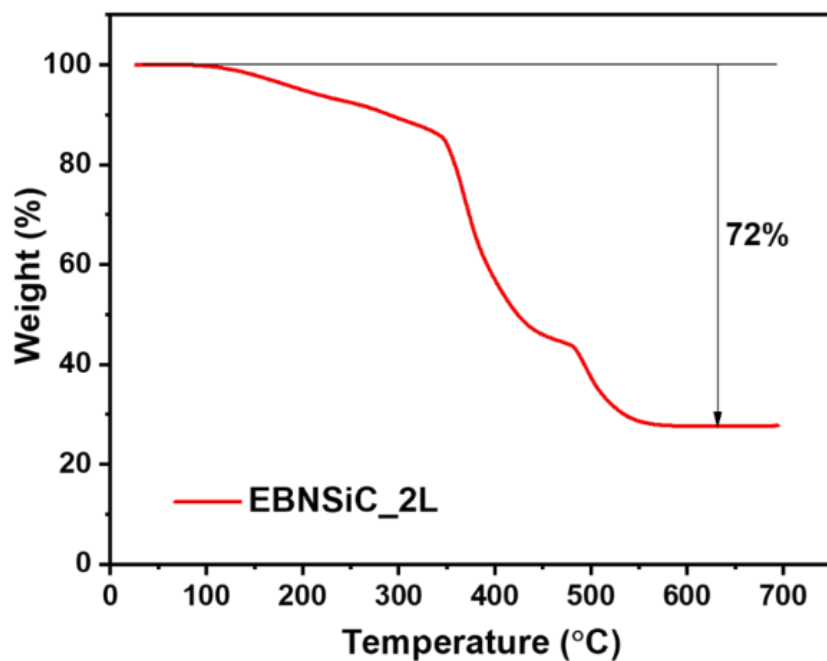


Figure 5.4 TGA curve of Epoxy/BN/SiC layered composite from room temperature to 700 °C.

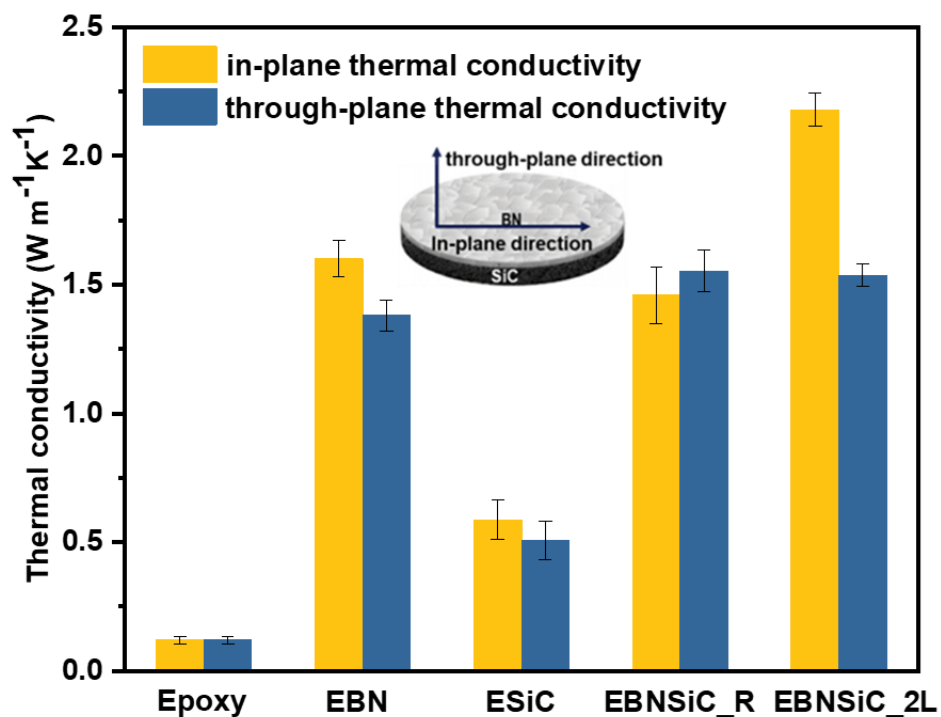


Figure 5.5 In-plane and through-plane thermal conductivity of pure epoxy resin, EBN, ESiC, EBNSiC_R and EBNSiC_2L composites.

Table 5.1 Thermal conductivity (K) data for three samples of the same materials, including the average value, standard deviation (S). Standard error (SE), t-value and P-value of the two groups data (in-plane and through-plane thermal conductivity) calculated by statistical methods.

	K1 (W m ⁻¹ K ⁻¹)	K2 (W m ⁻¹ K ⁻¹)	K3 (W m ⁻¹ K ⁻¹)	Average K (\bar{x}) (W m ⁻¹ K ⁻¹)	S (W m ⁻¹ K ⁻¹)	SE	t	P
Epoxy	0.11	0.12	0.14	0.123	0.015	-	-	-
EBN In-plane	1.53	1.61	1.67	1.603	0.070			
EBN Through- plane	1.41	1.31	1.42	1.380	0.061	0.054	4.163	P < 0.05
ESiC In-plane	0.50	0.64	0.62	0.587	0.076			
ESiC Through- plane	0.58	0.43	0.51	0.506	0.075	0.062	1.30	P > 0.05
EBNSiC_R In-plane	1.53	1.33	1.52	1.460	0.11			
EBNSiC_R Through- plane	1.53	1.58	1.55	1.553	0.080	0.080	1.40	P > 0.05
EBNSiC_2L In-plane	2.18	2.08	2.06	2.107	0.064			
EBNSiC_2L Through- plane	1.54	1.49	1.58	1.537	0.045	0.045	12.57	P < 0.001

Because poor dimensional stability can negatively impact the dependability of the devices, polymer composites' dimensional stability has become an essential factor for their reliable usage in electronic devices. The CTE value is indicative of the dimensional stability and is evaluated by thermomechanical analysis (TMA) within the temperature range of room temperature to 100 °C. The CTE values and

dimensional change of the pure epoxy and all composites in through-plane direction are shown in Figure 5.6. The maximum CTE is found in pure epoxy resin (92 ppm K^{-1}), and the CTE values of all composites are decrease after adding fillers. For example, the SiC layered composite (ESiC) has the lowest CTE which is only 31 ppm K^{-1} . This result implies that the SiC filler is more capable of reducing CTE in through-plane direction than BN fillers, because CTE (38 ppm K^{-1}) of BN in through-plane direction is much higher than that of SiC (5 ppm K^{-1}) [132, 193, 205]. The value of CTE for EBNSiC_2L layered composite falls within the ranges of CTE for EBN and ESiC composites because it combines both BN layer and SiC layer. The suppression of volume change in the layered structure between BN and SiC and epoxy in the interstitial region is responsible for the composite's lower CTE [118]. Another possible reason was that the epoxy molecular chains were constrained in the layered composites so that their motion ability was limited. The results suggest that the EBNSiC_2L layered composite exhibited better dimension stability compared with pure epoxy.

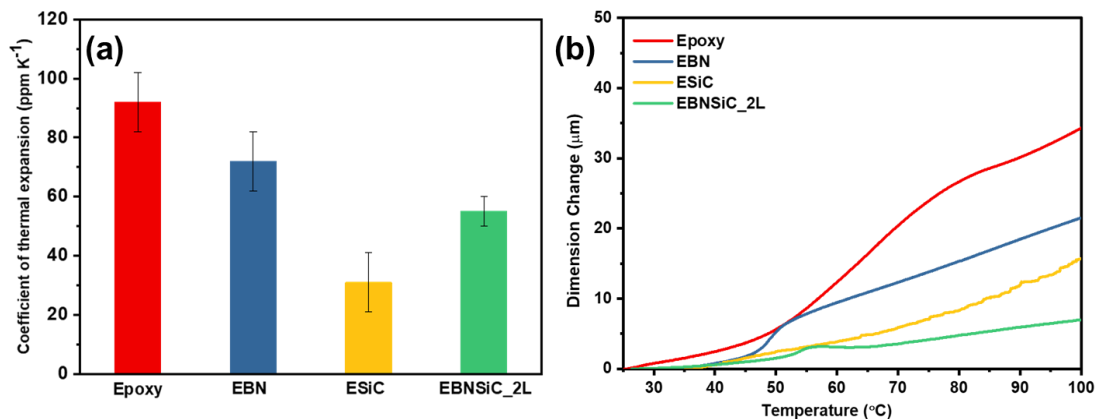


Figure 5.6 (a) The coefficient of thermal expansion of pure epoxy resin, EBN, ESiC and EBNSiC_2L composites; (b) Dimensional change as a function of operating temperature of the pure epoxy, EBN, ESiC and EBNSiC_2L.

5.4 Dielectric properties of Epoxy/BN/SiC bi-layered composite

The dielectric permittivity of a material is a measure of its ability to store electric charge in an external electric field and reflects the material's dielectric properties. Figure 5.7a shows the frequency-dependence of the dielectric constant and dissipation factor of pure epoxy resin and different kinds of composites at room temperature. Their dielectric constants exhibited a very low frequency-dependence, which slightly decreased with the frequency from 10^2 - 10^6 Hz. The detailed data is shown in Figure 5.8. The interfacial polarization and orientation polarization of dipoles were unable to keep pace with the high frequency change, which accounts for the decrease of the dielectric constant [147, 206, 207]. The dielectric behaviour at low frequencies mirrors the characteristic interface polarization, originating from the macroscopic interfaces among various multiphase structures. On the other hand, at high frequencies, the dielectric behaviour is attributed to the polarization caused by dipole orientation within the composites, in line with Debye relaxation theory [38]. The dielectric constant of pure epoxy resin was 4.99 under the frequency of 1kHz, and the addition of BN and SiC caused an increase in the overall level of the dielectric constant compared with pure epoxy at room temperature. The EBNSiC_2L bi-layered composites has the highest dielectric constant which is 9.03 (1kHz).

Figure 5.7a also displays the dependence of dielectric loss on frequency at room temperature for the composites. It is widely recognized that dielectric loss predominantly consists of conductive loss and polarization loss [140]. At low frequencies, the dissipation factor can attribute to the conductance loss since the material polarization essentially aligns with the gradual shift in the external electric field. Consequently, conductive loss prevails as a result of minimal polarization loss.

As shown in Figure 5.7a, because the polymer is insulated, the dielectric loss of pure epoxy and composites below 10^4 Hz is very low. The dielectric loss for the composites keeps increasing above 10^4 Hz because of polarization loss since dipoles have less time to orient. The dielectric loss increases dramatically over 10^5 Hz because of the relaxation loss caused mainly by segmental movements of the epoxy matrix at high frequencies [208]. The EBNSiC_2L bi-layered composite has same dielectric loss ($\tan\delta$ 0.015) at 1kHz with epoxy.

Figure 5.7b-c show the dielectric constant and dielectric loss of the pure epoxy and composites at different temperature in the 10^2 - 10^6 Hz frequency range. Both dielectric constant and dielectric loss increased with the temperature, which suggests that the temperature plays a key role in determining the dielectric property of the composites. The higher temperature allows the dipoles to have enough mobility to contribute to the loss and dielectric constant because of the increased segmental mobility of polymer [209]. All the samples have highest dielectric constant and dielectric loss at 100 °C under low frequency. As the frequency increases, the dielectric constant and dielectric loss both decrease gradually. At low frequencies, the conductance loss is dominant, and the high temperature prompt the charge carrier transport in composites leading to a high dielectric loss [138].

The EBNSiC_2L bi-layered composites exhibited a higher and relatively stable dielectric constant and a low level of dielectric loss in the 10^2 - 10^6 Hz frequency range, which satisfy the requirement for a high dielectric constant but low loss value in practical engineering applications.

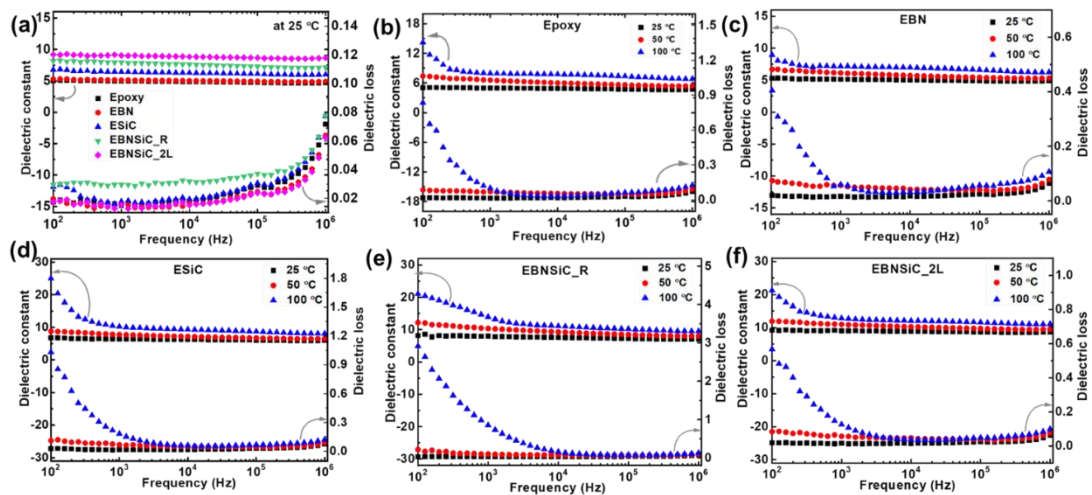


Figure 5.7 (a) Dielectric constant and dielectric loss dependence on frequency for pure epoxy and composites at room temperature; Dielectric constant and dielectric loss dependence on frequency at different temperature for (b) Epoxy, (c) EBN, (d) ESiC, (e) EBNSiC_R, (f) EBNSiC_2L.

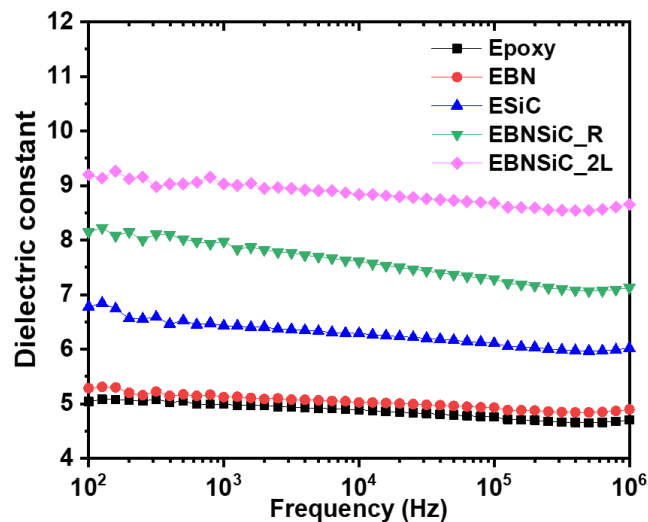


Figure 5.8 Dielectric constant dependence on frequency for pure epoxy and composites at room temperature.

The breakdown strength is also a key parameter in practical applications. The characteristic breakdown strength (E_b) of epoxy, EBNSiC_R and EBNSiC_2L composites is deduced from a two parameter Weibull distribution as shown in Figure 5.9a. The equation is given as followed,

$$P(E) = 1 - \exp\left[-\left(\frac{E}{E_b}\right)^\beta\right] \quad \text{Equation 5.4}$$

where $P(E)$ is the cumulative probability of electrical breakdown, E is the measured experimental breakdown strength, E_b is the characteristic breakdown strength at the cumulative breakdown probability of 63.2% for materials, and β is the Weibull modulus related to the linear regressive fit of the distribution. Thus, E_b can be calculated by converting the function to:

$$\ln\left(\ln\left(\frac{1}{1-P}\right)\right) = \beta \ln\left(\frac{E}{E_b}\right) \quad \text{Equation 5.5}$$

The breakdown strength of pure epoxy resin is $\sim 23 \text{ kV mm}^{-1}$, and the breakdown strength of randomly mixed BN and SiC composites (EBNSiC_R) is slightly higher than that of pure epoxy resin. This is because the randomly scattered fillers in the polymer do not form conductive pathways and hinder the growth of electrical trees to some extent under applied external electric field. However, the breakdown strength of EBNSiC_2L is slightly lower than that of epoxy and EBNSiC_R, which is 20 kV mm^{-1} . The reason for this is that the fillers in it are ordered in a layer that facilitates the formation of a pathway for the growth of the electric tree, as shown in Figure 5.9b-d, the EBNSiC_2L layered composite forms a greater breakdown damage.

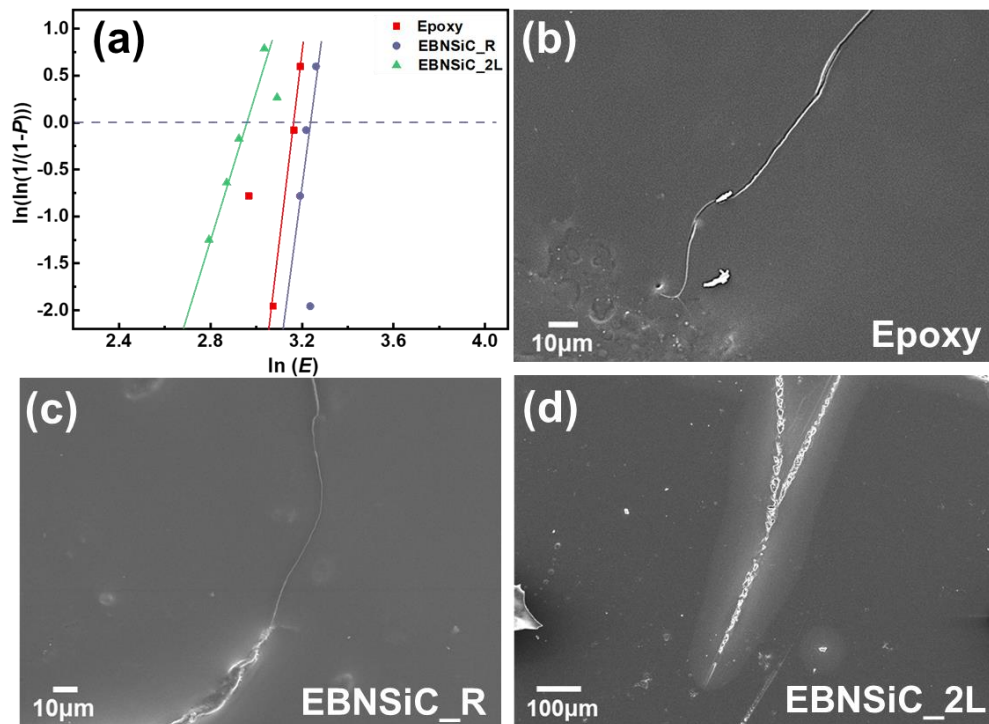


Figure 5.9 (a) Weibull distribution of breakdown strength of pure epoxy resin and composites; SEM images of (b) epoxy; (c) EBNSiC_R composites; (d) EBNSiC_2L composites after breakdown.

5.5 Electrical properties of Epoxy/BN/SiC bi-layered composite

The good electrical insulation also plays an important role in the application of the composites. Because the addition of the BN and SiC probably influence their insulating properties, the volume resistivity of BN and SiC epoxy resin composites were measured, as shown in Figure 5.10. The volume resistance of pure epoxy resin is $1.5 \times 10^{10} \Omega \text{ cm}$, after adding the fillers, the volume resistance of the composites is slightly lower than that of pure epoxy, but it still meeting the required resistance standard for electrical insulation applications ($10^9 \Omega \text{ cm}$).

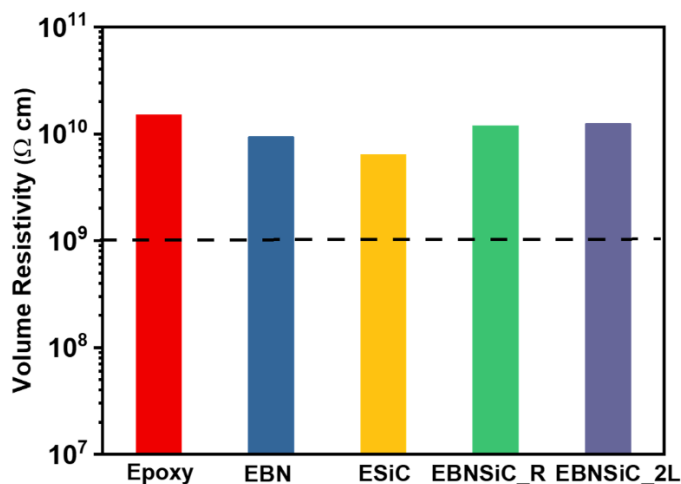


Figure 5.10 Electrical resistivities of epoxy and composites.

5.6 Discussion

XRD results (Figure 5.3) and SEM results (Figure 5.2) confirmed that the BN platelets were aligned in the horizontal direction by vacuum force. Meanwhile, SEM results of Epoxy/BN/SiC bi-layered composite demonstrate the interfaces between the two layers are seamlessly integrated, with no observable voids or defects within the composites. Because thermal conduction pathways and tightly bonded interfaces have been established in the in-plane direction, Epoxy/BN/SiC bi-layered composite (EBNSiC_2L) with two layered structure achieves the highest in-plane thermal conductivity ($2.16 \text{ W m}^{-1} \text{ K}^{-1}$) (Figure 5.5). These results correlate well with the findings by Chen et al. and Tarhini et al., who reported similar improvements in in-plane thermal conductivity by aligning fillers horizontally using various alignment techniques [210, 211]. The high in-plane thermal conductivity can be attributed to the efficient heat transfer pathways formed by the aligned BN platelets and SiC whiskers, enhancing the composite's overall thermal performance.

The thermal conductivity comparison results show that the through-plane thermal conductivities of EBN, EBNSiC_R, and EBNSiC_2L are similar. This similarity arises because, at the same volume filler loading, the number of vertical thermal conduction

pathways is nearly the same. In contrast, ESiC has the lowest thermal conductivity because the thermal conductivity of SiC itself is lower than that of BN. Additionally, SiC fibres are 1D materials, resulting in smaller contact areas between fibres. However, by using hybrid fillers, even though SiC is also used in EBNSiC_R and EBNSiC_2L, their thermal conductivities remain close to that of pure EBN. The advantages of selecting SiC as a filler are manifested in its role in reducing the CTE, with ESiC having the lowest CTE at only 31 ppm K^{-1} . The low CTE of ESiC also suppresses the thermal expansion of the bi-layered EBNSiC_2L, thus the CTE of the EBNSiC_2L is 55 ppm K^{-1} , which is 10 ppm K^{-1} lower than that of pure EBN (Figure 5.5b). This finding aligns with studies by Shen et al. who demonstrated that incorporating SiC fibres can significantly lower the CTE of polymer composites [36].

The synergistic effect of the Epoxy/BN/SiC bi-layered composite in enhancing thermal conductivity and decreasing dielectric loss is demonstrated in this study. Generally, to achieve the target thermal conductivity, fillers are added into polymer to form continuous heat transfer pathways. But these fillers in composites are generally increase the dielectric loss and dramatically decreased breakdown strength. Table 5.2 shows the thermal conductivity and dielectric properties of various polymer composites. The breakdown strength of all composites decreased after adding the fillers in matrix. For example, the breakdown strength of Al/Epoxy resin composite even decreased from 31.2 to 6 kV mm^{-1} . In this work, the breakdown strength of EBNSiC_2L only decreased from 23 to 20 kV mm^{-1} . The reason for the less decrease is the region of electric field which is formed around the interface between two different layers in the bi-layered composite [148].

Regarding the dielectric constant, it also increases from 4.99 to 9.03 . This would be explained that the fillers have inherently higher dielectric constant and the different of

electrical conductivity between the fillers and epoxy resin generates the interfacial polarization, which increases the dielectric constant. It is worth noting that the dielectric constant of single-layered SiC composite (ESiC) is higher than that of single-layered BN composite (EBN). The reason is that SiC whiskers have a higher aspect ratio than BN platelets, and the large dipole moments of the high aspect ratio filler results in a higher dielectric enhancement of composites at lower loading [212, 213].

In addition, the dielectric constant of the randomly mixed composite (EBNSiC_R) is higher than the dielectric constant of the layered composite with only one filler. In EBNSiC_R composite, the mismatch of electrical conductivities between the epoxy matrix, BN and SiC enabled lots of space charges to migrate and accumulate at the interfaces and bring stronger interfacial polarization [214]. For EBNSiC_2L, BN and SiC are aligned and in contact or very close to each other. The average polarization associated with the contacted fillers is larger than that of an individual particle because of an increase in the dimensions of the fillers linked together leads to greater average polarization and thus a greater contribution to dielectric constant [206]. Additionally, interfacial polarization also occurs at the interface between the BN layer and SiC layer, which results in the increase of dielectric constants. Thus EBNSiC_2L bi-layered composite has the highest dielectric constant which is 9.03 (1kHz).

Regarding dielectric loss, compared with epoxy matrix, the dielectric loss of EBNSiC_2L bi-layered composite has no change. The layered structure could inhibit the movement of the charge carriers within epoxy, leading to a lower dissipation factor value. The low dielectric loss is beneficial to small leakage current and low energy loss. However, Table 5.2 shows almost all dielectric loss of composites increased after adding fillers. Thus, by designing a bilayer structure, the composite manages to

increase the dielectric constant while still enhancing thermal conductivity, maintaining dielectric loss and breakdown strength.

When compared to other layered dielectric thermal conductivity composites, the EBNSiC_2L composite shows notable improvements. For instance, Wang et al. demonstrated a three-layer composite film of Al₂O₃ with an in-plane thermal conductivity of 0.532 W m⁻¹ K⁻¹, which is much lower than the 2.16 W m⁻¹ K⁻¹ achieved by EBNSiC_2L [148]. However, Wang et al.'s composite showed a higher breakdown strength (73.79 kV mm⁻¹) due to the sandwich structure and high breakdown strength of epoxy matrix (64.45 kV mm⁻¹) [148]. In terms of dielectric properties, the EBNSiC_2L's dielectric constant of 9.03 is higher than that of many single-filler systems reported in the literature (Table 5.2), such as the BN/epoxy composites reported by Huang et al., which had a dielectric constant of 3.91 [145]. The low dielectric loss of EBNSiC_2L also compares favourably with other same filler composites, such as the hybrid BN/SiC composites reported by Sima et al., which showed a lower dielectric constant (6, 1kHz) but with a higher dielectric loss (0.02, 1kHz) [215].

Doctor-blading and hot-pressing methods are also used to increase in-plane thermal conductivity. Doctor-blading, as used by Jang et al., has shown to align BN sheets effectively, achieving in-plane thermal conductivities of up to 2.4 W m⁻¹ K⁻¹ [216]. However, this method requires precise control over the process and uniformity of the film thickness, but it is suitable for large-area preparation. A flexible BNNS-PVDF film was also prepared by doctor-blading process, and the in-plane thermal conductivity of this film reach 7 W m⁻¹ K⁻¹ [217]. However, the through-plane thermal conductivity of the BNNS-PVDF film is only 0.3 W m⁻¹ K⁻¹. Our EBNSiC_2L composite achieved an increase in the in-plane thermal conductivity along with an

increase in the through-plane thermal conductivity ($1.5 \text{ W m}^{-1} \text{ K}^{-1}$). Hot pressing, reported by Liu et al., achieved an in-plane thermal conductivity of $3 \text{ W m}^{-1} \text{ K}^{-1}$ in a BN/epoxy composite, but the high pressure and temperature involved in the process can limit its applicability to sensitive materials [218]. In comparison to other studies, our results demonstrate a more balanced approach to enhancing both thermal and dielectric properties without significantly compromising the breakdown strength of the composite.

Compared with the commercial FR4 substrate, which typically has a thermal conductivity of around $0.3\text{-}0.4 \text{ W m}^{-1} \text{ K}^{-1}$ and a dielectric constant of approximately 4.5, the EBNSiC_2L composite significantly outperforms FR4 in terms of thermal conductivity and dielectric constant while maintaining comparable breakdown strength. Furthermore, FR4 typically exhibits a CTE of around $60\text{-}70 \text{ ppm K}^{-1}$ in the through-plane direction, which is significantly higher than the CTE of EBNSiC_2L [187, 188]. The breakdown strength of FR4 is generally around 5 kV mm^{-1} , which is much lower than that of EBNSiC_2L, and the EBNSiC_2L also offers enhanced thermal performance and lower dielectric loss [219, 220]. This is particularly advantageous for applications requiring materials with high thermal conductivity and low dielectric loss, such as in advanced electronic packaging and thermal management systems. The ability of EBNSiC_2L to offer both high thermal conductivity and low dielectric loss while maintaining structural integrity and breakdown strength presents a significant improvement over traditional FR4 materials used in PCBs.

While the outcomes of this study offer significant advancements over traditional materials like FR4 and other layered composites reported in the literature, it is essential to consider the potential disadvantages. One potential drawback is the complexity of producing the bi-layered structure, which might increase manufacturing costs

compared to more straightforward filler incorporation methods used in FR4. Additionally, while EBNSiC_2L exhibits superior thermal and dielectric properties, the integration of such materials into existing manufacturing processes could pose challenges. The need for precise alignment and layering techniques might limit large-scale production feasibility and increase costs. Furthermore, while our study shows promising results under laboratory conditions, the long-term reliability and performance under various environmental conditions, such as humidity, temperature cycling, and mechanical stress, still need further investigation to ensure they meet all application requirements.

Table 5.2 Comparison of thermal conductivity, dielectric constant, dielectric loss and breakdown strength of our EBNSiC_2L composite with various polymer in the open literature.

Matrix	Filler	loading (vol%)	Thermal conductivity (W m ⁻¹ K ⁻¹)	Dielectric constant	Dielectric loss	Breakdown strength (kV mm ⁻¹)	Reference
Silicone	BaTiO ₃ fibres	0	-	3.02	0.001	31.5	[221]
		20 vol%	-	8.33	~0.005	19.1	
Epoxy	Al	0	0.2	5	0.009	31.2	[209]
		48 vol%	1.25	34	0.010	6	
Epoxy	BNNF	0	0.15	~3.4	-	115.8	[146]
		2 wt%	0.205	~3.55	-	113.5	
Epoxy	Si/SiO ₂	0	0.17	~3	0.01	-	[147]
		25.5 vol%	0.65	~16	0.11	-	
Epoxy	h-BN-PGMA	0	0.2	~3.9	~0.03	-	[222]
		15 vol%	1.198	4.93	~0.068	-	
Epoxy	BN/SiC bilayer	0	0.12	4.99	0.015	23	This work
		15.5 vol%	2.16	9.03	0.015	20	

5.7 Summary

The bi-layered EBNSiC_2L composite was prepared in order to improve the thermal conductivity and dielectric properties of epoxy composites. The results indicate that EBNSiC_2L increased the through-plane thermal conductivity of epoxy from $0.12 \text{ W m}^{-1} \text{ K}^{-1}$ to $1.54 \text{ W m}^{-1} \text{ K}^{-1}$ and the in-plane thermal conductivity to $2.16 \text{ W m}^{-1} \text{ K}^{-1}$ because of the continue thermal transfer pathway constructed by horizontal aligned BN platelets and SiC whiskers. The EBNSiC_2L also has higher dielectric constant of 9.03 at 1kHz, compared with 4.99 for epoxy at the same frequency. Most importantly, the obtained EBNSiC_2L possessed high thermal conductivity and high dielectric constant but low dielectric loss at the measured frequency range. The dielectric loss of EBNSiC_2L bi-layered composite is only 0.015 at 1kHz. Additionally, the EBNSiC_2L composite exhibits the stability of dielectric properties at the frequency higher than 1 kHz. Even though there is a slight drop in breakdown strength, it is still maintained at 20 kV m^{-1} . At same time, the EBNSiC_2L composite has low CTE value which is 55 ppm K^{-1} . The improvements in thermal and dielectric properties of the composites indicate promising prospects for future engineering applications.

Chapter 6 Enhanced through-plane thermal conductivity of BN and GO epoxy composites by vacuum-assisted filtration

In this chapter, the vertically aligned BN-GO composites were fabricated by vacuum-assisted filtration and followed by slicing up. The vertically aligned structure was characterised by XRD and SEM. Furthermore, the compressive test was carried out to demonstrate the strength of BN-GO slices and the function of GO. The thermal conductivity and CTE of the BN-GO composites with different percentage of GO have been investigated in this research. For further increase the thermal conductivity of BN-GO composites, the 70 nm BNNS were added into epoxy resin before infiltration. This research proposes a novel simple procedure to prepare vertically aligned fillers in composites by vacuum-assisted filtration method to improve the through-plane thermal conductivity of composites.

6.1 Characterisation of BN-GO slices

The BN-GO slices were prepared by vacuum-assisted filtration methods as illustrated in Section 1.1 and Figure 3.3. SEM was used to characterise the sizes and morphology of micro size and nano size h-BN platelets used in this study. As shown in Figure 6.1, h-BN revealed flaky and smooth morphology with average size of 0.5 μm and 70 nm. Referencing the SEM images provided by the supplier, the lateral dimensions of GO is over 5 micrometres [223]. XRD was also used to characterise the as-received h-BN and GO. As shown in Figure 6.1c, pristine h-BN displayed a well-crystallized hexagonal structure. The peaks at approximately 26.8°, 41.6°, 50.2° and 55.1° are assigned to the (002), (100), (102) and (004) crystallographic planes of h-BN, respectively. The XRD pattern of GO reveals a peak at 10.7°, which corresponds to

the (002) plane, indicating the presence of a significant number of oxygenated functional groups on the graphite planes. XRD analysis did not detect any impurity phases, confirming the high purity of the raw h-BN powder and GO.

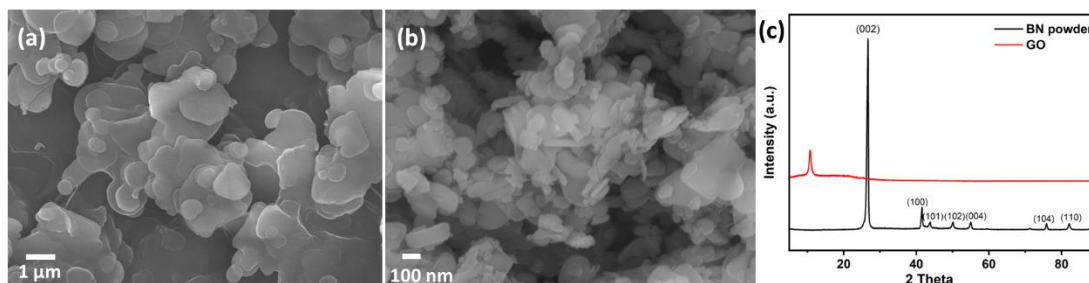


Figure 6.1 SEM images of h-BN powder with size of (a) 0.5 μm , (b) 70 nm; (c) XRD pattern of h-BN powder and GO.

During the preparation process, the BN platelets and GO with extremely high aspect ratio in the solvent preferentially orient parallel to the sample surface after vacuum-assisted filtration due to gravitational forces. The h-BN and GO dispersions underwent the vacuum-assisted filtration, resulting in the assembly of h-BN into a closely packed and horizontally aligned bulk. After the obtained BN-GO “cake” was cut up lengthways, the slices flipped 90° followed by spreading out on the plate, and the flipping process made the horizontally oriented BN and GO changing to vertical oriented direction. Hence, a significant portion of h-BN and GO sheets is expected to align in the through-direction (vertical direction) of the samples. The XRD detection of BN-GO slices with different GO weight percentage provide support for the alignment of BN structures. The characteristic peaks that represent the planes of hexagonal BN are also observed in XRD of BN-GO slices. The horizontally and vertically aligned h-BN are responsible for the reflection from (002) and (100) plane respectively, which is indicated in the inset of Figure 6.2. The intensity ratio of (002) peak and (100) peak represents the orientation degree of h-BN platelets. As shown in

Table 6.1, the relative intensity ratio of the I(100)/I(002) of the BN-GO5 slices is more than four times higher than that of BN powder, which indicates the number of vertical plane h-BN significantly increased. To further study the orientation of h-BN platelets, texture coefficients (Tc) for h-BN powder and BN-GO slices were also calculated and shown in Table 6.1. The Tc associated with the plane defined by the Miller indices (hkl) for n (where n represents the calculated number of peaks, here equalling 3) suggests a favoured alignment along a specific plane [224]. For BN platelets, as observed in the inset of Figure 6.2, the crystalline structure exhibited a preferential orientation along the (002) plane, with a Tc(002) value of 2.57. This value gradually decreased to 1.55 in aligned BN-GO5 slice with the increase of GO content, indicating a shift in the preferred orientation towards the (100) plane as Tc(100) increased from 0.31 to 0.90.

Table 6.1 The intensity of peak (002), (100) and (102); the relative intensity of (100) and (002) peaks; text coefficient of peak (002) and (100) for pure h-BN powder and aligned BN-GO slices.

	I(002)	I(100)	I(102)	I(100)/I(002)%	Tc(002)	Tc(100)
h-BN powder	977.47	120.00	44.18	12.27%	2.57	0.31
BN-GO1	1162.8	177.03	85.11	15.22%	2.44	0.37
BN-GO3	261.93	152.43	57.25	58.19%	1.67	0.97
BN-GO5	38.84	22.61	13.58	58.21%	1.55	0.90
BN-GO7	532.98	113.97	49.78	21.38%	2.29	0.49

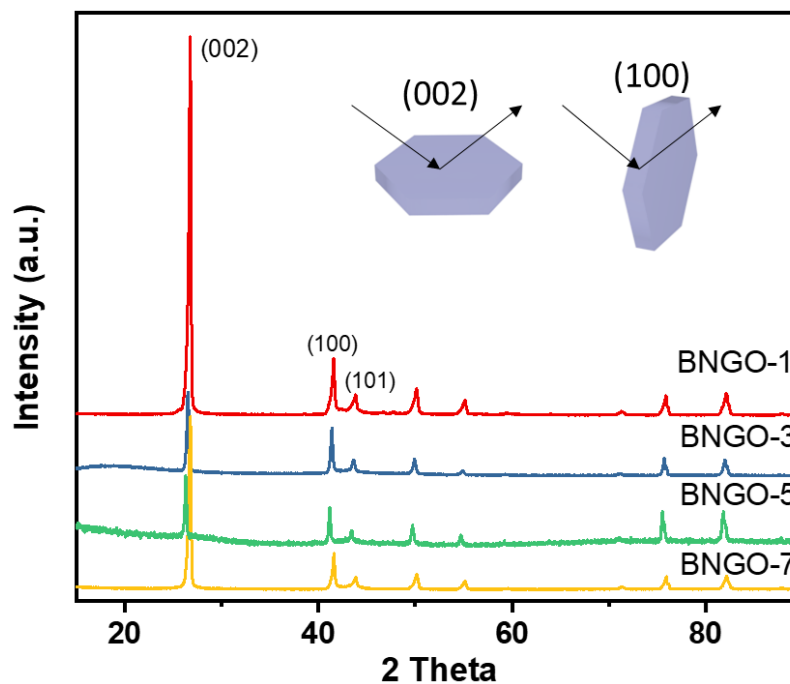


Figure 6.2 XRD pattern of aligned BN-GO slices. Inset shows the illustration of the effect of BN orientation on the XRD pattern.

SEM was performed to study the vertically aligned structure of BN-GO slides. Figure 6.3a shows the surface morphology of BN-GO3 slice from the top-view. From Figure 6.3b and c, it can be observed that GO is a thin layer that wraps and connects the BN platelets. The energy-dispersive X-ray spectroscopy (EDS) was performed on the surface of the BN-GO3 (Figure 6.3c). The results of EDS show uniform dissociation of constituent elements B, C and O, indicating that GO sheets were distributed in the aligned BN-GO slice. As revealed by the cross-section SEM images of BN-GO slides (Figure 6.4), 2D h-BN platelets and GO sheets are assembled into the directional alignment, where BN platelets are densely cross-linked by GO. In the cross-sectional SEM images of the BN-GO5 sample, a distinct layered aligned structure is observed in Figure 6.4a. Upon magnification, it can be observed that GO is interconnecting with BN (Figure 6.4b). Similarly, in the BN-GO7 sample, a similar layered aligned structure is observed (Figure 6.4c), and upon further magnification, it can be observed that

almost all of the BN within the sample cross-section is covered by GO (Figure 6.4d).

The cross-sectional SEM images of the BN-GO slices reveal their dense structure.

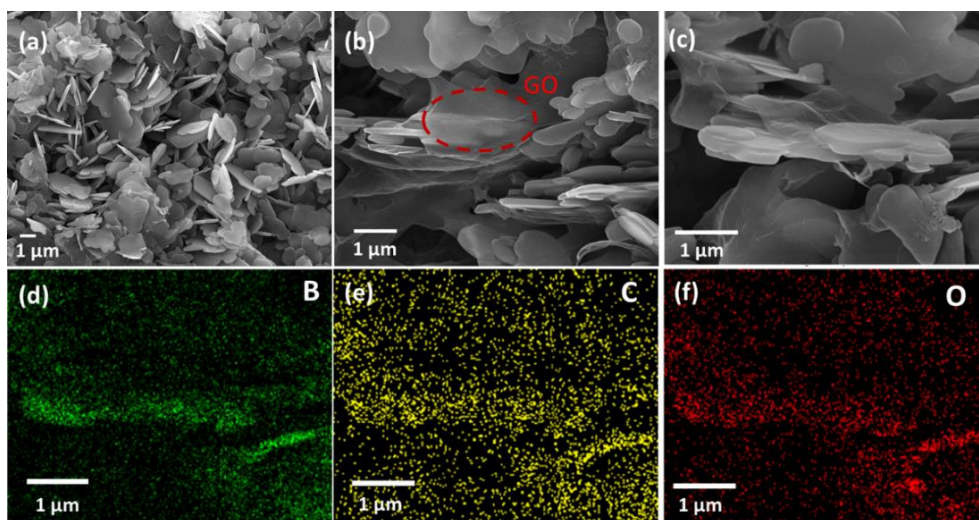


Figure 6.3 (a) (b) (c) SEM images of the surface of aligned BN-GO3 slice with different magnification; (d) (e) (f) Elemental mapping collect from (c).

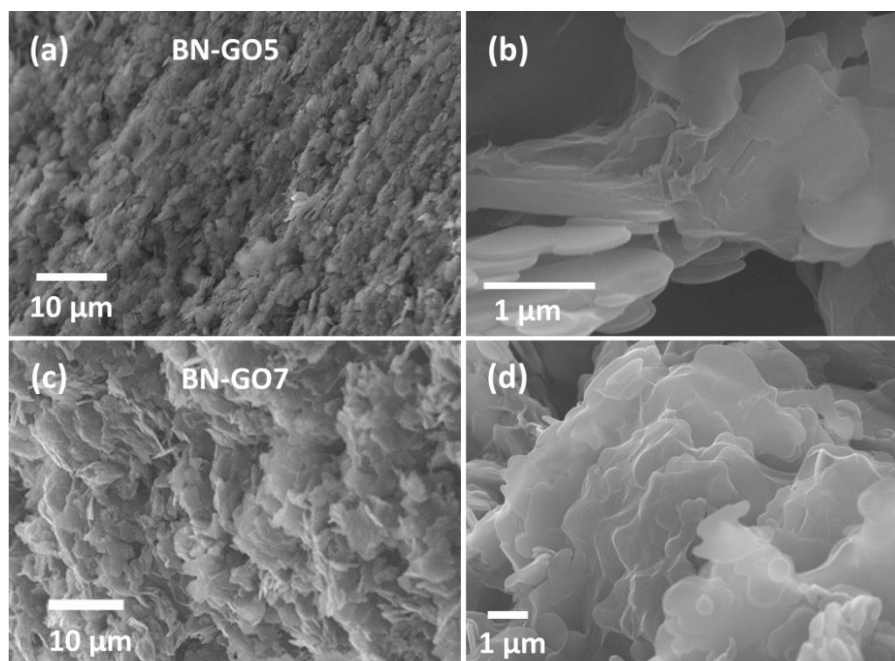


Figure 6.4 SEM images of the cross-section of (a) (b) BN-GO5; (c)(d) BN-GO7.

The dense structure imparts strong mechanical strength to the BN-GO slices. To evaluate the mechanical strength of the BN-GO slices, BN slices and BN-GO slices prepared using the same method were subjected to compression tests. The compressive

strain-stress curves are shown in the Figure 6.5. Figure 6.5b represents the compressive strain-stress of pure BN slice. The sudden drop in the curve indicates that the sample was crushed by the press machine. Pure BN slice can only withstand a maximum pressure of only 0.00075 MPa, whereas BN-GO5 can withstand a maximum pressure of 2.5 MPa, which is over 3000 times the compressive strength of pure BN slice. Pure BN slice is particularly fragile, collapsing and breaking under minimal pressure. The crushed BN slice was isolated as BN powder, while the crushed BN-GO remained compacted, with the loose small pieces of BN-GO. The high strength of BN-GO is attributed to the presence of GO. High mechanical strength is beneficial for maintaining their alignment structure during epoxy resin infiltration.

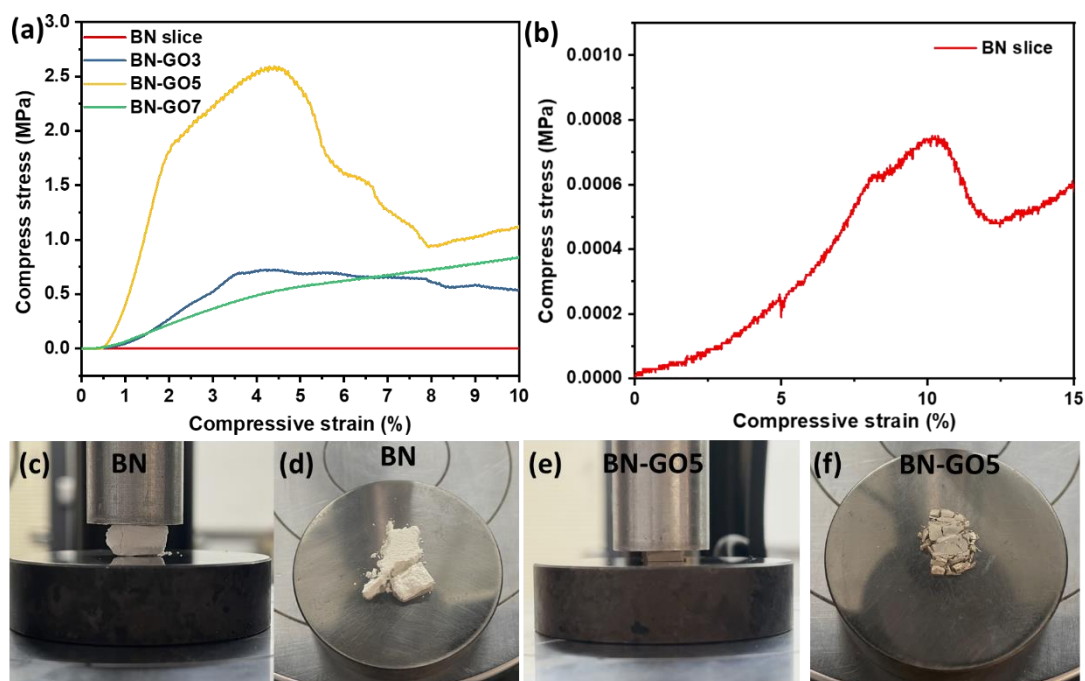


Figure 6.5 Compressive stress-strain curves of (a) pure BN and BN-GO slices; (b) pure BN. (c) Photo of BN slice during compression test; (d) Photo of BN slices after compression test; (e) Photo of BN-GO5 during compression test; (f) Photo of BN-GO5 after compression test.

6.2 Characterisation of BN-GO composites

The BN-GO composites were prepared by impregnating BN-GO slices into epoxy resin (Section 1.1 and Figure 3.3). BN-GO composites with different weight percentage of GO were obtained by epoxy resin infiltration. SEM was performed to study the vertically aligned structure of BN-GO composites. As shown in Figure 6.6, the BN-GO5 composites exhibited an aligned structure as well. From the surface of SEM images (Figure 6.6a), there are no pores in the composites, and BN-GO demonstrates strong adhesion to the epoxy, with no evident interfacial debonding observed between them. Moreover, the alignment of BN-GO structure is well maintained in the epoxy resin matrix (Figure 6.6b, c and d). These vertically aligned BN-GO build many heat transfer channels in the through-plane direction. Moreover, due to the highly anisotropic thermal properties of h-BN platelets, the thermal conductivity of the aligned BN-GO composites will be significantly enhanced in the vertical direction.

TGA tests was carried out to get the fillers loading in BN-GO composites. Figure 6.7 shows the TGA curves of BN-GO epoxy composites from room temperature to 700 °C. Three significant drops can be found in the weight loss curve. The initial drop, occurring approximately between 140-350 °C, is attributed to the pyrolysis of low molecular weight components and the removal of oxygen functional groups from graphene oxide (GO). The subsequent drop, observed around 350-500 °C, is associated with the decomposition of epoxy resin. The final stage of weight loss, occurring between 500-620 °C, is attributed to the combustion of residual carbon from the epoxy resin and the oxidative pyrolysis of the carbon framework in an air atmosphere [225]. At this point, all organic compounds have undergone complete decomposition and volatilization. The remaining weight corresponds to the weight of boron nitride (BN)

in the composite. h-BN content could be obtained by the residual weight at 700 °C. The volume loadings of h-BN are approximately 31 vol% in BN-GO1, 26 vol% in BN-GO3 and 23 vol% in BN-GO5. The loading of BN and GO in the composites can be calculated by using the densities of the fillers, samples and epoxy resin. The volume loading of BN and GO is 43 vol% in BN-GO1, 42 vol% in BN-GO3 and 42 vol% in BN-GO5. Therefore, the volume loading of the BN and GO in composites is probably around 42 vol%. The data used in the calculations are shown in Table 6.2 and Table 6.3. Additionally, the TGA results also indicate that the polymer remains stable under conditions up to 100 °C, which meets the thermal stability requirements for electronic device applications.

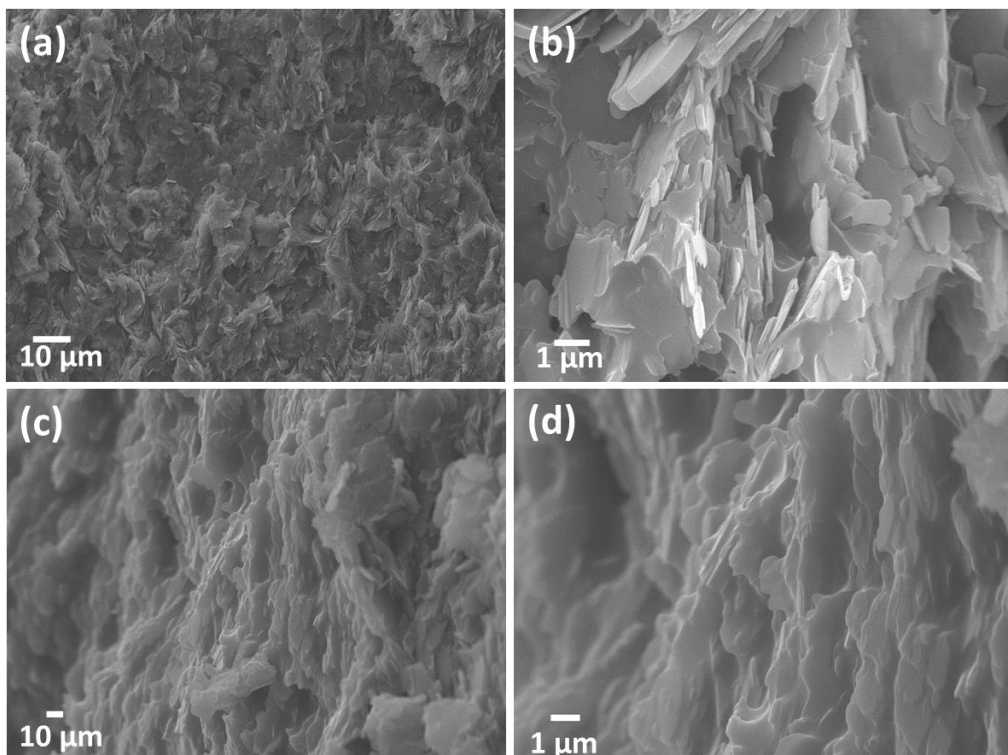


Figure 6.6 SEM images of (a) the top surface of BN-GO5 composites, (b) (c) (d) the fracture surface cross-section of BN-GO5 composites.

Table 6.2 The weight loss of samples at 700 °C, the original samples weight, weight of epoxy and GO in samples, weight of BN, weight of GO, the weight of epoxy in samples.

Sample	Weight loss (mg)	Weight (mg)	Weight (epoxy+GO) (mg)	Weight (BN) (mg)	Weight (GO) (mg)	Weight (epoxy) (mg)
BN-GO1	1.617	3.491	1.617	1.874	0.0189	1.5981
BN-GO3	5.132	9.538	5.132	4.406	0.136	4.9960
BN-GO5	2.050	3.692	2.050	1.642	0.0864	1.9656

Table 6.3 The density of samples (ρ), volume of epoxy in samples (V_{epoxy}), volume of whole samples (V_{sample}), volume of BN in samples (V_{BN}), volume loading of BN in samples ($V_{\text{BN}\%}$), volume of BN and GO in samples ($V_{\text{BN+GO}}$), volume loading of BN and GO in samples ($V_{\text{BN+GO}\%}$).

Sample	ρ (g/cm ³)	V_{epoxy} (cm ³)	V_{sample} (cm ³)	V_{BN} (cm ³)	$V_{\text{BN}\%}$ (vol%)	$V_{\text{BN+GO}}$ (cm ³)	$V_{\text{BN+GO}\%}$ (vol%)
BN-GO1	1.374	0.00138	0.00254	0.000818	32	0.0011	43
BN-GO3	1.274	0.0043	0.00749	0.00192	26	0.00319	42
BN-GO5	1.270	0.00169	0.00291	0.000717	25	0.00122	42

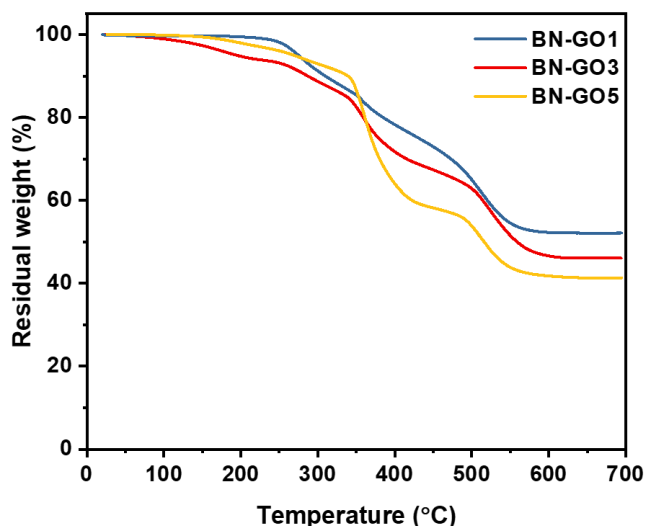


Figure 6.7 TGA curves of the BN-GO1, BN-GO3 and BN-GO5 composites.

6.3 Thermal properties of BN-GO composites

Figure 6.8 summarize the through-plane thermal conductivities of BN-GO epoxy composites with various GO weight percentage. To prove the effectiveness of GO, the pure BN composite was also prepared by the same methods. The data for calculating the thermal conductivities is shown in Table 6.4. At room temperature, pure epoxy resin exhibits a thermal conductivity of $0.12 \text{ W m}^{-1} \text{ K}^{-1}$, consistent with earlier research findings. [63, 226]. The existence of aligned BN-GO structure results in a dramatic enhancement of thermal conductivity of the epoxy resin. It can be explained by the orientation of BN micro platelets along the through-plane direction upon filtration and slicing up. The maximum thermal conductivity of $5.51 \text{ W m}^{-1} \text{ K}^{-1}$ in BN-GO-epoxy composites is achieved with 5 wt% GO in BN-GO slice, which is about 46 times higher than that of pure epoxy resin. In the direction oriented by h-BN, a more conductive pathway is established, resulting in a notable enhancement of the composite's thermal conductivity in that specific direction. Furthermore, the densely packed structure established during vacuum-assisted filtration contributed to a reduction in interfacial thermal resistance, thus contributing to the high thermal

conductivity. However, when the weight concentration of GO increases to 7 wt%, the thermal conductivity of BN-GO-epoxy decreases from 5.51 to 4.30 W m⁻¹ K⁻¹.

Table 6.4 The density (ρ), specific heat capacity (C_p) through-plane thermal diffusivities (λ), the calculated thermal conductivities (K) of epoxy resin, BN-epoxy, BN-GO-epoxy composites.

Sample	ρ (g cm ⁻³)	C_p (J g ⁻¹ °C ⁻¹)	λ (mm ² s ⁻¹)	K (W m ⁻¹ K ⁻¹)
Epoxy resin	1.160	0.968	0.108±0.005	0.12±0.01
BN-epoxy	1.293	1.060	1.036±0.010	1.42±0.02
BN-GO1-epoxy	1.374	0.990	1.328±0.006	1.81±0.07
BN-GO3-epoxy	1.274	1.310	2.025±0.016	3.38±0.08
BN-GO5-epoxy	1.270	1.421	3.050±0.020	5.51±0.04
BN-GO7-epoxy	1.281	1.573	2.135±0.019	4.30±0.04

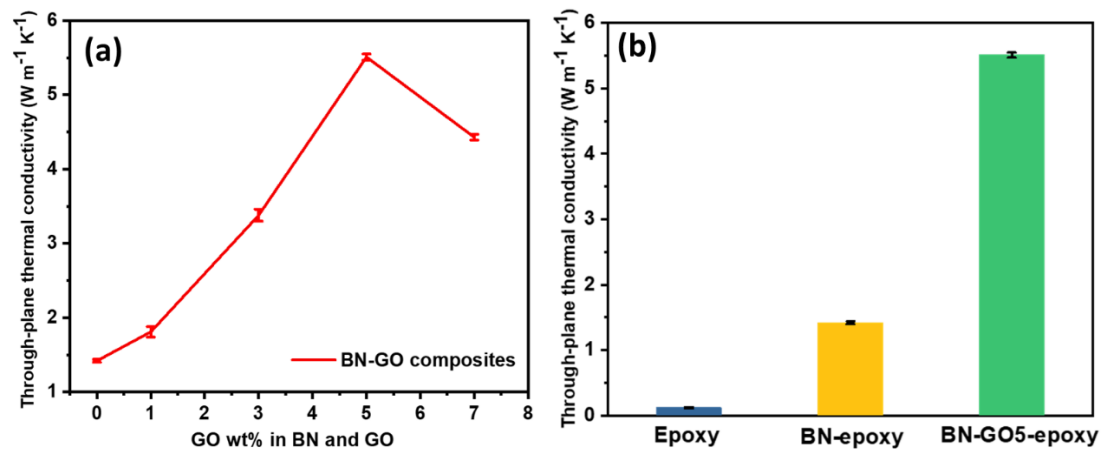


Figure 6.8 (a) Thermal conductivity of aligned BN-GO-epoxy composites with different GO weight percentage in BN-GO slices; (b) Thermal conductivity of pure epoxy resin, BN-epoxy and BN-GO5-epoxy.

Dimensional stability is a crucial property of polymer composites, as any mismatch in dimensional stability between two distinct materials can result in product deformation. The CTE serves as an indicator of the dimensional stability of the composites and can be evaluated through thermomechanical analysis (TMA) within a temperature range from 25 to 100 °C, as shown in Figure 6.9a. The values of CTE are determined in the glassy region. Figure 6.9b shows the values of CTE of the pure epoxy resin, BN composite and BN-GO composites. The CTE value of pure epoxy resin reaches up to 92 ppm K⁻¹. All the CTE value of composites was much lower than that of epoxy resin. BN-GO3-epoxy has the lowest CTE which is only 5 ppm K⁻¹, which matches with the CTE of silicon. The results indicated that the aligned BN-GO composites demonstrated superior dimensional stability in comparison with pure epoxy resin. The higher loading of fillers leads to the low CTE because the fillers have lower CTE than polymer matrix. The presence of aligned BN-GO layered structure constrained the motion of epoxy resin molecular chains, thereby limiting their mobility. Another reason is that the volume change was suppressed within the alternative layered structure between BN-GO and epoxy resin within the interstitial space.

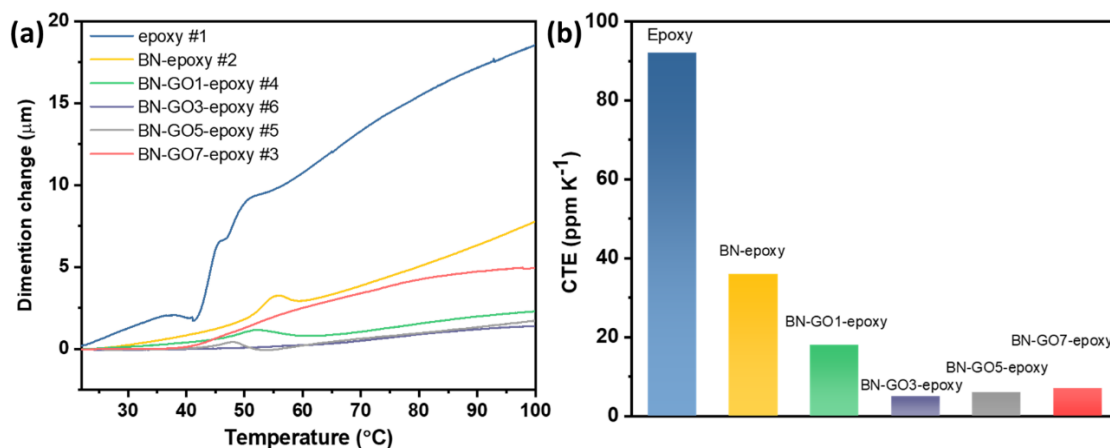


Figure 6.9 (a) Dimension change of pure epoxy resin, BN composites and BN-GO composites with the temperature change; (b) CTE values of pure epoxy resin, BN composites and BN-GO composites.

6.4 Thermal conductivity of BN-GO5-70 composites

In the previous section, BN-GO5 exhibited the highest thermal conductivity ($5.51 \text{ W m}^{-1} \text{ K}^{-1}$). In order to further enhance the thermal conductivity of BN-GO composites, nano-sized BN was added to the epoxy resin before being infiltrated into BN-GO, aiming to increase the contact area between the fillers and thereby enhance the thermal conductivity of the composite. The nano-sized BN added to the epoxy resin has a size of 70 nm, with addition amounts of 5 wt% and 10 wt% relative to the mass of the epoxy resin, respectively. Table 6.5 lists the data for calculating the thermal conductivity of the composites. The densities of BN-GO5-70 composites are higher than the BN-GO5 composites because of the addition of nano BN. BN-GO5-70-5wt% composite achieves highest thermal conductivity which is $6.70 \text{ W m}^{-1} \text{ K}^{-1}$. The high thermal conductivity attributed to the nano size BN platelets fills in the gap between the BN and GO and they connect all the fillers to build the thermal transfer pathways in composites. The results demonstrate that mixing BN in epoxy resin before infiltration is an effective way to improve thermal conductivity of composites.

Table 6.5 The density (ρ), specific heat capacity (C_p) through-plane thermal diffusivities (λ), the calculated thermal conductivities (K) of epoxy resin, BN-epoxy, BN-GO5-epoxy and BN-GO5-70 composites.

Sample	ρ (g cm ⁻³)	C_p (J g ⁻¹ °C ⁻¹)	λ (mm ² s ⁻¹)	K (W m ⁻¹ K ⁻¹)
Epoxy resin	1.160	0.968	0.108±0.005	0.12±0.01
BN-epoxy	1.293	1.060	1.036±0.010	1.42±0.02
BN-GO5-epoxy	1.270	1.421	3.050±0.020	5.51±0.04
BN-GO5-70-5wt%	1.469	1.226	3.722±0.030	6.70±0.05
BN-GO5-70-10wt%	1.540	1.247	2.744±0.013	5.27±0.02

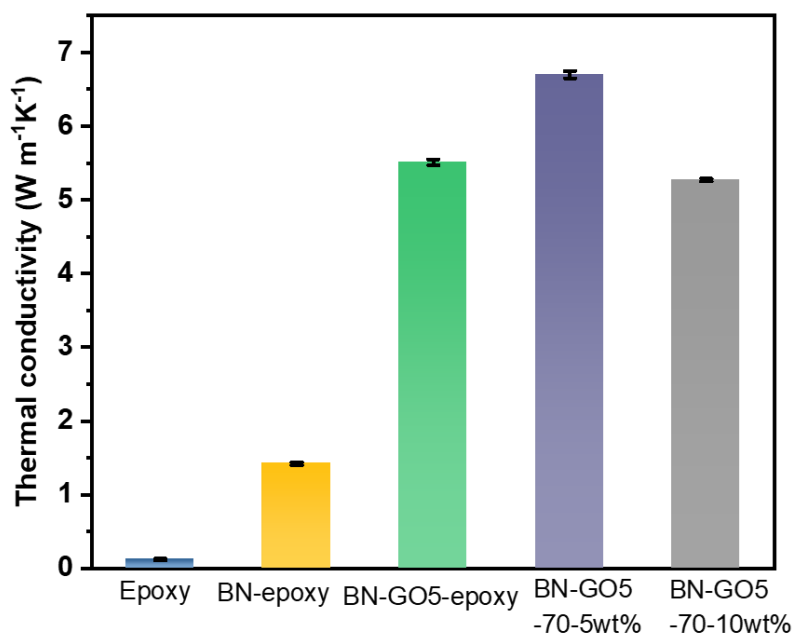


Figure 6.10 The thermal conductivities of epoxy resin, BN-epoxy, BN-GO5-epoxy and BN-GO5-70 composites.

6.5 Discussion

XRD and SEM results shown in Figure 6.2 and Figure 6.4 confirm that the BN platelets were vertically aligned in the BN-GO slices successfully. T_c values which indicate preferred orientation along a particular plane were calculated based on the XRD results.

The higher $T_c(002)$ value represents BN platelets preferred to be aligned vertically. Table 6.1 shows the $T_c(002)$ value gradually decreased from 2.57 to 1.55 in aligned BN-GO5 slice with the increase of GO content, indicating a shift in the preferred orientation towards the (100) plane as $T_c(100)$ increased from 0.31 to 0.90. These results indicate that the increasing the content of GO to a certain extent can assist in the vertical alignment of BN. SEM results (Figure 6.4 and Figure 6.6) also demonstrates the successful construction of well orientation of BN and GO. However, when the content of GO reached 7 wt%, the value of $T_c(100)$ decreased from 0.90 to 0.49, indicating a decrease in the quantity of BN oriented in the vertical direction. The related research has shown that the viscosity of GO dispersions increases with higher concentrations [227]. This is attributed to the greater interactions between GO sheets, leading to denser structures and higher viscoelastic moduli in the linear viscoelastic regime. In our study, as the GO content gradually increases, the concentration of the BN and GO mixed aqueous solution also increases, leading to a gradual increase in the solution's viscosity. When the solution's viscosity increases, the mobility of the fillers within it decreases, thereby affecting the ability of BN to align and move within the solution. The trend of BN alignment direction in composites with changes in viscosity can also be observed in other studies. The orientation of BN in the polystyrene matrix is inhibited due to the increased viscosity of polystyrene at lower temperatures [228]. Therefore, the reduced degree of vertical alignment of BN in BN-GO7 can be attributed to the increased viscosity of the mixed solution caused by the higher content of BN and GO, which impedes the alignment of BN.

The strong Van der Waals interaction between BN and GO allows them to bond tightly. The BN-GO slices exhibit excellent mechanical strength. Because the BN suspension was treated by ultrasonic, BN platelets were exfoliated, leading to the formation of

hydroxyl and amino groups on the BN sheet edges due to the hydrolysis [229, 230]. GO entities readily adhere to BNNSs, facilitated by the robust Van der Waals forces and by the potential formation of out-of-plane chemical bonds, attributed to the dangling bonds emerging on the planes and fractured edges of BN during its synthesis [231, 232]. GO acts as an adhesive, and BN sheets then were cemented due to the strong interactions. Thus, BN platelets act as bridges by GO forming an oriented pathways for directional thermal transport. The strong interactions between BN and GO decrease effective phonon scattering centres in composites, resulting in continuous conductive paths in the through-plane direction [233].

When using the hybrid different fillers, phonon reflections occur at the interfaces, which attributes to discrepancies in the vibrational modes among the constituent lattice structures. This reflection of phonons at the interfaces emerges as the paramount factor influencing the thermal flow across these boundaries [234]. Figure 6.11 presents the phonon dispersion profiles for BN and GO, as deduced from theoretical analyses and data from previous published studies [235-237]. BN and GO exhibit comparable frequency ranges, each featuring three acoustic and three optical bands, which display analogous vibrational patterns. It shows that phonon spectral of GO match well with BN, which eventually reduce the interfacial thermal resistance between the BN platelets. As a result, the thermal conductivity of BN-epoxy is much lower than BN-GO-epoxy resin.

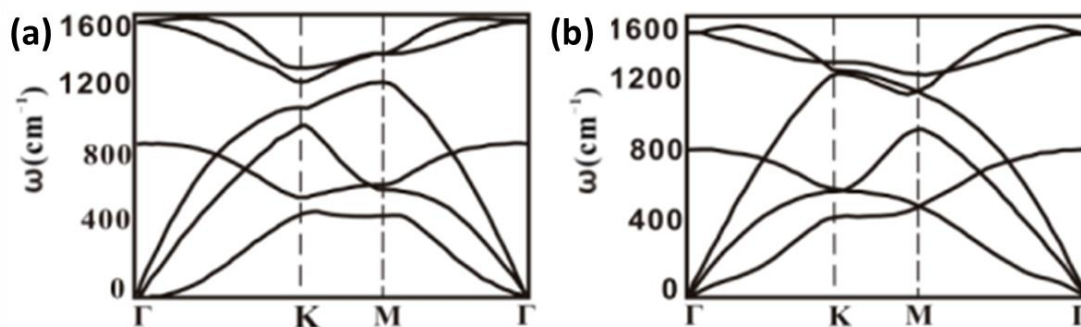


Figure 6.11 The phonon dispersion spectra of (a) h-BN [235], (b) Graphene [237].

In the BN-GO-epoxy composite, the establishment of vertically oriented thermal pathways and the use of GO as a thermal bridge work together to enhance thermal conductivity. As a result, the highest thermal conductivity of $5.51 \text{ W m}^{-1} \text{ K}^{-1}$ in BN-GO-epoxy composites is reached with 5 wt% GO in BN-GO slice. Considering GO functions as a binding agent for h-BN platelets, the content of GO has a strong influence on the value of thermal conductivity. The h-BN platelets are not adequately cross-linked by GO when the GO content is below 5 wt%, leading to less improvement in thermal conductivity [238]. Conversely, when the GO concentration exceeds 5 wt%, the overabundance of GO layers can lead to diminished heat transfer efficiency between neighbouring BN plates. The viscosity resulting from the high concentrations of GO also contributes to the degradation of BN-GO orientation.

Table 6.6 illustrates the thermal behaviour of BN-GO-epoxy composites in comparison to polymer composites reinforced with BN sheets. Historically, reported thermal conductivities typically range between 0.5 and $3.5 \text{ W m}^{-1} \text{ K}^{-1}$ and CTE values between 20 to $30 \text{ K}^{-1} \text{ ppm}$ [110] [118] [132] [239-241]. It is clear that our BN-GO5-epoxy, with its vertical alignment, achieves the highest thermal conductivity ($5.15 \text{ W m}^{-1} \text{ K}^{-1}$), which indicates BN-GO serves as a more efficient filler than raw BN in

improving thermal conductivity. Meanwhile, 70 nm BNNS was added in epoxy resin to further improve the thermal conductivity to $6.70 \text{ W m}^{-1} \text{ K}^{-1}$ (Figure 6.10).

Typically, methods for achieving vertical alignment of fillers include ice templating and magnetic/electric field alignment, both of which are complex and time-consuming, requiring liquid nitrogen, freeze-drying, and extended processing times. In contrast, our method uses a simple vacuum filtration setup to achieve vertical alignment of BN and GO. Compared to BN epoxy composites aligned using magnetic fields, our method improves thermal conductivity by 40% even with a 10% reduction in filler loading [240].

Ice templating has the advantage of facilitating vertical alignment at low filler loadings, but its ability to enhance through-plane thermal conductivity is limited. Increasing filler loading to further improve thermal conductivity is constrained by the method's limitations, as many fillers become trapped in the growing ice, aligning parallel instead of vertically. Additionally, higher filler content increases the difficulty of preparing a homogeneous filler solution, which complicates the process. This challenge is why composites prepared using ice templating typically have filler contents below 15 vol%. Therefore, although our vacuum filtration method results in composites with higher filler loadings, the thermal conductivity is also 50% higher than that of composites prepared using ice templating.

It is worth noting that the CTE value is extremely low compared to epoxy resin and other composites (Figure 6.9). The strong interaction between BN and GO also inhibits the expansion of the composites. The BN-GO-epoxy composites show significantly improved thermal performance and dimensional stability.

FR4 which is commonly used in PCBs typically has a thermal conductivity of about $0.3 \text{ W m}^{-1} \text{ K}^{-1}$ and a through-plane CTE of about $70 \text{ K}^{-1} \text{ ppm}$ [187, 188, 219]. The BN-GO-epoxy composites have improved thermal conductivity by approximately 1616.67% compared to FR4. The CTE of the BN-GO-epoxy composite has been reduced by approximately 91.43% compared to FR4 and matches well to CTE of silicon ($3 \text{ K}^{-1} \text{ ppm}$).

Table 6.6 Comparison of thermal conductivity (K) and CTE of our vertically aligned BN-GO-epoxy composite with other BN polymer composites.

Fillers	Matrix	Loading (vol%)	K ($\text{W m}^{-1} \text{ K}^{-1}$)	CTE (ppm K^{-1})	References
BNNS	PVDF	~14	1.4	-	[239]
Magnetic aligned BN	Epoxy	~50	3.59	-	[240]
Vertically aligned BN	PDMS	15.6	1.94	-	[241]
Magnetic aligned BN	Epoxy	11.7	0.85	28.7	[132]
3D BNNS aerogel	Epoxy	9.29	2.85	24	[118]
3D BNNS aerogel	Epoxy	9.6	3.13	-	[110]
Vertically aligned BN-GO	Epoxy	42	5.15	6	This work

6.6 Summary

In this chapter, an easily operated and eco-friendly vacuum-assisted method was used to prepare BN-GO-epoxy composites. The GO act as the bridges linking the BN because of the strong van der Waals interactions between them to form the thermal

transfer pathways. The obtained BN-GO5-epoxy composites show a high through-plane thermal conductivity of $5.51 \text{ W m}^{-1} \text{ K}^{-1}$. The BN-GO-epoxy composites have improved thermal conductivity by approximately 1600% compared to the commercial and recently research of FR4. The CTE of the BN-GO-epoxy composite has been reduced by approximately 91.43% compared to FR4 and matches well to CTE of silicon ($3 \text{ K}^{-1} \text{ ppm}$). In addition, the CTE of the BN-GO is excellent which is only 5 ppm K^{-1} . These results can be attributed to the vertically aligned and densely packed BN-GO structure achieved through vacuum-assisted filtration followed by slicing. To increase the thermal conductivity even further, the 70 nm nano BN platelets were mixed with epoxy resin before infiltration. When the addition of nano-BN is at 5wt% in epoxy resin, the thermal conductivity of the BN-GO5-70-5wt% composite reaches $6.7 \text{ W m}^{-1} \text{ K}^{-1}$. Therefore, BN-GO composites which have high thermal conductivity and low CTE have been successfully prepared and shown great potentials as a thermal management material.

Chapter 7 Conclusion and future work

7.1 Conclusion

In this thesis, after a review of the mechanism of heat transfer and latest research advancements in thermally conductive composites materials, several new types of epoxy resin-based thermally conductive composites were prepared. This work also investigated the relationship between the thermal conductivity and micro/nano fillers assembly technology, as well as the microstructure of the composites. The conclusions are as follows:

Due to the lack of effective filler assembly technology in the through-plane direction, the applications of thermally conductive composites have been limited by the low through-plane thermal conductivity. In this work, 3D SiCW aerogels were constructed by freeze casting method first and followed by sintered. The obtained 3D SiCW aerogels possess high porosity and light weight, while also exhibiting high mechanical strength. The characterisation on the changes to the surface of SiC fibres after sintering reveals that SiO₂ generated during the sintering process bonded the SiC fibres, thereby endowing the aerogel with a robust structure and high mechanical properties. The adjustment of the sintering temperature can control the thickness of the SiO₂ layer formed on the surface; a higher sintering temperature results in a thicker SiO₂ layer. This thickness of the SiO₂ layer, in turn, influences the thermal conductivity of the composites. At a sintering temperature of 1000°C, the SiO₂ layer reaches a thickness of 70 nm, and the composite has the highest thermal conductivity. By adjusting the proportion of raw materials in the suspension, SiCW aerogels with tailored microstructure can be achieved. An optimised 10.2 vol% SiCW loading has been proposed for the preparation of SiCW aerogels by freeze-casting method. The obtained

3D SiCWs-epoxy composites exhibit enhanced thermal conductivities, compared with that of random SiCW composite and pure epoxy resin. At the highest SiCWs loading (10.2 vol%), the through-plane thermal conductivity of the 3D SiCWs-epoxy reaches $1.55 \text{ W m}^{-1} \text{ K}^{-1}$, which is 8.1 times that of pure epoxy resin, and 1.6 times that of R-SiCW-epoxy composite. Furthermore, the 3D SiCWs-epoxy composites present a lower through-plane (48 ppm K^{-1}) and in-plane CTE (35 ppm K^{-1}) compared to the pure epoxy resin (92 ppm K^{-1}). Surface temperature changes in the composites during heating demonstrate their considerable potential for use in thermal management applications.

The in-plane thermal conductivity is also very important for the thermally conductive materials. In this work, bi-layered EBNSiC_2L composite was prepared by vacuum-assisted filtration method. h-BN and SiC whiskers were successfully aligned in the horizontal direction under the action of vacuum-assisted filtration. As a result, EBNSiC_2L increased the through-plane thermal conductivity of epoxy from $0.12 \text{ W m}^{-1} \text{ K}^{-1}$ to $1.54 \text{ W m}^{-1} \text{ K}^{-1}$ and the in-plane thermal conductivity from $0.12 \text{ W m}^{-1} \text{ K}^{-1}$ to $2.16 \text{ W m}^{-1} \text{ K}^{-1}$. The alignment of BN and SiC establishes thermal conduction pathways, which is the primary reason for the increased thermal conductivity. Surprisingly, this bilayer structure of BN and SiC not only possesses high thermal conductivity but also exhibits good dielectric properties. The EBNSiC_2L has higher dielectric constant of 9.03 at 1kHz, compared with 4.99 for epoxy at the same frequency. The dielectric loss of EBNSiC_2L bi-layered composite is only 0.015 at 1kHz. Additionally, the EBNSiC_2L composite exhibits the stability of dielectric properties at the frequency higher than 1 kHz. The enhancements in the thermal and dielectric properties of the composites show potential in future engineering applications.

Inspired by the successful enhancement of in-plane thermal conductivity through vacuum-assisted filtration, this method can also be applied to increase the through-plane thermal conductivity. By simply rotating the sample obtained after vacuum-assisted filtration by 90 degrees, horizontally aligned fillers can be converted into vertically aligned fillers, thereby achieving the goal of enhancing through-plane thermal conductivity. By employing this method, BN and GO were successfully oriented in the vertical direction. The through-plane thermal conductivity of BN-GO5 epoxy reaches up to $5.51 \text{ W m}^{-1} \text{ K}^{-1}$, which is 45 times that of pure epoxy resin. More importantly, BN-GO epoxy exhibits an ultra-low CTE (5 ppm K^{-1}), matching with that of Si materials. A low CTE significantly reduces thermal stress between electronic packaging materials, thereby mitigating potential damage and enhancing device reliability.

The following conclusions can be drawn from all the research above. Aligning fillers in the one direction to establish a thermal conduction pathway can effectively enhance the thermal conductivity of composites. The advantage of the freeze-casting method is the ability to establish the filler thermal conduction networks at a lower filler loading. Using micro-size 1D materials with a high aspect ratio, such as the SiC whiskers used as fillers in this thesis, can successfully construct a 3D network. Notably, this study discovered changes on the surface of SiC whiskers during the high-temperature sintering process, which are key to preparing the aerogels. The sintering process serves two functions: removing the polymer adhesive and connecting the SiC whiskers. High temperatures and an oxygen environment are essential conditions for this process. Therefore, the key to preparing a three-dimensional aerogel structure using the freeze-casting method is that the filler can be sintered in air conditions to form solid connections. These connections also contribute to the improvement of thermal

conductivity. Compared to the freeze-casting method, the vacuum-assisted filtration method is simpler, more efficient, and can orientate more fillers. The utilization of mixed fillers also benefits the enhancement of thermal conductivity, especially when the phonon spectrum of the mixed fillers is match, such as with BN and GO highlighted in this study. Furthermore, this research demonstrates that thermally conductive composites have advantages not only in thermal conductivity but also in dielectric and thermo-mechanical performance. The results of this study reveal that confining the epoxy resin matrix within the filler layers can effectively lower the CTE. Moreover, a reduction in the gaps between the layers of fillers leads to a more substantial decrease in CTE, and an increased filler loading further diminishes the CTE. This investigation underlines the comprehensive benefits of strategic filler alignment and loading in enhancing the material properties of thermally conductive composites. Consequently, these composites are highly promising for applications in the electronics sector, where thermal management and compatibility with existing semiconductor technologies are critical for the performance and longevity of electronic devices.

7.2 Future work

This research has produced several promising results, and there are some suggestions based on the results for future work. These suggested research directions have not been explored or realized within the scope of this thesis due to constraints related to materials, time, or resources.

- BN-GO epoxy composites show high thermal conductivity because of the match of phonon spectrum. In future, the research on phonon heat transfer and coupling mechanisms can be further investigated. Currently, there is limited study on phonon-phonon and electron-phonon coupling between different

materials, as well as the specific mechanisms of phonon transport at interfaces. Future research will focus on deepening insights into the mechanisms underlying thermal conduction.

- In this thesis, the maximum size of the composites was limited to 12 mm, primarily constrained by the capacity of the preparation equipment. This size is suitable for laboratory experiments, but industrial applications require larger dimensions. Thus, methods for preparing larger-sized composites must be explored to meet the needs of practical applications.
- The multifaceted performance of the composite has been obtained. Professional simulation software enables the creation of models for electronic packaging, into which the properties of the composite derived from the research are integrated. This allows for the simulation of the composite under actual application conditions. The detailed thermal conductivity and thermal stress of the composite within electronic packaging models can be observed, thereby guiding the design and heat dissipation strategies for actual electronic packaging.
- After completing the simulations, the application of composites in electronic packaging emerges as a promising area for exploration. They can be utilized as substrates for mounting electronic components on PCBs or as thermal interface materials. This future research could facilitate the transition from academic research to practical application.
- The technology of preparing SiC whisker aerogels using the freeze casting method is well-established in this study. In future research, substituting the matrix material could explore a broader range of applications. For instance, by

replacing the matrix material with paraffin, the composites can be utilized as a phase change material. Research in this direction is already progress.

- Another potential area for future research would be the multifunctional composites. Besides serving as thermal management materials, the composites can also be investigated for use as other functional materials, such as electromagnetic wave absorption. SiC was widely used in the wave absorption research, and some important results have been presented in this thesis, for example, the aligned SiC whisker structure and the light weight SiC aerogels. By integrating the results of this thesis with literature research, we can anticipate that SiC aerogels or composites possess promising wave absorption properties.

References

1. Hobley, A., *Will gas be gone in the United Kingdom (UK) by 2050? An impact assessment of urban heat decarbonisation and low emission vehicle uptake on future UK energy system scenarios*. Renewable energy, 2019. **142**: p. 695-705.
2. Moore, A.L. and L. Shi, *Emerging challenges and materials for thermal management of electronics*. Materials today, 2014. **17**(4): p. 163-174.
3. Tu, K.-N., *Reliability challenges in 3D IC packaging technology*. Microelectronics Reliability, 2011. **51**(3): p. 517-523.
4. Sheldon, D.D.J. *2.5/3D Packaging NEPP ETW*. 2018; Available from: <https://nepp.nasa.gov/docs/etw/2018/19JUNE18/1330a%20-%20Sheldon%20-%20NEPP%20ETW%20djs%20final.pdf>.
5. Garimella, S.V., et al., *Thermal challenges in next-generation electronic systems*. IEEE Transactions on Components and Packaging Technologies, 2008. **31**(4): p. 801-815.
6. Schelling, P.K., L. Shi, and K.E. Goodson, *Managing heat for electronics*. Materials Today, 2005. **8**(6): p. 30-35.
7. Luedtke, A., *Thermal management materials for high - performance applications*. Advanced engineering materials, 2004. **6**(3): p. 142-144.
8. Chen, H., et al., *Thermal conductivity of polymer-based composites: Fundamentals and applications*. Progress in Polymer Science, 2016. **59**: p. 41-85.
9. Han, Y., et al., *Enhanced thermal conductivities of epoxy nanocomposites via incorporating in-situ fabricated hetero-structured SiC-BNNS fillers*. Composites Science and Technology, 2020. **187**: p. 107944.
10. Han, Z. and A. Fina, *Thermal conductivity of carbon nanotubes and their polymer nanocomposites: A review*. Progress in polymer science, 2011. **36**(7): p. 914-944.
11. Huang, C., X. Qian, and R. Yang, *Thermal conductivity of polymers and polymer nanocomposites*. Materials Science and Engineering: R: Reports, 2018. **132**: p. 1-22.
12. Tsekmes, I., et al. *Thermal conductivity of polymeric composites: A review*. in *2013 IEEE International Conference on Solid Dielectrics (ICSD)*. 2013. IEEE.
13. Zweben, C., *Thermal materials solve power electronics challenges*. Power Electronics Technology, 2006. **32**(2): p. 40-47.
14. Zhang, L., H. Deng, and Q. Fu, *Recent progress on thermal conductive and electrical insulating polymer composites*. Composites Communications, 2018. **8**: p. 74-82.
15. assembly, P.b. 2019; Available from: <https://pcbboardassembly.com/fr-4-pcb/>.

16. Bian, W., et al., *The synergistic effects of the micro-BN and nano-Al₂O₃ in micro-nano composites on enhancing the thermal conductivity for insulating epoxy resin*. Composites Science and Technology, 2018. **168**: p. 420-428.
17. Cao, M., et al., *Continuous network of CNTs in poly (vinylidene fluoride) composites with high thermal and mechanical performance for heat exchangers*. Composites Science and Technology, 2019. **173**: p. 33-40.
18. Jiang, C., et al., *Preparation of high performance AlN/Hydantion composite by gelcasting and infiltration processes*. Ceramics International, 2014. **40**(1): p. 2535-2538.
19. Han, Y., et al., *Nest-like hetero-structured BNNS@ SiCnws fillers and significant improvement on thermal conductivities of epoxy composites*. Composites Part B: Engineering, 2021. **210**: p. 108666.
20. Guo, Y., et al., *Factors affecting thermal conductivities of the polymers and polymer composites: A review*. Composites Science and Technology, 2020. **193**: p. 108134.
21. Zhang, F., Y. Feng, and W. Feng, *Three-dimensional interconnected networks for thermally conductive polymer composites: Design, preparation, properties, and mechanisms*. Materials Science and Engineering: R: Reports, 2020. **142**: p. 100580.
22. Jasmee, S., et al., *Interface thermal resistance and thermal conductivity of polymer composites at different types, shapes, and sizes of fillers: A review*. Polymer Composites, 2021. **42**(6): p. 2629-2652.
23. Bai, X., et al., *Recent progress in thermally conductive polymer/boron nitride composites by constructing three-dimensional networks*. Composites Communications, 2021. **24**: p. 100650.
24. Yang, J., et al., *An elegant coupling: Freeze-casting and versatile polymer composites*. Progress in Polymer Science, 2020. **109**: p. 101289.
25. Zhang, L., et al., *Ice-templating synthesis of hierarchical and anisotropic silver-nanowire-fabric aerogel and its application for enhancing thermal energy storage composites*. ACS sustainable chemistry & engineering, 2019. **7**(24): p. 19910-19917.
26. Feng, W., et al., *Fabrication of SiCf-CNTs/SiC composites with high thermal conductivity by vacuum filtration combined with CVI*. Materials Science and Engineering: A, 2016. **662**: p. 506-510.
27. Zhao, K., et al., *Vacuum filtration-assisted design of hierarchical structure in polyimide-BN composite films: Toward enhanced thermal conductivity, low dielectric and electrical insulation*. Ceramics International, 2024.
28. Cao, L., et al., *Multi-functional properties of MWCNT/PVA buckypapers fabricated by vacuum filtration combined with hot press: thermal, electrical and electromagnetic shielding*. Nanomaterials, 2020. **10**(12): p. 2503.
29. Tan, Z., et al., *Fabrication of diamond/aluminum composites by vacuum hot pressing: process optimization and thermal properties*. Composites Part B: Engineering, 2013. **47**: p. 173-180.

30. Zhang, X., et al., *Enhanced thermally conductivity and mechanical properties of polyethylene (PE)/boron nitride (BN) composites through multistage stretching extrusion*. *Composites Science and Technology*, 2013. **89**: p. 24-28.
31. Zhao, X. and L. Ye, *Structure and properties of highly oriented polyoxymethylene/multi-walled carbon nanotube composites produced by hot stretching*. *Composites Science and Technology*, 2011. **71**(10): p. 1367-1372.
32. Dasgupta, A., *Thermomechanical Analysis and design*, in *Handbook of Electronic Package Design*. 2018, CRC Press. p. 477-528.
33. Yamada, T., et al. *Development of a Low CTE chip scale package*. in *2013 IEEE 63rd Electronic Components and Technology Conference*. 2013. IEEE.
34. Wong, C. and R.S. Bollampally, *Thermal conductivity, elastic modulus, and coefficient of thermal expansion of polymer composites filled with ceramic particles for electronic packaging*. *Journal of applied polymer science*, 1999. **74**(14): p. 3396-3403.
35. Goyal, R., A. Tiwari, and Y.S. Negi, *High performance polymer/AlN composites for electronic substrate application*. *Composites Part B: Engineering*, 2013. **47**: p. 70-74.
36. Shen, Z. and J. Feng, *Achieving vertically aligned SiC microwires networks in a uniform cold environment for polymer composites with high through-plane thermal conductivity enhancement*. *Composites Science and Technology*, 2019. **170**: p. 135-140.
37. Pop, E., S. Sinha, and K.E. Goodson, *Heat generation and transport in nanometer-scale transistors*. *Proceedings of the IEEE*, 2006. **94**(8): p. 1587-1601.
38. Mahajan, R., C.-p. Chiu, and G. Chrysler, *Cooling a microprocessor chip*. *Proceedings of the IEEE*, 2006. **94**(8): p. 1476-1486.
39. Hamann, H.F., et al., *Hotspot-limited microprocessors: Direct temperature and power distribution measurements*. *IEEE Journal of Solid-State Circuits*, 2006. **42**(1): p. 56-65.
40. Wan, Y.-J., et al., *Recent advances in polymer-based electronic packaging materials*. *Composites Communications*, 2020. **19**: p. 154-167.
41. Xu, H.J., et al., *Review on heat conduction, heat convection, thermal radiation and phase change heat transfer of nanofluids in porous media: Fundamentals and applications*. *Chemical Engineering Science*, 2019. **195**: p. 462-483.
42. Namsheer, K. and C.S. Rout, *Conducting polymers: a comprehensive review on recent advances in synthesis, properties and applications*. *RSC advances*, 2021. **11**(10): p. 5659-5697.
43. Burger, N., et al., *Review of thermal conductivity in composites: mechanisms, parameters and theory*. 2016. **61**: p. 1-28.
44. T'Joen, C., et al., *A review on polymer heat exchangers for HVAC&R applications*. *International journal of refrigeration*, 2009. **32**(5): p. 763-779.

45. Vadivelu, M., C.R. Kumar, and G.M. Joshi, *Polymer composites for thermal management: a review*. Composite Interfaces, 2016. **23**(9): p. 847-872.
46. Singh, V., et al., *High thermal conductivity of chain-oriented amorphous polythiophene*. Nature nanotechnology, 2014. **9**(5): p. 384-390.
47. Zeng, X., et al., *Fibrous epoxy substrate with high thermal conductivity and low dielectric property for flexible electronics*. Advanced Electronic Materials, 2016. **2**(5): p. 1500485.
48. Akatsuka, M. and Y. Takezawa, *Study of high thermal conductive epoxy resins containing controlled high - order structures*. Journal of applied polymer science, 2003. **89**(9): p. 2464-2467.
49. Ruan, K., Y. Guo, and J. Gu, *Liquid crystalline polyimide films with high intrinsic thermal conductivities and robust toughness*. Macromolecules, 2021. **54**(10): p. 4934-4944.
50. Pierson, H.O., *Handbook of carbon, graphite, diamonds and fullerenes: processing, properties and applications*. 2012: William Andrew.
51. Wypych, G., *Handbook of fillers*. 1999.
52. Fischer, J.E., *Carbon nanotubes: structure and properties*. Nanotubes and nanofibers, 2006. **1**(1).
53. Shtein, M., et al., *Thermally conductive graphene-polymer composites: size, percolation, and synergy effects*. Chemistry of Materials, 2015. **27**(6): p. 2100-2106.
54. Wang, X.-f., et al., *Synthesis and sintering of beryllium oxide nanoparticles*. Progress in Natural Science: Materials International, 2010. **20**: p. 81-86.
55. Xu, X., et al., *Thermal conductivity of polymers and their nanocomposites*. 2018. **30**(17): p. 1705544.
56. Ali, S., et al., *Effect of Morphology and Crystal Structure on the Thermal Conductivity of Titania Nanotubes*. Nanoscale research letters, 2018. **13**: p. 1-11.
57. Zhao, M., et al., *Defect engineering in development of low thermal conductivity materials: a review*. Journal of the European Ceramic Society, 2017. **37**(1): p. 1-13.
58. Slack, G.A., et al., *The intrinsic thermal conductivity of AlN*. Journal of Physics and Chemistry of Solids, 1987. **48**(7): p. 641-647.
59. Yao, Y., et al., *Vertically aligned and interconnected SiC nanowire networks leading to significantly enhanced thermal conductivity of polymer composites*. ACS applied materials & interfaces, 2018. **10**(11): p. 9669-9678.
60. Zhou, W.Y., et al., *Thermally conductive silicone rubber reinforced with boron nitride particle*. Polymer composites, 2007. **28**(1): p. 23-28.
61. Zhou, W., et al., *Effect of the particle size of Al₂O₃ on the properties of filled heat - conductive silicone rubber*. Journal of Applied Polymer Science, 2007. **104**(2): p. 1312-1318.

62. Pashayi, K., et al., *High thermal conductivity epoxy-silver composites based on self-constructed nanostructured metallic networks*. Journal of applied physics, 2012. **111**(10).
63. Su, J., Y. Xiao, and M. Ren, *Enhanced thermal conductivity in epoxy nanocomposites with hybrid boron nitride nanotubes and nanosheets*. physica status solidi (a), 2013. **210**(12): p. 2699-2705.
64. Kargar, F., et al., *Thermal percolation threshold and thermal properties of composites with high loading of graphene and boron nitride fillers*. ACS applied materials & interfaces, 2018. **10**(43): p. 37555-37565.
65. Burger, N., et al., *Review of thermal conductivity in composites: mechanisms, parameters and theory*. Progress in Polymer Science, 2016. **61**: p. 1-28.
66. Kim, K., et al., *Chemically modified boron nitride-epoxy terminated dimethylsiloxane composite for improving the thermal conductivity*. Ceramics International, 2014. **40**(1): p. 2047-2056.
67. Biercuk, M., et al., *Carbon nanotube composites for thermal management*. Applied physics letters, 2002. **80**(15): p. 2767-2769.
68. Zhang, P., et al., *Thermal properties of graphene filled polymer composite thermal interface materials*. Macromolecular Materials and Engineering, 2017. **302**(9): p. 1700068.
69. Zhang, R., et al., *High antibacterial performance of electrospinning silk fibroin/gelatin film modified with graphene oxide - silver nanoparticles*. Journal of Applied Polymer Science, 2019. **136**(35): p. 47904.
70. Wang, S., et al., *Highly thermal conductive copper nanowire composites with ultralow loading: toward applications as thermal interface materials*. ACS Applied Materials & Interfaces, 2014. **6**(9): p. 6481-6486.
71. Shen, H., et al., *Bioinspired modification of h-BN for high thermal conductive composite films with aligned structure*. ACS applied materials & interfaces, 2015. **7**(10): p. 5701-5708.
72. Wu, G., et al., *The effect of modified AlN on the thermal conductivity, mechanical and thermal properties of AlN/polystyrene composites*. RSC advances, 2016. **6**(104): p. 102542-102548.
73. Pan, W., et al., *Interfacial engineering of graphene nanosheets at mgo particles for thermal conductivity enhancement of polymer composites*. Nanomaterials, 2019. **9**(5).
74. Panda, A., *Effect of shape, size and content on the effective thermal conductivity BeO filled polymer composites*. 2013.
75. Noma, Y., Y. Saga, and N. Une, *Amorphous silica-coated graphite particles for thermally conductive and electrically insulating resins*. Carbon, 2014. **78**: p. 204-211.
76. Patti, A., et al., *The effect of filler functionalization on dispersion and thermal conductivity of polypropylene/multi wall carbon nanotubes composites*. Composites Part B: Engineering, 2016. **94**: p. 350-359.

77. Xie, X. and D. Yang, *Multi-functionalization of Al₂O₃ nanoparticles for enhancing thermal conductivity of epoxy natural rubber composites*. Applied Surface Science, 2022. **602**: p. 154335.
78. Chandrashekar, A., et al., *Non-covalent surface functionalization of nanofillers towards the enhancement of thermal conductivity of polymer nanocomposites: A mini review*. European Polymer Journal, 2023: p. 112379.
79. Yu, Z.-Q., et al., *Boride ceramics covalent functionalization and its effect on the thermal conductivity of epoxy composites*. Materials Chemistry and Physics, 2015. **164**: p. 214-222.
80. Teng, C.-C., et al., *Thermal conductivity and structure of non-covalent functionalized graphene/epoxy composites*. Carbon, 2011. **49**(15): p. 5107-5116.
81. Chen, L., et al., *Enhanced thermal conductivity of benzoxazine nanocomposites based on non-covalent functionalized hexagonal boron nitride*. Composites Science and Technology, 2019. **182**: p. 107741.
82. Mi, Y.-n., et al., *Thermally conductive aluminum nitride–multiwalled carbon nanotube/cyanate ester composites with high flame retardancy and low dielectric loss*. Industrial & Engineering Chemistry Research, 2013. **52**(9): p. 3342-3353.
83. Lewis, J.S., et al., *Thermal and electrical conductivity control in hybrid composites with graphene and boron nitride fillers*. Materials Research Express, 2019. **6**(8): p. 085325.
84. Xu, Y., D. Chung, and C. Mroz, *Thermally conducting aluminum nitride polymer-matrix composites*. Composites Part A: Applied science and manufacturing, 2001. **32**(12): p. 1749-1757.
85. Xie, B.-H., X. Huang, and G.-J. Zhang, *High thermal conductive polyvinyl alcohol composites with hexagonal boron nitride microplatelets as fillers*. Composites Science and Technology, 2013. **85**: p. 98-103.
86. Kusunose, T., et al., *Fabrication of epoxy/silicon nitride nanowire composites and evaluation of their thermal conductivity*. Journal of Materials Chemistry A, 2013. **1**(10): p. 3440-3445.
87. Zeng, X., et al., *Artificial nacre-like papers based on noncovalent functionalized boron nitride nanosheets with excellent mechanical and thermally conductive properties*. Nanoscale, 2015. **7**(15): p. 6774-6781.
88. Sun, N., et al., *Hot-pressing induced orientation of boron nitride in polycarbonate composites with enhanced thermal conductivity*. Composites Part A: Applied Science and Manufacturing, 2018. **110**: p. 45-52.
89. Wang, H., et al., *An electrospinning–electrospraying technique for connecting electrospun fibers to enhance the thermal conductivity of boron nitride/polymer composite films*. Composites Part B: Engineering, 2022. **230**: p. 109505.
90. Huang, X., et al., *Role of interface on the thermal conductivity of highly filled dielectric epoxy/AlN composites*. The Journal of Physical Chemistry C, 2012. **116**(25): p. 13629-13639.

91. Qi, X.-d., et al., *Tailoring the hybrid network structure of boron nitride/carbon nanotube to achieve thermally conductive poly (vinylidene fluoride) composites*. Composites Communications, 2019. **13**: p. 30-36.
92. Guo, C., L. Zhou, and J. Lv, *Effects of expandable graphite and modified ammonium polyphosphate on the flame-retardant and mechanical properties of wood flour-polypropylene composites*. Polymers and Polymer Composites, 2013. **21**(7): p. 449-456.
93. Song, W.L., et al., *Polymer/boron nitride nanocomposite materials for superior thermal transport performance*. Angewandte Chemie, 2012. **124**(26): p. 6604-6607.
94. Liu, Z., *Study on the effect of fillers on thermal conductivity of composites* 2021.
95. Versavaud, S., et al., *Influence of injection molding on the electrical properties of polyamide 12 filled with multi-walled carbon nanotubes*. Polymer, 2014. **55**(26): p. 6811-6818.
96. Enomoto, K., et al., *Effect of filler orientation on thermal conductivity of polypropylene matrix carbon nanofiber composites*. Japanese journal of applied physics, 2005. **44**(6L): p. L888.
97. Mirkhalaf, M. and F. Barthelat, *Nacre-like materials using a simple doctor blading technique: Fabrication, testing and modeling*. Journal of the mechanical behavior of biomedical materials, 2016. **56**: p. 23-33.
98. Li, Q., et al., *Ultrahigh thermal conductivity of assembled aligned multilayer graphene/epoxy composite*. Chemistry of Materials, 2014. **26**(15): p. 4459-4465.
99. Kong, X., et al., *Two-dimensional hexagonal boron nitride nanosheets as lateral heat spreader with high thermal conductivity*. Frontiers in Materials, 2022. **8**: p. 817061.
100. Yuan, C., et al., *Thermal conductivity of polymer-based composites with magnetic aligned hexagonal boron nitride platelets*. ACS applied materials & interfaces, 2015. **7**(23): p. 13000-13006.
101. Kim, K. and J. Kim, *Magnetic aligned AlN/epoxy composite for thermal conductivity enhancement at low filler content*. Composites Part B: Engineering, 2016. **93**: p. 67-74.
102. Cho, H.-B., et al., *Insulating polymer nanocomposites with high-thermal-conduction routes via linear densely packed boron nitride nanosheets*. Composites Science and Technology, 2016. **129**: p. 205-213.
103. Ding, P., et al., *Anisotropic thermal conductive properties of hot-pressed polystyrene/graphene composites in the through-plane and in-plane directions*. Composites Science and Technology, 2015. **109**: p. 25-31.
104. Yu, C., et al., *Hot-pressing induced alignment of boron nitride in polyurethane for composite films with thermal conductivity over 50 Wm⁻¹ K⁻¹*. Composites Science and Technology, 2018. **160**: p. 199-207.

105. Yang, X., et al., *Significant improvement of thermal conductivities for BNNS/PVA composite films via electrospinning followed by hot-pressing technology*. Composites Part B: Engineering, 2019. **175**: p. 107070.
106. Gu, J., et al., *Dielectric thermally conductive boron nitride/polyimide composites with outstanding thermal stabilities via in-situ polymerization-electrospinning-hot press method*. Composites Part A: Applied Science and Manufacturing, 2017. **94**: p. 209-216.
107. Ruan, K., et al., *Improved thermal conductivities in polystyrene nanocomposites by incorporating thermal reduced graphene oxide via electrospinning-hot press technique*. Composites Communications, 2018. **10**: p. 68-72.
108. Nam, T.H., et al., *Effects of stretching on mechanical properties of aligned multi-walled carbon nanotube/epoxy composites*. Composites Part A: Applied Science and Manufacturing, 2014. **64**: p. 194-202.
109. Park, J.G., et al., *Thermal conductivity of MWCNT/epoxy composites: The effects of length, alignment and functionalization*. Carbon, 2012. **50**(6): p. 2083-2090.
110. Chen, J., et al., *Cellulose nanofiber supported 3D interconnected BN nanosheets for epoxy nanocomposites with ultrahigh thermal management capability*. 2017. **27**(5): p. 1604754.
111. Hu, J., et al., *Polymer composite with improved thermal conductivity by constructing a hierarchically ordered three-dimensional interconnected network of BN*. 2017. **9**(15): p. 13544-13553.
112. Yao, Y., et al., *Construction of 3D skeleton for polymer composites achieving a high thermal conductivity*. 2018. **14**(13): p. 1704044.
113. Ferraro, C., et al., *Light and strong SiC networks*. 2016. **26**(10): p. 1636-1645.
114. Li, W., K. Lu, and J.J.I.m.r. Walz, *Freeze casting of porous materials: review of critical factors in microstructure evolution*. 2012. **57**(1): p. 37-60.
115. Laurie, J., et al., *Colloidal suspensions for the preparation of ceramics by a freeze casting route*. 1992. **147**: p. 320-325.
116. Deville, S.J.A.E.M., *Freeze - casting of porous ceramics: a review of current achievements and issues*. 2008. **10**(3): p. 155-169.
117. Deville, S., et al., *Freezing as a path to build complex composites*. 2006. **311**(5760): p. 515-518.
118. Zeng, X., et al., *Ice - templated assembly strategy to construct 3D boron nitride nanosheet networks in polymer composites for thermal conductivity improvement*. 2015. **11**(46): p. 6205-6213.
119. Cui, Y., et al., *Fabrication of EVA connected 3D BN network for enhancing the thermal conductivity of epoxy composites*. Composites Part B: Engineering, 2021. **224**: p. 109203.

120. Qin, M., et al., *Efficiently controlling the 3D thermal conductivity of a polymer nanocomposite via a hyperelastic double - continuous network of graphene and sponge*. *Advanced functional materials*, 2018. **28**(45): p. 1805053.
121. Takenaka, K. and M. Ichigo, *Thermal expansion adjustable polymer matrix composites with giant negative thermal expansion filler*. *Composites Science and Technology*, 2014. **104**: p. 47-51.
122. Miller, W., et al., *Reduced thermal stress in composites via negative thermal expansion particulate fillers*. *Composites science and technology*, 2010. **70**(2): p. 318-327.
123. Saba, N. and M. Jawaid, *A review on thermomechanical properties of polymers and fibers reinforced polymer composites*. *Journal of industrial and engineering chemistry*, 2018. **67**: p. 1-11.
124. Kalaitzidou, K., H. Fukushima, and L.T. Drzal, *Multifunctional polypropylene composites produced by incorporation of exfoliated graphite nanoplatelets*. *Carbon*, 2007. **45**(7): p. 1446-1452.
125. Warriar, A., et al., *The effect of adding carbon nanotubes to glass/epoxy composites in the fibre sizing and/or the matrix*. *Composites Part A: Applied Science and Manufacturing*, 2010. **41**(4): p. 532-538.
126. Kiba, S., et al., *Prototype of low thermal expansion materials: fabrication of mesoporous silica/polymer composites with densely filled polymer inside mesopore space*. *Chemistry—An Asian Journal*, 2010. **5**(9): p. 2100-2105.
127. Wu, H. and L.T. Drzal, *Effect of graphene nanoplatelets on coefficient of thermal expansion of polyetherimide composite*. *Materials Chemistry and Physics*, 2014. **146**(1-2): p. 26-36.
128. Wang, S., et al., *Effect of nanotube functionalization on the coefficient of thermal expansion of nanocomposites*. *Advanced functional materials*, 2007. **17**(1): p. 87-92.
129. Ren, L., et al., *Engineering the coefficient of thermal expansion and thermal conductivity of polymers filled with high aspect ratio silica nanofibers*. *Composites Part B: Engineering*, 2014. **58**: p. 228-234.
130. Liang, X. and F. Dai, *Epoxy nanocomposites with reduced graphene oxide-constructed three-dimensional networks of single wall carbon nanotube for enhanced thermal management capability with low filler loading*. *ACS applied materials & interfaces*, 2019. **12**(2): p. 3051-3058.
131. Firkowska, I., et al., *The origin of high thermal conductivity and ultralow thermal expansion in copper–graphite composites*. *Nano letters*, 2015. **15**(7): p. 4745-4751.
132. Lin, Z., et al., *Magnetic alignment of hexagonal boron nitride platelets in polymer matrix: toward high performance anisotropic polymer composites for electronic encapsulation*. *Acs Appl Mater Interfaces*, 2013. **5**(15): p. 7633-7640.
133. Psarras, G., *Fundamentals of dielectric theories*, in *Dielectric polymer materials for high-density energy storage*. 2018, Elsevier. p. 11-57.

134. Qin, M., L. Zhang, and H. Wu, *Dielectric loss mechanism in electromagnetic wave absorbing materials*. *Advanced Science*, 2022. **9**(10): p. 2105553.
135. Hao, X., *A review on the dielectric materials for high energy-storage application*. *Journal of Advanced Dielectrics*, 2013. **3**(01): p. 1330001.
136. Huang, X., et al., *High-k polymer nanocomposites with 1D filler for dielectric and energy storage applications*. *Progress in Materials Science*, 2019. **100**: p. 187-225.
137. Lin, X., et al., *High temperature electrical energy storage: advances, challenges, and frontiers*. *Chemical Society Reviews*, 2016. **45**(21): p. 5848-5887.
138. Pan, J., et al., *Dielectric characteristics of poly (ether ketone ketone) for high temperature capacitive energy storage*. *Applied Physics Letters*, 2009. **95**(2): p. 022902.
139. Zhang, Y., et al., *Excellent energy storage performance and thermal property of polymer-based composite induced by multifunctional one-dimensional nanofibers oriented in-plane direction*. *Nano energy*, 2019. **56**: p. 138-150.
140. Chi, Q., et al., *Excellent energy storage properties with high-temperature stability in sandwich-structured polyimide-based composite films*. *ACS Sustainable Chemistry & Engineering*, 2018. **7**(1): p. 748-757.
141. Chen, S., et al., *Asymmetric alicyclic amine-polyether amine molecular chain structure for improved energy storage density of high-temperature crosslinked polymer capacitor*. *Chemical Engineering Journal*, 2020. **387**: p. 123662.
142. Xiao, M. and B.X. Du, *Review of high thermal conductivity polymer dielectrics for electrical insulation*. *High Voltage*, 2016. **1**(1): p. 34-42.
143. Yang, S., et al., *Fabrication of morphologically controlled composites with high thermal conductivity and dielectric performance from aluminum nanoflake and recycled plastic package*. *ACS applied materials & interfaces*, 2018. **11**(3): p. 3388-3399.
144. Sun, C., et al., *The effect of multilayered film structure on the dielectric properties of composites films based on P (VDF-HFP)/Ni (OH) 2*. *Nanocomposites*, 2019. **5**(1): p. 36-48.
145. Huang, L., et al., *Spherical and flake-like BN filled epoxy composites: Morphological effect on the thermal conductivity, thermo-mechanical and dielectric properties*. *Journal of Materials Science: Materials in Electronics*, 2015. **26**: p. 3564-3572.
146. Wang, Z., et al., *Alignment of boron nitride nanofibers in epoxy composite films for thermal conductivity and dielectric breakdown strength improvement*. *Nanomaterials*, 2018. **8**(4): p. 242.
147. Wang, Z., et al., *Dielectric properties and thermal conductivity of epoxy composites using core/shell structured Si/SiO₂/Polydopamine*. *Composites Part B: Engineering*, 2018. **140**: p. 83-90.

148. Wang, Z., et al., *Sandwiched epoxy–alumina composites with synergistically enhanced thermal conductivity and breakdown strength*. Journal of materials science, 2017. **52**: p. 4299-4308.
149. Wang, Y., et al., *Compositional tailoring effect on electric field distribution for significantly enhanced breakdown strength and restrained conductive loss in sandwich-structured ceramic/polymer nanocomposites*. Journal of Materials Chemistry A, 2017. **5**(9): p. 4710-4718.
150. Wang, Y., et al., *Significantly enhanced breakdown strength and energy density in sandwich - structured barium titanate/poly (vinylidene fluoride) nanocomposites*. Advanced Materials, 2015. **27**(42): p. 6658-6663.
151. Hu, P., et al., *Highly enhanced energy density induced by hetero-interface in sandwich-structured polymer nanocomposites*. Journal of Materials Chemistry A, 2013. **1**(39): p. 12321-12326.
152. Wang, Z., et al., *Boron nitride nanosheets from different preparations and correlations with their material properties*. Industrial & Engineering Chemistry Research, 2019. **58**(40): p. 18644-18653.
153. Wang, Z., et al., *Dispersion of high-quality boron nitride nanosheets in polyethylene for nanocomposites of superior thermal transport properties*. Nanoscale Advances, 2020. **2**(6): p. 2507-2513.
154. Zhang, B., et al., *High-Efficient Liquid Exfoliation of Boron Nitride Nanosheets Using Aqueous Solution of Alkanolamine*. Nanoscale Research Letters, 2017. **12**(1): p. 596.
155. Huang, X., P. Jiang, and T. Tanaka, *A review of dielectric polymer composites with high thermal conductivity*. IEEE Electrical Insulation Magazine, 2011. **27**(4): p. 8-16.
156. Song, N., et al., *Enhancement of thermal conductivity in polyamide-6/graphene composites via a “bridge effect” of silicon carbide whiskers*. RSC advances, 2017. **7**(73): p. 46306-46312.
157. Shen, Z.H., et al., *High - throughput phase - field design of high - energy - density polymer nanocomposites*. Advanced Materials, 2018. **30**(2): p. 1704380.
158. Due, J. and A.J. Robinson, *Reliability of thermal interface materials: A review*. Applied Thermal Engineering, 2013. **50**(1): p. 455-463.
159. Wang, H., et al., *Recovery of waste printed circuit boards through pyrometallurgical processing: A review*. Resources, Conservation and Recycling, 2017. **126**: p. 209-218.
160. Zissis, G., P. Bertoldi, and T. Serrenho, *Update on the Status of LED-Lighting world market since 2018*. Publications Office of the European Union: Luxembourg, 2021.
161. Wu, B.-S., et al., *Comparison and perspective of conventional and LED lighting for photobiology and industry applications*. Environmental and Experimental Botany, 2020. **171**: p. 103953.

162. Bispo-Jr, A.G., et al., *Recent prospects on phosphor-converted LEDs for lighting, displays, phototherapy, and indoor farming*. Journal of Luminescence, 2021. **237**: p. 118167.
163. Huang, D.-S., et al., *Design of fins with a grooved heat pipe for dissipation of heat from high-powered automotive LED headlights*. Energy Conversion and Management, 2019. **180**: p. 550-558.
164. Radziemska, E., *The effect of temperature on the power drop in crystalline silicon solar cells*. Renewable energy, 2003. **28**(1): p. 1-12.
165. Hausler, T. and H. Rogaß. *Latent heat storage on photovoltaics*. in *Sixteenth European Photovoltaic Solar Energy Conference*. 2020. Routledge.
166. Kalogirou, S.A. and Y. Tripanagnostopoulos, *Hybrid PV/T solar systems for domestic hot water and electricity production*. Energy conversion and management, 2006. **47**(18-19): p. 3368-3382.
167. Pavlovic, A., et al., *Thermal Behavior of Monocrystalline Silicon Solar Cells: A Numerical and Experimental Investigation on the Module Encapsulation Materials*. Journal of Applied and Computational Mechanics, 2021. **7**(3): p. 1847-1855.
168. Oh, J., et al., *Reduction of PV module temperature using thermally conductive backsheets*. IEEE Journal of Photovoltaics, 2018. **8**(5): p. 1160-1167.
169. Saadah, M., et al., *Graphene-Enhanced Thermal Interface Materials for Thermal Management of Photovoltaic Solar Cells*. arXiv preprint arXiv:1610.01726, 2016.
170. Agari, Y., A. Ueda, and S. Nagai, *Thermal conductivity of a polymer composite*. Journal of Applied Polymer Science, 1993. **49**(9): p. 1625-1634.
171. Marturi, N., *Vision and visual servoing for nanomanipulation and nanocharacterization in scanning electron microscope*. 2013. p. 63.
172. Dwiranti, A., et al., *Imaging the inner structure of chromosomes: contribution of focused ion beam/scanning electron microscopy to chromosome research*. Chromosome Research, 2021. **29**: p. 51-62.
173. Amin, G., *ZnO and CuO nanostructures: low temperature growth, characterization, their optoelectronic and sensing applications*. 2012, Linköping University Electronic Press.
174. Levin, E.R., *Principles of X-ray spectroscopy*. Scanning Electron Microscopy, 1986. **1986**(1): p. 7.
175. Girão, A.V., *SEM/EDS and optical microscopy analysis of microplastics*, in *Handbook of Microplastics in the Environment*. 2022, Springer. p. 57-78.
176. Gharbi, O., *In-situ investigation of elemental corrosion reactions during the surface treatment of Al-Cu and Al-Cu-Li alloys*. 2016, Paris 6.
177. Netzsch. <https://analyzing-testing.netzsch.com/en/products/thermal-diffusivity-and-conductivity>.

178. Gawryla, M.D., et al., *Clay aerogel/cellulose whisker nanocomposites: a nanoscale wattle and daub*. Journal of Materials Chemistry, 2009. **19**(15): p. 2118-2124.
179. Gupta, P., et al., *Low density and high strength nanofibrillated cellulose aerogel for thermal insulation application*. Materials & Design, 2018. **158**: p. 224-236.
180. Koumoto, K., et al., *High - resolution electron microscopy observations of stacking faults in β - SiC*. Journal of the American Ceramic Society, 1989. **72**(10): p. 1985-1987.
181. Ghosh, B., et al., *Highly ordered $BN \perp -BN \perp$ stacking structure for improved thermally conductive polymer composites*. Advanced Electronic Materials, 2020. **6**(11): p. 2000627.
182. Mao, F., et al., *Microstructure evolutions of SiC whiskers at high temperature and its effects on silicon carbide ceramics*. Ceramics International, 2023.
183. Bansal, A., et al., *Quantitative equivalence between polymer nanocomposites and thin polymer films*. Nature materials, 2005. **4**(9): p. 693-698.
184. Xiao, C., et al., *Enhanced thermal conductivity of silicon carbide nanowires (SiCw)/epoxy resin composite with segregated structure*. Composites Part A: Applied Science and Manufacturing, 2019. **116**: p. 98-105.
185. Ash, B.J., R.W. Siegel, and L.S. Schadler, *Glass - transition temperature behavior of alumina/PMMA nanocomposites*. Journal of Polymer Science Part B: Polymer Physics, 2004. **42**(23): p. 4371-4383.
186. Rittigstein, P., et al., *Model polymer nanocomposites provide an understanding of confinement effects in real nanocomposites*. Nature materials, 2007. **6**(4): p. 278-282.
187. Hinojosa, M., et al., *Study of the thermomechanical performance of FR-4 laminates during the reflow process*. Journal of Materials Engineering and Performance, 2019. **28**: p. 6761-6770.
188. Kalantarian, A., et al. *Evaluation of high thermal conductivity dielectric on the temperature of PCB components*. in *2017 16th IEEE Intersociety Conference on Thermal and Thermomechanical Phenomena in Electronic Systems (ITherm)*. 2017. IEEE.
189. Kim, K., et al., *Magnetic filler alignment of paramagnetic Fe_3O_4 coated SiC/epoxy composite for thermal conductivity improvement*. Ceramics International, 2015. **41**(9): p. 12280-12287.
190. Kim, K., H. Ju, and J. Kim, *Vertical particle alignment of boron nitride and silicon carbide binary filler system for thermal conductivity enhancement*. Composites Science and Technology, 2016. **123**: p. 99-105.
191. Huang, X., et al., *Polyhedral oligosilsesquioxane - modified boron nitride nanotube based epoxy nanocomposites: an ideal dielectric material with high thermal conductivity*. Advanced Functional Materials, 2013. **23**(14): p. 1824-1831.

192. Hsueh, C.-H. and P.F. Becher, *Thermal Expansion Coefficients of Unidirectional Fiber-Reinforced Ceramics*. Journal of the American Ceramic Society, 1988. **71**(10): p. C438-C441.
193. Mohammad, et al., *Effects of nano-sized ceramic particles on the coefficients of thermal expansion of short SiC fiber-aluminum hybrid composites - ScienceDirect*. Journal of alloys and compounds, 2019. **803**(C): p. 554-564.
194. Liu, X., et al., *Tensile properties and damage evolution in a 3D C/SiC composite at cryogenic temperatures*. Materials Science and Engineering: A, 2011. **528**(25-26): p. 7524-7528.
195. Safi, M., M.K. Hassanzadeh-Aghdam, and M.J. Mahmoodi, *Effects of nano-sized ceramic particles on the coefficients of thermal expansion of short SiC fiber-aluminum hybrid composites*. Journal of Alloys and Compounds, 2019. **803**: p. 554-564.
196. Chan, K.C. and J. Liang, *Thermal expansion and deformation behaviour of aluminium-matrix composites in laser forming*. Composites science and technology, 2001. **61**(9): p. 1265-1270.
197. Schapery, R.A., *Thermal expansion coefficients of composite materials based on energy principles*. Journal of Composite materials, 1968. **2**(3): p. 380-404.
198. Goyal, R., et al., *Thermal expansion behaviour of high performance PEEK matrix composites*. Journal of Physics D: Applied Physics, 2008. **41**(8): p. 085403.
199. Chichane, A., R. Boujmal, and A. El Barkany, *A comparative study of analytical and numerical models of mechanical properties of composites and hybrid composites reinforced with natural reinforcements*. Polymers and Polymer Composites, 2023. **31**: p. 09673911231172491.
200. Jeong, J.-H., et al., *Age and moisture effects on thermal expansion of concrete pavement slabs*. Journal of Materials in Civil Engineering, 2012. **24**(1): p. 8-15.
201. Zhang, C., S. Shen, and X. Jia, *Modification of the Hirsch dynamic modulus prediction model for asphalt mixtures*. Journal of Materials in Civil Engineering, 2017. **29**(12): p. 04017241.
202. Landel, R.F. and L.E. Nielsen, *Mechanical properties of polymers and composites*. 1993: CRC press.
203. Hassanzadeh-Aghdam, M., R. Ansari, and A. Darvizeh, *Micromechanical modeling of thermal expansion coefficients for unidirectional glass fiber-reinforced polyimide composites containing silica nanoparticles*. Composites Part A: Applied Science and Manufacturing, 2017. **96**: p. 110-121.
204. Harris, G., X. *Quantitative measurement of preferred orientation in rolled uranium bars*. The London, Edinburgh, and Dublin Philosophical Magazine and Journal of Science, 1952. **43**(336): p. 113-123.
205. Majumdar, S., D. Kupperman, and J. Sing, *Determinations of Residual Thermal Stresses in a SiC-Al₂O₃ Composite Using Neutron Diffraction*. Journal of the American Ceramic Society, 1988.

206. Zhou, W. and D. Yu, *Fabrication, thermal, and dielectric properties of self-passivated Al/epoxy nanocomposites*. Journal of Materials Science, 2013. **48**: p. 7960-7968.
207. Zhou, W., et al., *Enhanced thermal conductivity and dielectric properties of Al/ β -SiCw/PVDF composites*. Composites Part A: Applied Science and Manufacturing, 2015. **71**: p. 184-191.
208. Zhou, W. and D. Yu, *Fabrication, thermal, and dielectric properties of self-passivated Al/epoxy nanocomposites*. Journal of Materials Science, 2013. **48**(22): p. 7960-7968.
209. Zhou, W. and D. Yu, *Thermal and dielectric properties of the aluminum particle/epoxy resin composites*. Journal of Applied Polymer Science, 2010. **118**(6): p. 3156-3166.
210. Chen, L., et al., *Preparation and characterization of epoxy-based composite with multilayered structure and high thermal conductivity*. Materials Research Express, 2019. **6**(7): p. 075314.
211. Tarhini, A. and A. Tehrani-Bagha, *Graphene-based polymer composite films with enhanced mechanical properties and ultra-high in-plane thermal conductivity*. Composites Science and Technology, 2019. **184**: p. 107797.
212. A, X.H., et al., *High- k polymer nanocomposites with 1D filler for dielectric and energy storage applications*. Progress in Materials Science, 2019. **100**: p. 187-225.
213. Tang, H., Z. Zhou, and H.A. Sodano, *Relationship between BaTiO₃ Nanowire Aspect Ratio and the Dielectric Permittivity of Nanocomposites*. Acs Applied Materials & Interfaces, 2014. **6**(8): p. 5450.
214. Zhao, L., et al., *Synchronously improved thermal conductivity and dielectric constant for epoxy composites by introducing functionalized silicon carbide nanoparticles and boron nitride microspheres*. Journal of Colloid and Interface Science, 2022. **627**: p. 205-214.
215. Sima, W., et al., *Cactus-like double-oriented magnetic SiC and BN networks leading to simultaneously enhanced dielectric strength and thermal conductivity of epoxy composites*. Ceramics International, 2023. **49**(12): p. 19950-19959.
216. Jang, I., et al., *Enhancement of thermal conductivity of BN/epoxy composite through surface modification with silane coupling agents*. Colloids and Surfaces A: Physicochemical and Engineering Aspects, 2017. **518**: p. 64-72.
217. Teng, C., et al., *Flexible, thermally conductive layered composite films from massively exfoliated boron nitride nanosheets*. Composites Part A: Applied Science and Manufacturing, 2019. **124**: p. 105498.
218. Liu, Z., J. Li, and X. Liu, *Novel functionalized BN nanosheets/epoxy composites with advanced thermal conductivity and mechanical properties*. ACS Applied Materials & Interfaces, 2020. **12**(5): p. 6503-6515.
219. Polanský, R., P. Prosr, and M. Čermák, *Determination of the thermal endurance of PCB FR4 epoxy laminates via thermal analyses*. Polymer degradation and stability, 2014. **105**: p. 107-115.

220. Avenas, Y., et al. *Metal-Air-FR4 Electrical Field Management with Embedded Electrical Field Plates for PCB Embedded Power Electronics*. in *CIPS 2024; 13th International Conference on Integrated Power Electronics Systems*. 2024. VDE.
221. Wang, Z., et al., *Effect of high aspect ratio filler on dielectric properties of polymer composites: a study on barium titanate fibers and graphene platelets*. *IEEE Transactions on Dielectrics and Electrical Insulation*, 2012. **19**(3): p. 960-967.
222. Jiang, Y., et al., *Enhanced thermal conductivity and ideal dielectric properties of epoxy composites containing polymer modified hexagonal boron nitride*. *Composites Part A: Applied Science and Manufacturing*, 2018. **107**: p. 657-664.
223. GOgraphene, *Graphene Oxide Analysis*. 2024.
224. Kumar, M., A. Kumar, and A. Abhyankar, *Influence of texture coefficient on surface morphology and sensing properties of W-doped nanocrystalline tin oxide thin films*. *ACS applied materials & interfaces*, 2015. **7**(6): p. 3571-3580.
225. Farivar, F., et al., *Unlocking thermogravimetric analysis (TGA) in the fight against "Fake graphene" materials*. *Carbon*, 2021. **179**: p. 505-513.
226. Wen, Y., et al., *Advances on Thermally Conductive Epoxy - Based Composites as Electronic Packaging Underfill Materials—A Review*. *Advanced Materials*, 2022. **34**(52): p. 2201023.
227. Lei, Y., et al., *The Rheological and Structural Properties of Aqueous Graphene Oxide Dispersions: Concentration and pH Dependence*. *Langmuir*, 2024.
228. Liu, Y., et al., *Enhancing Thermal Conductivity in Polymer Composites through Molding-Assisted Orientation of Boron Nitride*. *Polymers*, 2024. **16**(8): p. 1169.
229. Zhu, H., et al., *Highly thermally conductive papers with percolative layered boron nitride nanosheets*. *ACS nano*, 2014. **8**(4): p. 3606-3613.
230. Zhi, C., et al., *Large-scale fabrication of boron nitride nanosheets and their utilization in polymeric composites with improved thermal and mechanical properties*. *Advanced materials*, 2009. **21**(28): p. 2889-2893.
231. Gao, G., et al., *Artificially stacked atomic layers: toward new van der Waals solids*. *Nano letters*, 2012. **12**(7): p. 3518-3525.
232. Vinod, S., et al., *Low-density three-dimensional foam using self-reinforced hybrid two-dimensional atomic layers*. *Nature communications*, 2014. **5**(1): p. 4541.
233. Zhang, Z., et al., *Hexagonal boron nitride: a promising substrate for graphene with high heat dissipation*. *Nanotechnology*, 2017. **28**(22): p. 225704.
234. Warzoha, R.J. and A.S. Fleischer, *Heat flow at nanoparticle interfaces*. *Nano Energy*, 2014. **6**: p. 137-158.

235. Michel, K. and B. Verberck, *Theoretical phonon dispersions in monolayers and multilayers of hexagonal boron - nitride*. *physica status solidi (b)*, 2009. **246**(11 - 12): p. 2802-2805.
236. Song, N.-J., et al., *Thermally reduced graphene oxide films as flexible lateral heat spreaders*. *Journal of Materials Chemistry A*, 2014. **2**(39): p. 16563-16568.
237. Xu, Y., Z. Li, and W. Duan, *Thermal and thermoelectric properties of graphene*. *Small*, 2014. **10**(11): p. 2182-2199.
238. Yao, Y., et al., *Significant enhancement of thermal conductivity in bioinspired freestanding boron nitride papers filled with graphene oxide*. *Chemistry of Materials*, 2016. **28**(4): p. 1049-1057.
239. Li, Q., et al., *Solution-processed ferroelectric terpolymer nanocomposites with high breakdown strength and energy density utilizing boron nitride nanosheets*. *Energy & Environmental Science*, 2015. **8**(3): p. 922-931.
240. Xu, S., et al., *Influence of magnetic alignment and layered structure of BN&Fe/EP on thermal conducting performance*. *Journal of Materials Chemistry C*, 2016. **4**(4): p. 872-878.
241. Chen, J., et al., *Vertically aligned and interconnected boron nitride nanosheets for advanced flexible nanocomposite thermal interface materials*. *ACS applied materials & interfaces*, 2017. **9**(36): p. 30909-30917.